Image-Based Dosimetry in Targeted Radionuclide Therapy with Terbium-161:
From Technical Foundations to Clinical Application

© Frida Westerbergh 2025

frida.westerbergh@gu.se
Department of Medical Radiation Sciences, Institute of Clinical Sciences, Sahlgrenska Academy,
University of Gothenburg, Gothenburg, 2025

ISBN 978-91-8115-248-7 (PRINT) | ISBN 978-91-8115-249-4 (PDF)

Image-Based Dosimetry in Targeted Radionuclide Therapy with Terbium-161

From Technical Foundations to Clinical Application

Frida Westerbergh

Department of Medical Radiation Sciences
Institute of Clinical Sciences
Sahlgrenska Academy, University of Gothenburg

UNIVERSITY OF GOTHENBURG
Gothenburg 2025

Cover illustration: *One size fits some* by Frida Westerbergh

© Frida Westerbergh 2025
frida.westerbergh@gu.se

ISBN 978-91-8115-248-7 (PRINT)
ISBN 978-91-8115-249-4 (PDF)

Printed in Borås, Sweden 2025
Printed by Stema Specialtryck AB

"Mät aldrig bergets höjd förrän du nått toppen.
Då ska du se hur lågt det var."

– Dag Hammarskjöld

PREFACE

This thesis focuses on image-based quantification in radionuclide therapy and is primarily intended for readers with a background in medical physics. That said, I've aimed to keep the content accessible to those outside the discipline.

To support readability, a glossary is included with key terms related to radiation physics and nuclear medicine. Some are explained in detail in the main text; others appear only in the glossary to avoid repetition. Feel free to consult the glossary as needed. Generative AI (ChatGPT) was used during the writing process to assist with proofreading. All content has been carefully reviewed and edited to ensure accuracy. Unless otherwise stated, all illustrations are my own work.

Writing this thesis has been both a challenging and rewarding journey, and I'm deeply grateful for the people I've met and the places it has taken me. I hope reading it proves to be as enjoyable as writing it has been for me—or at the very least, a little less stressful. ☺

Kind regards,

Frida Westerbergh
19th of April 2025

Image-Based Dosimetry in Targeted Radionuclide Therapy with Terbium-161

From Technical Foundations to Clinical Application

Frida Westerbergh

Department of Medical Radiation Sciences, Institute of Clinical Sciences
Sahlgrenska Academy, University of Gothenburg
Gothenburg, Sweden

ABSTRACT

This work explores SPECT/CT-based quantification of the novel therapeutic radionuclide terbium-161 (^{161}Tb). The interest in ^{161}Tb stems from its substantial emission of low-energy conversion and Auger electrons, hypothesized to enhance the treatment of microscopic cancer disease.

In **Paper I**, technical aspects of ^{161}Tb imaging were investigated through phantom studies, demonstrating the feasibility of accurate quantification. A medium-energy collimator combined with a 75 keV ± 10% energy window was found preferable, which was attributed to reduced degradation from dead time, septal penetration, and scatter.

These effects were further examined in **Paper II** through characterization of a clinical SPECT/CT system, confirming that ^{161}Tb imaging is particularly susceptible to dead-time effects, owing to the emission of high-intensity X-rays and penetration from high-energy, low-yield γ-photons. These limitations were mitigated by employing a medium-energy collimator, rather than a low-energy one.

In **Papers III and IV**, quantitative ^{161}Tb SPECT/CT imaging was applied in two first-in-human clinical studies, evaluating novel ^{161}Tb-labeled radioligands for neuroendocrine and prostate cancer, respectively. In both studies, initial dosimetry results indicated favorable therapeutic indices compared to clinically available ^{177}Lu-labeled alternatives.

Together, these studies underscore both the limitations and potential of ^{161}Tb SPECT/CT imaging, contributing to the groundwork for its future clinical implementation.

Keywords: Dosimetry, SPECT, Terbium-161
ISBN 978-91-8115-248-7 (PRINT)
ISBN 978-91-8115-249-4 (PDF)

SUMMARY IN SWEDISH

Användandet av radioaktiva, tumörsökande läkemedel (s.k. radionuklidterapi) har visat sig vara en effektiv behandlingsstrategi vid spridd cancersjukdom. Behandlingen är emellertid palliativ, vilket innebär att bot sällan uppnås. En möjlig orsak till detta är att de radionuklider som används idag inte är optimala vad gäller strålningens egenskaper, en annan att bristen på individanpassning ofta leder till att patienter underbehandlas.

Beträffande individualisering har radionuklidterapi en unik fördel gentemot andra behandlingsformer – strålningen som avges gör läkemedlet spårbart. Med en så kallad SPECT-kamera kan 3D-bilder av radioaktivitetens fördelning i patienten genereras, vilket möjliggör beräkningar av stråldos till både tumörer och riskorgan. Bildtagning utgör således ett viktigt optimeringsverktyg; det kan användas för att utvärdera behandlingens effektivitet, förutspå negativa biverkningar och jämföra olika läkemedel med varandra.

I denna avhandling undersöks terbium-161 (^{161}Tb), en ny radionuklid som i tidiga studier har visat sig lovande för behandling av neuroendokrin tumörsjukdom och metastaserad prostatacancer. Dock saknas riktlinjer för hur bildtagningsprotokoll bör utformas för att säkerställa god noggrannhet i dosberäkningar – en lucka denna avhandling avser fylla.

Avhandlingen består av fyra delarbeten. De två första arbetena fokuserar på tekniska aspekter av bildtagnings- och bildbearbetningsprocessen. Här genomförs omfattande fantomförsök där olika kärl (ofta med människolik geometri) fylls med ^{161}Tb och avbildas. Genom dessa experiment utvärderas möjligheterna till noggrann dosberäkning, och olika parametrars inverkan på bildkvalitén kartläggs.

De två sista arbetena utgör fallbeskrivningar från två pågående kliniska studier vid universitetssjukhuset i Basel, Schweiz. I dessa testas två olika ^{161}Tb-läkemedel, avsedda för behandling av just neuroendokrina tumörer respektive prostatacancer, för första gången på människa. Bildbaserade dosberäkningar genomförs för att undersöka läkemedlens effektivitet. I båda fallstudierna observerades högre tumördos jämfört med befintliga läkemedel, utan ökad negativ påverkan på friska organ.

Sammantaget belyser denna avhandling utmaningarna såväl som möjligheterna med bildbaserad ^{161}Tb-dosimetri, och bidrar på så vis till utvecklingen av radionuklidterapi som individualiserad behandlingsform vid metastaserad cancer.

LIST OF PAPERS

This thesis is based on the following studies, referred to in the text by their Roman numerals.

I. Westerbergh F, van der Meulen NP, Müller C, Grings A, Ritt P, Bernhardt P. Quantitative Terbium-161 SPECT/CT Imaging: Demonstrating the Feasibility of Image-Based Dosimetry and Highlighting Pitfalls. *Submitted to EJNMMI Research, Nov 22, 2024.*

II. Westerbergh F, McDougall L, Ritt P, Fricke JG, van der Meulen NP, Müller C, Schibli R, Wild D, Bernhardt P. Bridging Physics and Practice: Evaluating Sensitivity, Septal Penetration, and Detector Dead Time in Terbium-161 Gamma-Camera Imaging. *Submitted to EJNMMI Physics, Apr 29, 2025.*

III. Fricke J, Westerbergh F, McDougall L, et al. First-in-human administration of terbium-161-labelled somatostatin receptor subtype 2 antagonist ([^{161}Tb]Tb-DOTA-LM3) in a patient with a metastatic neuroendocrine tumour of the ileum. *Eur J Nucl Med Mol Imaging*. 2024;51(8):2517-2519. doi:10.1007/s00259-024-06641-w

IV. Chirindel A, Nicolas GP, Westerbergh F, et al. First-in-human administration of [^{161}Tb]Tb-SibuDAB and comparative dosimetry with standard [^{177}Lu]Lu-PSMA-I&T as part of the PROGNOSTICS phase Ia study. *Eur J Nucl Med Mol Imaging*. Published online December 5, 2024. doi:10.1007/s00259-024-07009-w

**Note: An extension of Paper III was awarded the 2024 European Association of Nuclear Medicine Marie Curie Award.*

RELATED PUBLICATIONS

Original Research

Hjellström M, Westerbergh F, Forssell-Aronsson E, Isaksson M. Usefulness and limitations of various detector systems for estimation of ^{131}I thyroid activity following an RN event. *J Radiol Prot*. 2024;44(4):10.1088/1361-6498/ad7ec5. Published 2024 Oct 10. doi:10.1088/1361-6498/ad7ec5.

Conference Contributions (Available Online)

Westerbergh F, Rydén T, Khan J, van Essen M, Svensson J, Grudzinski J, Bernhardt P. Patient-specific kidney recovery coefficients may increase dosimetric accuracy of ^{177}Lu-radiopharmaceutical treatments. *Annual Meeting of the Society of Nuclear Medicine & Molecular Imaging (SNMMI'22)*; 2022 Jun 11–14; Vancouver, BC, Canada. J Nucl Med. 2022 Aug;63(Suppl 2):3286.

Westerbergh F, Rydén T, van Essen M, van der Meulen NP, Müller C, Bernhardt P. Exploring the quantitative impact of non-uniformities in SPECT imaging with ^{161}Tb. *Annual Congress of the European Association of Nuclear Medicine (EANM'22)*; 2022 Oct 15–19; Barcelona, Spain. Eur J Nucl Med Mol Imaging. 2022;49(Suppl 1):1–751. OP-826. doi:10.1007/s00259-022-05924-4.

Westerbergh F, Rydén T, van Essen M, Kindblom J, Bernhardt P. Deep learning denoising of ^{177}Lu-PSMA triple-bed SPECT using clinical ^{68}Ga PET/CT images as digital phantoms. *Annual Meeting of the Society of Nuclear Medicine & Molecular Imaging (SNMMI'23)*; 2023 Jun 24–27; Chicago, IL, USA. J Nucl Med. 2023 Jun;64(Suppl 1):P909.

Westerbergh F, van der Meulen NP, Müller C, Grings A, Ritt P, Bernhardt P. Demonstrating the quantitative potential of terbium-161 SPECT/CT imaging: an anthropomorphic phantom study. *Annual Congress of the European Association of Nuclear Medicine (EANM'23)*; 2023 Sep 9–13; Vienna, Austria. Eur J Nucl Med Mol Imaging. 2023;50(Suppl 1):1–898. OP-080. doi:10.1007/s00259-023-06333-x.

Smits K, Rydén T, Westerbergh F, Hemmingsson J, Svensson J, Hallqvist A, Grudzinski J, Bernhardt P. Evaluation of how the number of delineated vertebrae in SPECT influences the accuracy of bone marrow dosimetry. *Annual Meeting of the Society of Nuclear Medicine & Molecular Imaging (SNMMI'23)*; 2023 Jun 24–27; Chicago, IL, USA. *J Nucl Med.* 2023 Jun;64(Suppl 1):P1117.

Smits K, Westerbergh F, Hemmingsson J, Svensson J, Rydén T, Bernhardt P. AI-generated synthetic intermediate projections could enable SPECT-based bone marrow dosimetry with reduced acquisition time. *Annual Congress of the European Association of Nuclear Medicine (EANM'23)*; 2023 Sep 9–13; Vienna, Austria. *Eur J Nucl Med Mol Imaging.* 2023;50(Suppl 1):1–898. OP-836. doi:10.1007/s00259-023-06333-x.

Fricke J, Westerbergh F, McDougall L, Favaretto C, Christ E, Nicolas G, et al. Therapy with the somatostatin receptor antagonist DOTA-LM3 labeled with terbium-161: interim results of the Phase 0 study in patients with gastroenteropancreatic neuroendocrine tumors. *Annual Congress of the European Association of Nuclear Medicine (EANM'24)*; 2024 Oct 19–23; Hamburg, Germany. *Eur J Nucl Med Mol Imaging.* 2024;51(Suppl 1):1–1026. OP-252. doi:10.1007/s00259-024-06838-z.

Chirindel A, Westerbergh F, Schmid D, Ahmadsei N, McDougall L, Baumann A, et al. Targeted radionuclide therapy in metastatic prostate cancer using a new PSMA ligand radiolabeled with terbium-161 ([^{161}Tb]Tb-SibuDAB) - dose identification/escalation Phase Ia/b study. *Annual Congress of the European Association of Nuclear Medicine (EANM'24)*; 2024 Oct 19–23; Hamburg, Germany. *Eur J Nucl Med Mol Imaging.* 2024;51(Suppl 1):1–1026. OP-687. doi:10.1007/s00259-024-06838-z.

Westerbergh F, van der Meulen NP, Müller C, Grings A, Ritt P, Bernhardt P. SPECT/CT calibration and quantification with ^{161}Tb for kidney dosimetry. *Annual Congress of the European Association of Nuclear Medicine (EANM'24)*; 2024 Oct 19–23; Hamburg, Germany. *Eur J Nucl Med Mol Imaging.* 2024;51(Suppl 1):1–1026. OP-687. doi:10.1007/s00259-024-06838-z.

Other Conference Contributions

Westerbergh F, Rydén T, Khan J, van Essen M, Svensson J, Grudzinski J, Bernhardt P. Personalized Monte Carlo-generated kidney recovery coefficients in ^{177}Lu-SPECT imaging: A novel method for increased dosimetric accuracy. *Swedish Radiation Research Association for Young Scientists (SWERAYS) Workshop*; 2022 Aug 23–25; Stockholm, Sweden.

Hjellström M, Westerbergh F, Forssell-Aronsson E, Isaksson M. Usefulness and limitations of various detector systems for estimation of I-131 activity in humans after an RN event. *European Radiation Protection Week (ERPW)*; 2023 Oct 9–13; Dublin, Ireland.

Westerbergh F, van der Meulen NP, Müller C, Grings A, Ritt P, Bernhardt P. Terbium-161 SPECT imaging: Assessing quantifiability for a novel theragnostic nuclide. *EFOMP Symposium on Molecular Radiotherapy Dosimetry: The Future of Theragnostics*; 2023 Nov 9–11; Athens, Greece.

Smits K, Westerbergh F, Svensson J, van Essen M, Rydén T, Bernhardt P. Reducing the influence of noise in bone marrow activity concentration estimates by using AI-generated projections in the SPECT reconstruction. *EFOMP Symposium on Molecular Radiotherapy Dosimetry: The Future of Theragnostics*; 2023 Nov 9–11; Athens, Greece.

Westerbergh F, van der Meulen NP, Müller C, Grings A, Ritt P, Bernhardt P. SPECT/CT imaging with terbium-161: Challenges and possibilities. *Swedish Cancer Society Autumn Meeting*; 2023 Nov 29–Dec 1; Linköping, Sweden.

Fricke J, Westerbergh F, McDougall L, Favaretto C, Christ E, Nicolas GP, et al. The somatostatin receptor subtype 2 antagonist DOTA-LM3 labelled with beta$^-$- and Auger-electron emitter terbium-161: Interim results of the Phase 0 "Beta plus" Study in patients with neuroendocrine tumors. *Swiss Congress of Radiology 2024 (SCR'24)*; 2024 Jun 20–22; Geneva, Switzerland.

Fricke J, Westerbergh F, McDougall L, Christ E, Nicolas GP, Schmid DE, et al. Targeted beta- plus Auger and conversion electron therapy with terbium-161 labelled somatostatin receptor antagonist DOTA-LM3 – BETA plus phase 0 study. *22nd Annual European Neuroendocrine Tumor Society (ENETS) Conference*; 2025 Mar 5–7; Krakow, Poland.

Westerbergh F, McDougall L, Fricke J, Chirindel A, Nicolas GP, van der Meulen NP, et al. Post-therapeutic terbium-161 SPECT/CT imaging: Our journey to quantification. *Optimisation in X-ray and Molecular Imaging (OXMI'25)*; 2025 Apr 28–30; Gothenburg, Sweden.

Projects Supervised

Engström A, Westerbergh F, Rydén T, Bernhardt P. Evaluation of challenges in SPECT-based dosimetry in the treatment of metastatic prostate cancer with ^{177}Lu-PSMA-617 [Master's thesis]. Gothenburg: Sahlgrenska Academy at Gothenburg University; 2024. Available at: https://hdl.handle.net/2077/83503.

Andelin A, Westerbergh F, Rydén T, Bernhardt P. Developing an energy resolution model for Monte Carlo-based SPECT simulation and reconstruction using a GE Discovery NM/CT 670 Pro system [Master's thesis]. Gothenburg: Sahlgrenska Academy at Gothenburg University; 2024. Available at: https://hdl.handle.net/2077/83506.

CONTENTS

Glossary xix
1 Introduction 1
1.1 Overarching Aim 2
2 Background 3
2.1 The History of Radionuclide Therapy 3
2.2 Terbium – A Theragnostic Game Changer? 6
2.2.1 Terbium-161's Path to the Clinic 7
2.2.2 Production 9
2.2.3 Decay Properties 10
2.3 The Gamma Camera 13
2.3.1 Principal Components 13
2.3.2 Collimation 15
2.3.3 Sensitivity 16
2.3.4 Resolution 17
2.3.5 Septal Penetration and Scatter 18
2.3.6 Dead Time 20
2.3.7 Uniformity 22
2.4 Single Photon Emission Computed Tomography 24
2.4.1 Acquisition Protocols 24
2.4.2 Iterative Reconstruction 25
2.4.3 Methods of Compensation 27
2.5 Monte Carlo Simulation 30
2.5.1 Basic Principles for γ-Camera Simulation 30
2.6 Dosimetry in Radionuclide Therapy 33
2.6.1 General Workflow and Calibration 34
2.6.2 The MIRD Formalism 35
2.6.3 Time-Activity Curve Fitting 36
2.7 Radioligand Optimization Strategies 39

2.7.1 Somatostatin Antagonists for Therapy of NETs 39
2.7.2 Albumin-Binding Ligands for Therapy of mCRPC 40
3 Specific Aims 43
4 Patients and Methods 45
4.1 Image Acquisition Protocols 45
4.1.1 Sahlgrenska University Hospital 45
4.1.2 Basel University Hospital 46
4.2 Clinical Study Protocols 47
4.2.1 BETA PLUS for NETs 47
4.2.2 PROGNOSTICS for mCRPC 48
4.3 Activity Measurements 49
4.4 Phantom Measurements 49
4.4.1 Uniformity 49
4.4.2 Calibration Factors 50
4.4.3 Recovery 50
4.4.4 Anthropomorphic Evaluations 51
4.4.5 Sensitivity, Penetration, and Dead Time 52
4.5 SPECT Reconstructions 53
4.5.1 Conventional OSEM Reconstruction 53
4.5.2 MC-Based OSEM Reconstruction 53
4.6 Clinical Dosimetry 54
4.6.1 Segmentation and Activity Quantification 54
4.6.2 TAC Fitting and Absorbed Dose Calculations 55
5 Results 57
5.1 Technical Foundations (Paper I & II) 57
5.2 Clinical Application (Paper III & IV) 62
6 Discussion 67
7 Future Perspectives 71
Summarizing Thoughts 73
References 76
Acknowledgements 91

ABBREVIATIONS

2D	Two-Dimensional
3D	Three-Dimensional
AI	Artificial Intelligence
ARF	Angular Response Function
CDR	Collimator Detector Response
CF	Calibration Factor
CT	Computed Tomography
CUDA	Compute Unified Device Architecture
CZT	Cadmium Zinc Telluride
DEW	Dual Energy Window
DOTA	Dodecane Tetraacetic Acid
DTPA	Diethylenetriaminepentaacetic Acid
EC	Electron Conversion
ELEGP	Extended Low Energy General Purpose
EM	Emission Window
FOV	Field of View
GE	General Electric
GPU	Graphics Processing Unit
HPGe	High-Purity Germanium
HU	Hounsfield Unit
I&T	Imaging and Therapy
IC	Internal Conversion
ICRP	International Commission on Radiological Protection
IQR	Interquartile Range
LEHR	Low Energy High Resolution
MC	Monte Carlo
mCRPC	Metastatic Castration-Resistant Prostate Cancer
MEGP	Medium Energy General Purpose
MELP	Medium Energy Low Penetration
MIRD	Medical Internal Radiation Dose

MLEM	Maximum Likelihood Expectation Maximization
MRI	Magnetic Resonance Imaging
NaI(Tl)	Thallium Doped Sodium Iodide
NEMA	National Electrical Manufacturers Association
NETs	Neuroendocrine Tumors
OSEM	Ordered Subsets Expectation Maximization
PET	Positron Emission Computed Tomography
PHA	Pulse Height Analyzer
PMT	Photomultiplier Tube
PRRT	Peptide Receptor Radionuclide Therapy
PSF	Point Spread Function
PSI	Paul Scherrer Institute
PSMA	Prostate-Specific Membrane Antigen
PVE	Partial Volume Effect
RC	Recovery Coefficient
RQE	Relative Quantification Error
RR	Resolution Recovery
SARec	Sahlgrenska Academy Reconstruction Code
SBR	Sphere-to-Background Ratio
SC	Scattering Window
SPECT	Single-Photon Emission Computed Tomography
sphCF	Sphere-Based Calibration Factor
SSTR	Somatostatin Receptor
TAC	Time-Activity Curve
TATE	Tyr3-Octreotate
TEW	Triple Energy Window
TIA	Time-Integrated Activity
TOC	Tyr3-Octreotide
uniCF	Uniform Calibration Factor
VOI	Volume-of-Interest

GLOSSARY

Absorbed dose: A dosimetric quantity used to estimate the biological effects of ionizing radiation, defined as the energy deposited per unit mass.

Alpha (α) decay: Decay in which an α-particle (i.e., a helium nucleus) is ejected from a heavy, unstable nucleus.

Attenuation: The elimination of photons travelling through a medium (through absorption or scattering), causing a reduction in beam intensity.

Auger electron: An orbital electron emitted from an atom after gaining energy when another electron fills an inner vacancy. Competes with X-ray emission.

Beta minus (β^-) decay: Decay in which a neutron is converted into a proton, causing the emission of a negatively charged β-particle (i.e., electron) and an antineutrino. Most common for neutron-rich nuclei.

Beta plus (β^+) decay: Decay in which a proton is converted into a neutron, causing the emission of a positively charged β-particle (i.e., positron) and a neutrino. Most common for proton-rich nuclei. The process competes with EC. Indirectly results in the emission of annihilation photons.

Compton scattering: A photon interaction in which a photon transfers part of its energy to an orbital electron and is deflected with reduced energy.

Conversion electron: An orbital electron emitted after gaining excess energy from an excited nucleus. Competes with γ emission.

Dosimetry: The calculation and assessment of radiation doses from exposure to ionizing radiation.

Electron capture (EC): Decay in which an atomic electron is absorbed into the nucleus, converting a proton into a neutron, and causing the emission of a neutrino. Most common for proton-rich nuclei. The process sometimes competes with β^+ decay, if the excess energy is high enough.

Gamma photon (γ): A photon emitted when an excited nucleus releases excess energy. Competes with conversion electron emission.

Half-life (T½): The time after which half of the nuclei in a radioactive sample has decayed.

Ionizing radiation: Radiation (e.g., photons or particles) with enough energy to remove an electron from an atom, i.e., cause ionization.

Isotope: An atom with a specific number of neutrons, belonging to a group of atoms that share the same number of protons. Sometimes used interchangeably with "nuclide."

Labeling: The process of chemically attaching a radioactive element to a molecule for diagnostic or therapeutic purposes.

Ligand: A molecule that binds to a specific cellular target. Commonly used as an umbrella term for carrier molecules in radiopharmaceuticals.

Nuclear medicine: A branch of medicine that uses radioactive drugs (i.e., radiopharmaceuticals) to diagnose and/or treat various conditions.

Nuclide: A specific type of atom defined by its number of protons and neutrons. Sometimes used interchangeably with "isotope."

PET imaging: A diagnostic nuclear medicine imaging modality used for β^+-emtting radiopharmaceuticals.

Photoabsorption: A photon interaction in which a photon transfers all its energy to an atom and ceases to exist.

Radioactivity: A property of unstable elements, characterized by the emission of various particles (i.e., radiation), in the atom's effort of reaching a more stable configuration. Measured in decays per unit time (1 Becquerel or Bq = 1 decay per second).

Radiopharmaceutical: A radioactive drug, used for imaging and/or therapy, with specific targeting properties. Usually consists of a radionuclide labeled to a carrier molecule/ligand.

SPECT imaging: A diagnostic nuclear medicine imaging modality used for γ-emitting radiopharmaceuticals

Theragnostics: A fusion of the words *therapy* and *diagnostics*, referring to treatment strategies that combine radionuclide therapy with radionuclide-based imaging—either before, during, or after treatment—using the same pharmaceutical or complementary agents.

X-ray: A photon emitted when an electron transitions between atomic orbitals, often after an inner electron is removed. Competes with Auger electron emission.

Yield: The likelihood of a certain emission following the decay of a given nuclide.

1 INTRODUCTION

Approximately 75,000 people are diagnosed with cancer in Sweden annually, corresponding to a lifetime risk of one in three. While the number of reported cases is on a steady uptick, advances in treatment and early detection have dramatically improved survival rates; in 1970, the 10-year survival was roughly 30%, compared to 72% today (*1*). However, despite this considerable progress, the prognosis for patients with metastatic disease generally remains poor.

Radionuclide therapy is a well-established, yet rapidly emerging, treatment modality that has offered hope for effectively treating metastatic cancer disease. With this approach, radiation can be delivered directly to malignant tissue via radioactive, tumor-targeting drugs—i.e., *radiopharmaceuticals.*

Therapeutic radiopharmaceuticals generally consist of a radioactive nuclide labeled to a carrier molecule (or *ligand*), where the latter dictates where in the body the drug accumulates. In brief, the drug will circulate through the bloodstream and bind to a specific target (e.g., a receptor on the tumor cell surface). Once bound, the radionuclide will disintegrate, releasing particles (e.g., α- or β^--particles) that deposit their energy in close proximity to the decay site, causing cellular damage that yields a therapeutic effect.

For most radionuclides, the emission of particles is accompanied by the emission of photons (i.e., γ- or X-rays). Photons can, unlike α- or β^--particles, travel long distances without being absorbed, allowing them to be detected *outside* the patient's body. Using radiation detectors in the form of nuclear medicine imaging devices (e.g., a SPECT camera) allows us to trace the photons back to the decay site, and create a map of the distribution of the radiopharmaceutical within the patient, as shown in Figure 1.

FIGURE 1. Post-therapeutic SPECT image of a prostate cancer patient with skeletal metastases, acquired 24 hours after administration.

The possibility for post-therapeutic imaging gives radionuclide therapy a unique edge over other systemic cancer treatments; we actually have insight as to where in the body the pharmaceutical resides. This knowledge allows us to quantify the amount of radioactivity present in different tissues, which in turn enables radiation dose calculations for both tumors and healthy organs at risk; a process referred to as *dosimetry*.

Currently, radionuclide therapy is primarily palliative, focusing on disease control and symptom alleviation rather than achieving complete remission. The limited curative success of radionuclide therapy can be attributed to several factors, one being the lack of personalization. SPECT-based dosimetry could help identify patients who might benefit from intensified treatment, without risk for serious adverse effects.

Another potential limitation lies in the properties of the radioligands used. In some cases, the radiation emitted may not be ideal in terms of energy and range, and alternative radionuclides could be more suitable (e.g., depending on tumor size). Additionally, the pharmacological profile of the ligands employed may be suboptimal; we might fail to achieve sufficiently high tumor accumulation, or promote too high accumulation in healthy organs, causing toxicity.

In this thesis, we examine the novel therapeutic radionuclide terbium-161 (^{161}Tb). It shares many similarities with the widely adopted lutetium-177 (^{177}Lu), including comparable β^- decay properties. However, ^{161}Tb also emits a substantial amount of low-energy conversion and Auger electrons, providing an additional short-ranged dose boost. These characteristics are theorized to make ^{161}Tb suitable for treating both larger tumors *and* micrometastases—small, undetectable tumors that can contribute to disease progression and relapse.

Currently, ^{161}Tb-labeled radiopharmaceuticals are rapidly progressing toward clinical implementation, with multiple ongoing first-in-human trials. However, due to the nuclide's novelty, standardized imaging and dosimetry guidelines are lacking.

1.1 OVERARCHING AIM

The overarching aim of this thesis is to support the clinical translation of ^{161}Tb-based radionuclide therapy by advancing image-based activity quantification and dosimetry. Specifically, we investigate technical aspects of imaging and quantification (Papers I and II) and apply this knowledge in two first-in-human trials at the University Hospital of Basel, Switzerland (Papers III and IV). In these trials, we use SPECT/CT-based dosimetry to compare different ^{161}Tb- and ^{177}Lu-labeled ligands in the treatment of neuroendocrine tumors and metastatic prostate cancer.

2 BACKGROUND

This chapter aims to provide scientific context for the research presented in subsequent chapters. It begins with a historical overview of radionuclide therapy and the emergence of ^{161}Tb as a theragnostic nuclide. Key principles of γ-camera imaging and recent developments in quantitative SPECT are then discussed, in relation to Papers I–II. Finally, the chapter outlines the fundamentals of radionuclide dosimetry and highlights recent advances in radioligand development, relevant to the clinical trials described in Papers III–IV.

2.1 THE HISTORY OF RADIONUCLIDE THERAPY

In the early 1900s, biologist and Nobel Prize laureate Paul Ehrlich proposed the concept of the "*magic bullet*" as a metaphor for the perfect pharmaceutical. Ehrlich envisioned a drug that could selectively target and damage pathological tissue, while leaving healthy tissue unharmed (2).

Only a few years prior, in 1896, physicist Henri Becquerel observed the spontaneous emission of some mysterious particles while studying a collection of uranium salts inherited from his father. With that, natural radioactivity was discovered. Drawing on Becquerel's findings, Marie and Pierre Curie identified the radioactive elements radium and polonium, thereby laying the foundation for the scientific understanding of radioactivity. These groundbreaking discoveries earned all three the 1903 Nobel Prize in Physics.

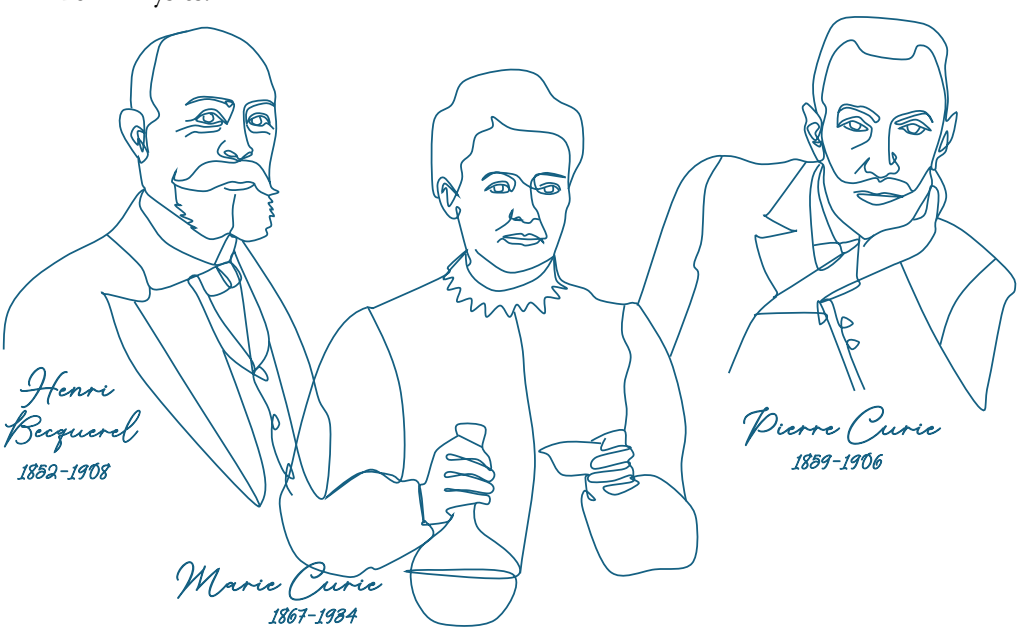

These two fields of research—selective targeting of diseases and radioactivity—would merge sooner than one might have anticipated. In the 1910s, another Nobel Prize laureate, George de Hevesy, made the pivotal discovery that radioactive elements could function as tracers whilst studying metabolic processes in animals and plants. This was an important step toward medical integration; de Hevesy published his findings in 1923 (3) and shortly thereafter, in 1927, Blumgart and Weiss used bismuth-214 to determine the velocity of blood in humans (4). Other diagnostic applications soon followed.

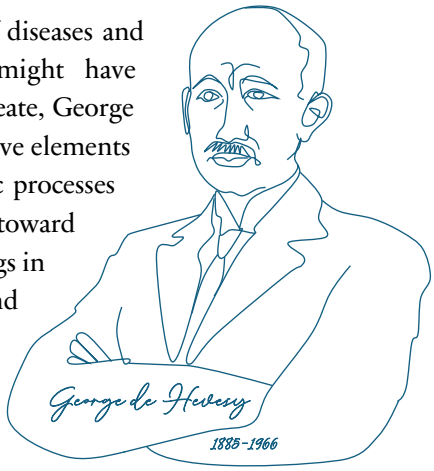

The first therapeutic applications emerged in the 1930s. In 1937, John H. Lawrence initiated the use of phosphorus-32 to treat leukemia, making it the earliest documented radionuclide therapy (5). Around the same time, Saul Hertz's work on iodine metabolism in Grave's disease laid the foundation for the clinical use of iodine-131. By the 1940s to 1950s, iodine-131 was routinely used in the diagnosis and treatment of thyroid cancer and hyperthyroidism (6).

These early forms of radionuclide therapy relied on the natural tendency of certain elements to accumulate in specific tissues, without the need for any complex chemical modification. For example, iodine-131 follows the physiological pathway of stable iodine (which is essential for thyroid hormone synthesis), while phosphorus-32, as a phosphate compound, naturally accumulates in regions of active bone remodeling.

It soon became evident, however, that the potential of radionuclide therapy could be greatly expanded through chemical engineering. By *labeling* bioactive molecules—such as antibodies, peptides, or small molecules—with radioactive elements, one could combine the specific targeting of one compound with the cytotoxic effects of radiation. This marked a major shift; transforming radionuclide therapy from a relatively simple approach based on natural analogs, to a more versatile and sophisticated treatment modality.

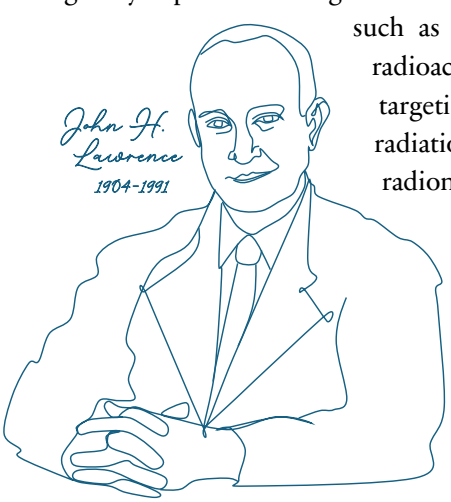

The 1990s marked the birth of peptide receptor radionuclide therapy (PRRT). By this time, it was recognized that neuroendocrine tumors (NETs)—a diverse group of malignancies, that

originate from neuroendocrine cells—commonly express a high level of somatostatin receptors. These receptors had proven to be suitable targets for disease visualization (significant advancements in imaging had already been achieved at this point, with Hal Anger's invention of the γ-camera in the 1950s (7), the development of SPECT by Kuhl and Edwards in the 1960s (8), and the invention of PET in the 1970s (9) being the most notable).

The first successful PRRT of NETs was performed in Rotterdam in 1992, using indium-111-pentetreotide—an agent previously employed for imaging, but using lower activity (*10*). Subsequent research explored alternative ligands and radionuclides with more favorable therapeutic properties, such as yttrium-90 and later lutetium-177. These advancements ultimately led to the first clinical approval of a PRRT agent in 2018: [^{177}Lu]Lu-DOTATATE as Lutathera®, following the pivotal NETTER-1 trial (*11*).

Building on this success, PRRT using lutetium-177 expanded beyond NETs. In 2022, [^{177}Lu]Lu-PSMA-617 (Pluvicto®) was approved for the treatment of metastatic castration-resistant prostate cancer (mCRPC), as a result of the VISION trial (*12*). This ligand targets the prostate-specific membrane antigen (PSMA), which is highly expressed in prostate cancer cells.

Today, nuclear medicine has evolved into a multifaceted field with therapeutic and diagnostic applications across several diagnoses. Roughly 67 radiopharmaceuticals have been approved for clinical use worldwide, including 13 for therapy (*13*). Besides those already mentioned, these include radium-223 and strontium-89 chloride for pain relief in skeletal metastases, yttrium-90-labeled antibodies for non-Hodgkin's lymphoma, and iodine-131-labeled small molecules for childhood neuroblastoma.

Ongoing research continues to expand the catalog of radionuclides and molecular targets, striving to enhance therapeutic efficacy while minimizing toxicity—all with the prospect of bringing Ehrlich's vision of a "*magic bullet*" closer to reality.

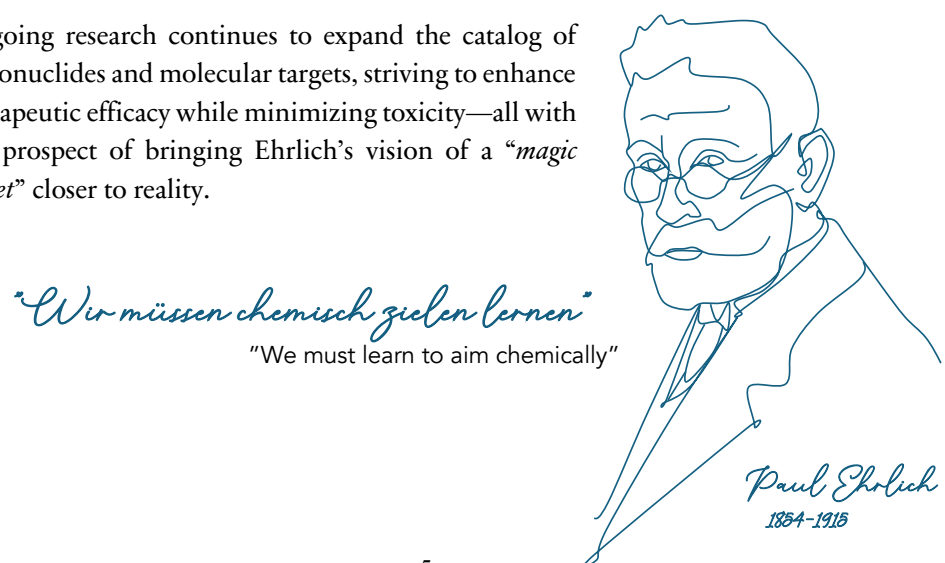

2.2 TERBIUM – A THERAGNOSTIC GAME CHANGER?

While the concept of *theragnostics* (or *theranostics*) is as old as nuclear medicine itself—dating back to the use of radioiodine in the 1930s (*14*)—it has recently become a bit of a buzzword in the field. The term is used somewhat ambiguously, but generally refers to nuclear medicine applications where therapy and diagnostics (primarily using PET or SPECT imaging) are combined as a unified treatment strategy.

The perhaps most direct form of theragnostics is when a single radiopharmaceutical is used, allowing diagnostics in direct conjunction with therapy. The most prominent clinical examples are ^{131}I and ^{177}Lu. Both decay via β^- emission (providing the main therapeutic effect), while simultaneously emitting γ-photons that enable diagnostics in the form of *post-therapeutic** SPECT imaging. In these cases, images are usually acquired at multiple time points after administration and are used to monitor response and estimate absorbed doses.

Theragnostics can also refer to treatment strategies in which pairs or sets of radiopharmaceuticals with similar biokinetic properties (i.e., uptake, redistribution, and excretion) are used. Here, imaging may be performed either before treatment (to diagnose and assess a patient's eligibility for therapy) or after treatment (to evaluate therapeutic outcomes).

A common approach involves labeling the same ligand with different elements. For example, PSMA-617 and DOTATATE are ligands used to target prostate cancer and neuroendocrine tumors, respectively. When labeled with the β^+-emitter ^{68}Ga, they serve as diagnostic PET imaging agents; when labeled with ^{177}Lu, they act as therapeutic agents.

Another appealing theragnostic strategy is to use isotopes of the same element, as they share identical chemical properties. This ensures matched biokinetics and allows for identical labeling procedures. A clinical example is iodine-based theragnostics, where ^{123}I and ^{124}I are used for diagnostic SPECT and PET imaging, respectively, and ^{131}I is used for therapy and post-therapeutic imaging (*14*).

Beyond these clinically established examples, research has focused on identifying new theragnostic nuclides—or sets of nuclides—with optimal imaging and therapeutic properties, which leads us to terbium.

**Peri-therapeutic* *(i.e., during therapy) would be more semantically accurate, as images are acquired while the therapy is technically ongoing. However, post-therapeutic is the more established term, and I have chosen to use it consistently throughout the thesis.*

2.2.1 Terbium-161's Path to the Clinic

Terbium (Tb) is a rare earth metal in the lanthanoid series, first discovered in 1843 in the Ytterby mine, located in the Stockholm archipelago (15). Naturally occurring terbium consists of a single stable isotope, ^{159}Tb. Since its discovery, 37 radioactive terbium isotopes have been synthesized (16), four of which—^{149}Tb, ^{152}Tb, ^{155}Tb, and ^{161}Tb—have been suggested for theragnostic applications (17). Their key decay properties (18) and proposed application are summarized in Table 2.1.

TABLE 2.1. General decay properties (half-life, $T_{½}$, decay mode, daughter nuclide) of the four terbium sisters, retrieved from ICRP 107 (18), along with their proposed medical application (17).

Nuclide	Half-life, $T_{½}$	Decay mode (Probability)	Daughter	Proposed application
^{149}Tb	4.188 hours	EC, β^+ (83.3%) α (16.7%)	^{149}Gd (Active) ^{145}Eu (Active)	Therapeutic (α therapy)
^{152}Tb	17.5 hours	EC, β^+ (100%)	^{152}Gd (Stable)	Diagnostic (PET)
^{155}Tb	5.32 days	EC (100%)	^{155}Gd (Stable)	Diagnostic (SPECT)
^{161}Tb	6.906 days	β^- (100%)	^{161}Dy (Stable)	Theragnostic (e^- therapy and SPECT)

Out of the four, ^{161}Tb stands out due to its favorable decay properties and accessible production, making it the most clinically advanced "*terbium sister*" (19). First synthesized during the Atomic Era (in 1949) (16), ^{161}Tb remained a subject of nuclear research for decades before its potential in medicine was explored. The first medical application came in 1995, when a research group in Rotterdam administered [^{161}Tb]Tb-DTPA-octreotide to rats, demonstrating its potential as a high-affinity radioligand for somatostatin receptors (20).

In the early 2000s, theoretical dosimetry studies laid the foundation for future applications by identifying ^{161}Tb as a promising nuclide for radionuclide therapy (alongside ^{177}Lu). These studies demonstrated favorable tumor-to-normal organ absorbed dose ratios in both murine (21) and human models (21, 22).

Subsequent preclinical research (particularly from the Paul Scherrer Institute, PSI, in Switzerland during the 2010s) further highlighted the therapeutic advantages of ^{161}Tb. When labeled to a folate conjugate, ^{161}Tb produced better therapeutic effects *in vivo* and *in vitro* compared to ^{177}Lu (23), with no additional renal damage (24). By this time, the feasibility of producing ^{161}Tb in the qualities and quantities required for clinical use had also been confirmed (25).

By the start of the 2020s, theoretical studies had further reinforced that ^{161}Tb is particularly effective for treating smaller tumors due to its large emission of low-energy conversion and Auger electrons (26–28). In addition to this, a first protocol for clinical SPECT/CT imaging had been established, revealing good visual image quality in phantoms (29). With these advancements, the first-ever in-human application took place in Bad Berka in 2021, where two patients were successfully treated and imaged using 600 and 1300 MBq of [^{161}Tb]Tb-DOTATOC, respectively (30) (despite no prior preclinical evaluation of the compound).

Since then, it has been shown that replacing ^{177}Lu with ^{161}Tb does not alter the pharmacokinetic profile of somatostatin analogues (31), and preclinical studies have confirmed the superiority of ^{161}Tb over ^{177}Lu for both SSTR (32) and PSMA (33) ligands. Moreover, theoretical models have consistently demonstrated ^{161}Tb's favorable characteristics for treating microscopic disease (34, 35), particularly in prostate cancer (36). It has also been shown that using ^{161}Tb results in a ~40% higher tumor absorbed dose per unit activity compared to ^{177}Lu (37).

Today, multiple facilities around the globe are capable of producing high-quality ^{161}Tb in quantities sufficient for therapy (38–41), and efficient labeling techniques have been established (42). As a result, ^{161}Tb is rapidly advancing into clinical applications (43–49), with ongoing first-in-human trials for both prostate cancer (45–48) and neuroendocrine tumors (49) (see Table 2), showing encouraging initial results (43, 44, 46–49).

TABLE 2.2. An overview of ongoing trials involving ^{161}Tb (as of April 2, 2025, sourced from https://clinicaltrials.gov/).

NCT Number	Study Acronym	Location	Condition	Drug	Duration	Ref.
NCT05521412	VIOLET	Melbourne, Australia	mCRPC	^{161}Tb-PSMA-I&T	Sep-22 – Dec-26	(45)
NCT05359146	BETA PLUS	Basel, Switzerland	NETs	^{161}Tb-DOTA-LM3 ^{177}Lu-DOTATOC	Mar-23 – Dec-25	(49)
NCT06343038	PROGNOSTICS	Basel, Switzerland	mCRPC	^{161}Tb-SibuDAB ^{177}Lu-PSMA-I&T	Feb-24 – Jun-28	(48)
NCT06827080	n/a	Mianyang, China	mCRPC	^{161}Tb-NYMO32	Feb-25 – Dec-26	n/a
NCT04833517	REALITY	Homburg, Germany	mCRPC	Multiple, incl. ^{177}Lu, ^{223}Ra, ^{153}Sm, ^{225}Ac, ^{161}Tb, and ^{90}Y	Jan-16 – Dec-25	(46,47)

2.2.2 Production

As a neutron-rich nuclide, ^{161}Tb can be produced via neutron bombardment in a nuclear reactor. The most efficient production route involves neutron activation of ^{160}Gd to ^{161}Gd, which quickly decays to ^{161}Tb, as follows (25):

$$^{160}\text{Gd}(n,\gamma)^{161}\text{Gd} \rightarrow \beta^{-}\ (T_{½} = 3.7\ \text{min}) \rightarrow {}^{161}\text{Tb}$$

After separation from the target, high-purity ^{161}Tb can be obtained, with a radionuclidic purity exceeding 99.99% (38). As with other lanthanides, ^{160}Gd has a high neutron capture cross-section, allowing the production of high activity levels (22).

To obtain high-purity ^{161}Tb, the ^{160}Gd target must be highly enriched. The most prominent impurity in ^{161}Tb production is ^{160}Tb (19): a long-lived nuclide ($T_{½}$ = 72.3 days, β^{-} decay) that emits a series of high-energy, high-yield γ-rays, e.g., 879 keV (30.1%), 966 keV (25.1%), and 1178 keV (14.9%) (50). Natural gadolinium contains several isotopes, and ^{160}Tb can be co-produced via two main routes: ^{158}Gd(n,γ)^{159}Gd → ^{159}Tb(n,γ)^{160}Tb, and ^{157}Gd(n,γ)^{158}Gd → ^{158}Gd(n,γ)^{159}Gd → ^{159}Tb(n,γ)^{160}Tb (19). Managing ^{160}Tb presents several challenges—e.g., in terms of waste disposal, imaging, and radiation dose to personnel—and its presence should therefore be minimized.

That said, current protocols enable the production of high-quality ^{161}Tb, making it suitable for clinical use. Its chemical similarity to ^{177}Lu also allows for labeling using established techniques (25). In addition, upscaling production is possible either by increasing the neutron flux or by increasing the target mass. Long-term challenges include securing a reliable supply of enriched target material (19).

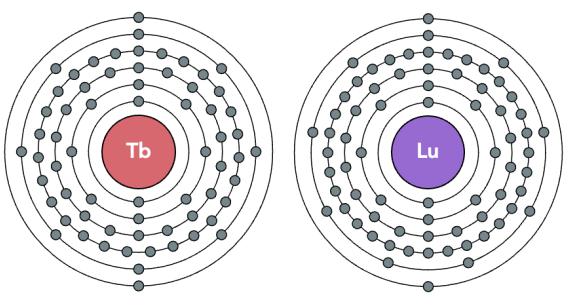

FIGURE 2.1. Electron shell configuration of ^{161}Tb and ^{177}Lu. Both radionuclides are lanthanides and exhibit similar outer electron configurations, resulting in comparable chemical properties, thus enabling similar labeling strategies.

2.2.3 Decay Properties

Like the clinically established ^{177}Lu, ^{161}Tb decays via β^- emission with subsequent γ-photon emissions. Besides this, there are additional similarities between the two radionuclides: both belong to the lanthanoid series (Figure 2.1), have comparable half-lives—$T_{½}$(^{161}Tb) = 6.953 days (51,52)* and $T_{½}$(^{177}Lu) = 6.647 days (53)—and emit β^--particles with similar average energies (154 keV/decay for ^{161}Tb and 133 keV/decay for ^{177}Lu), as summarized in Table 2.3.

TABLE 2.3. Key decay characteristics for ^{161}Tb and ^{177}Lu, respectively, including decay mode, half-life, mean energy emitted per decay (Δ) for β^- particles, conversion and Auger electrons, along with the number of listed emissions, #, in brackets (18).

	^{161}Tb	^{177}Lu
Decay	β^- (100%)	β^- (100%)
Daughter	^{161}Dy (Stable)	^{177}Hf (Stable)
Half-life, $T_{½}$	6.647 days	6.953 days
Energy, Δ_{β^-} [#]	154 keV [9]	133 keV [4]
Energy, $\Delta_{Auger\ e^-}$ [#]	8.94 keV [15]	1.13 keV [15]
Energy, $\Delta_{conv\ e^-}$ [#]	39.3 keV [199]	13.5 keV [36]
Energy, $\Delta_{all\ e^-}$	202 keV	148 keV

However, there are some fundamental differences, as evident in the decay schemes in Figures 2.2 and 2.3 (53, 54). While ^{177}Lu has four possible β^- transitions, ^{161}Tb has nine. This leads to a greater variety of subsequent de-excitations and, consequently, a broader range of γ-emissions for ^{161}Tb. Specifically, ^{161}Tb has 33 possible γ-emissions (25.7–550 keV), whereas ^{177}Lu has six (71.6–321 keV).

Since γ-emission competes with internal conversion (IC)—a process in which the excess nuclear energy is transferred to an orbital electron—^{161}Tb also exhibits a significant emission of conversion electrons. In ICRP 107, 199 such emissions are detailed for ^{161}Tb, compared to 36 for ^{177}Lu, resulting in a markedly higher IC energy release: 39.3 keV/decay versus 13.5 keV/decay, see Table 2.3.

When an electron vacancy is created following IC, it can lead to the emission of Auger electrons. ICRP 107 lists 15 Auger emissions for both ^{161}Tb and ^{177}Lu, with comparable individual energies. However, due to a higher emission probability, the total Auger energy released per decay is substantially greater for ^{161}Tb—8.94 keV/decay, compared to 1.13 keV/decay for ^{177}Lu, see Table 2.3.

**Discrepancies in $T_{½}$(^{161}Tb) may be noted (e.g., in Table 2.1, taken from ICRP 107). $T_{½}$ = 6.953(2) days was reported by Durán et al., based on three independent methods (51). A more recent study reported 6.967(11), days and proposed a weighted average of 6.9582(33) days based on four publications (52). While I acknowledge these (minor) variations, Durán's value is among the most precise and has been used for consistency.*

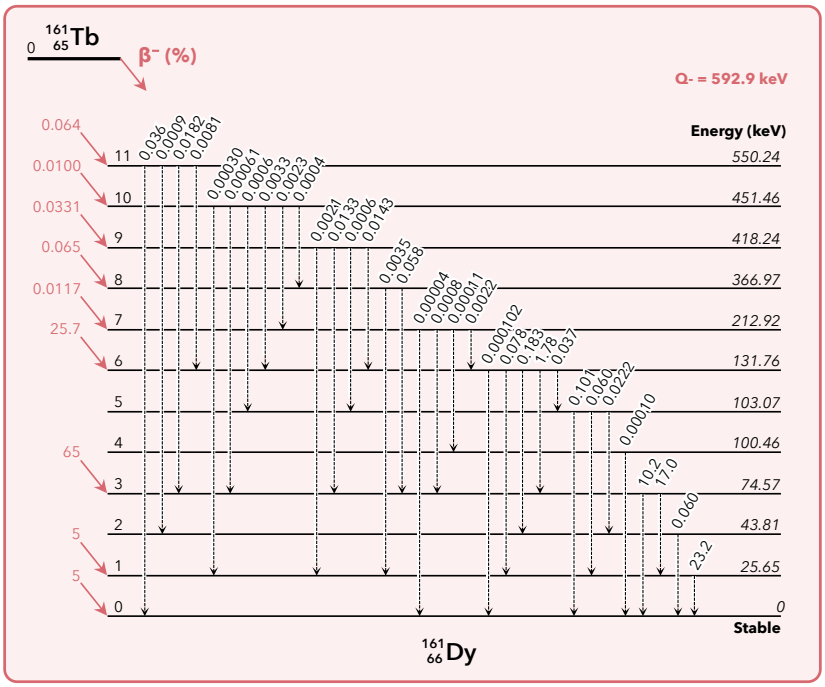

FIGURE 2.2. Decay scheme for ^{161}Tb, created with data from LARAWEB (54).

TABLE 2.4. Photon emission energies (X-rays and selected γ) with their corresponding yields for ^{161}Tb and ^{177}Lu, respectively (53,54). Emissions proposed for imaging (29,56) are highlighted in bold text*.

		^{161}Tb		^{177}Lu	
Photon emissions		E (keV)	Yield	E (keV)	Yield
X-rays	L	7.2	22%	8.9	3.20%
	Kα₂	**45.2***	6.28%	54.6	1.59%
	Kα₁	**46.0***	11.20%	55.8	2.78%
	Kβ₁	**52.2***	3.60%	63.3	0.92%
	Kβ₂	53.6	0.94%	65.1	0.25%
Selected γ-emissions		25.7	23.2%	71.6	0.1726
		28.7	0.037%	**113***	6.2%
		43.8	0.06%	137	0.047%
		48.9*	17.0%	**208***	10.38%
		57.2	1.78%	250	0.2012%
		74.6*	10.2%	321	0.216%
		77.4	0.06%		
		87.9	0.183%		
		103	0.101%		
		106	0.078%		
		292	0.058%		
		550	0.036%		

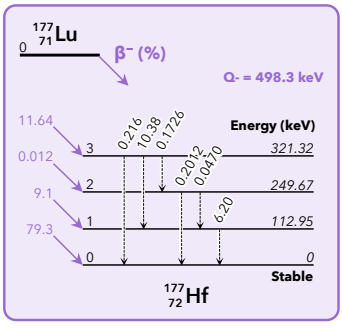

FIGURE 2.3. Decay scheme for ^{177}Lu, created with data from LARAWEB (53).

As Auger electron emission competes with X-ray emission, ^{161}Tb also exhibits some high-yield X-rays, as can be seen in Table 2.4. Each respective K-shell X-ray emission is approximately four times more likely for ^{161}Tb than for ^{177}Lu, while the L-shell X-ray emission is roughly seven times more likely.

Altogether, the β^- decay of ^{161}Tb results in a large cascade of photon and electron emissions. Importantly, the low-energy conversion and Auger electrons have a high interaction probability, leading to a high linear energy transfer (LET) and, consequently, substantial absorbed doses at short distances.

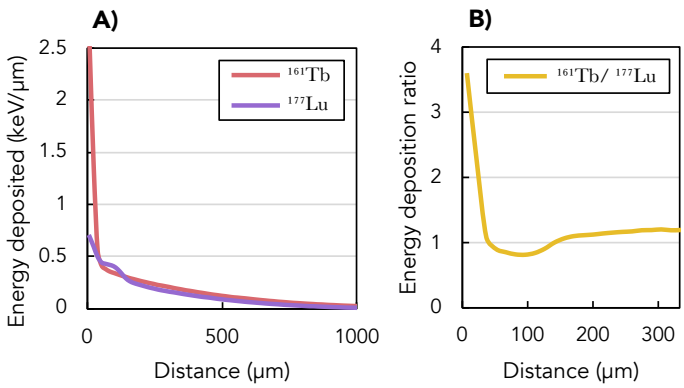

FIGURE 2.4. Energy deposition profiles (energy per unit distance as a function of distance) for ^{161}Tb and ^{177}Lu (A), as well as the ratio between them (B), modeled using Monte Carlo simulation for a point-source in soft tissue with all emissions (β^-, γ and X-rays, Auger and conversion e^-) included. The contribution from low-energy electrons, particularly pronounced for ^{161}Tb, can be seen at short distances (< 40 µm). Beyond this, the energy deposition is similar; ~1 in (B).

As shown in the energy deposition curves in Figure 2.4, the ^{161}Tb decay gives rise to a distinct "*dose boost*" within the first 40 µm. For reference, a typical human cell has a diameter of ~10 µm (57). Beyond this range, the energy deposition becomes comparable to that of ^{177}Lu. It is these characteristics that make ^{161}Tb particularly attractive: the combination of high-LET, short-range electron emissions—more suitable for targeting small cell clusters or single cancer cells—and the longer-range β^- emissions, providing exposure of larger tumors.

2.3 THE GAMMA CAMERA

The first ever γ-camera was constructed by Hal Anger in 1957 (8), and would become revolutionary to the field of nuclear medicine. Despite its early design, the core principles of the system have largely persisted. Today, the device remains a cornerstone of nuclear medicine, playing an essential role in diagnosing conditions such as cardiac disease, bone metastases, and thyroid disorders. In radionuclide therapy, the γ-camera is used to visualize the distribution of radiopharmaceuticals post-treatment, enabling both qualitative assessments of treatment response and activity quantification.

Essentially, SPECT refers to 3D γ-camera imaging and is further detailed in Section 2.4.

2.3.1 Principal Components

The major components of a traditional scintillation-based γ-camera can be summarized as follows:

1) Collimator
2) Scintillation crystal
3) Photomultiplier tubes (PMTs)
4) Electronics/Position circuitry
5) Computer

Figure 2.5 illustrates these components in relation to the formation of a planar 2D image (i.e., *a projection*).

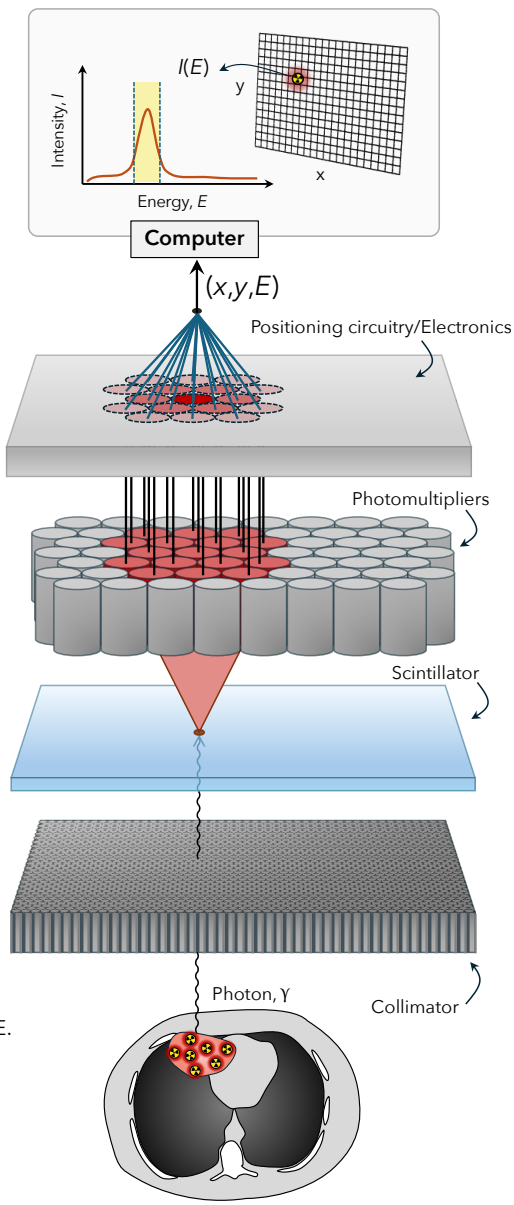

FIGURE 2.5. Schematic illustration of the basic principles of the image formation in γ-camera imaging. Incident photons generate a signal though scintillation. The produced light is collected and processed, giving an output signal consisting of the detection site, (x, y), and its corresponding energy, E.

In brief, an incoming photon will travel through the collimator and deposit its energy in the crystal, stimulating the emission of low-energy scintillation photons. The crystal is encased in a reflective material, allowing the photons to be directed toward the photomultiplier tubes (PMTs). Between the crystal and the PMTs, a light guide ensures efficient transmission of scintillation photons.

When the scintillation photons strike the photocathode of a PMT, electrons are released via the photoelectric effect. Inside the PMT, these electrons are accelerated and multiplied by a series of dynodes, amplifying the signal before reaching the anode, where the accumulated electrons generate an electrical current. This signal is processed and digitalized by a series of electrical components, e.g., pulse-height amplifiers (PHAs) and analogue-to-digital converters (ADCs), ultimately giving a signal with an amplitude proportional to the energy deposited in the crystal, E.

As the scintillation light is emitted isotropically (i.e., in all directions), a single event will be detected by multiple PMTs. To determine the position of the interaction, the positioning circuitry analyzes the distribution of signals among the PMTs, assigning (x, y) coordinates to the event—referred to as *Anger logic (58)*.

The output contains both the energy and spatial coordinates, (E, x, y), which are processed by a computer to generate an image. In the image generation, additional post-processing is applied, such as corrections for non-linearities (i.e., uneven PMT amplification) and non-uniformities (i.e., variations in detection efficiency across the image FOV).

Due to stochastic variations in the detection process, the pulse amplitude will vary slightly from event to event. Consequently, imaging a discrete photon energy gives rise to a Gaussian-shaped energy peak (rather than a sharp spike). To generate the final image, only events within a predefined energy range—referred to as an energy window—are selected. This helps capture relevant events while rejecting unwanted ones. And with that, we have obtained our projection.

2.3.2 Collimation

The collimator is a crucial component of the γ-camera that has a significant impact on the resulting image quality. Simply put; to determine the origin of a photon, we must know the direction in which it traveled to reach the detector. The collimator acts as a filter, allowing only photons traveling in a specific direction to reach and interact with the crystal.

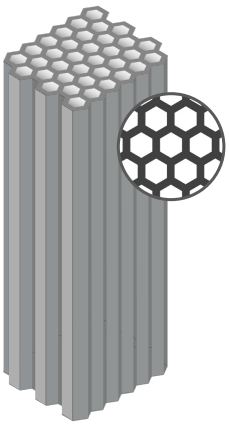

FIGURE 2.6. A parallel-hole collimator with hexagonally shaped holes.

Collimators are made of a material with high density and atomic number (typically lead) and consist of holes and walls (or *septa*) arranged in a specific pattern. In most applications, parallel-hole collimators are employed. In this design, the holes and septa are parallel to each other, permitting only photons incident perpendicularly—or nearly perpendicularly—to the detector surface to pass through.

Commercial γ-camera systems usually come with a set of collimators, commonly characterized as *low-energy*, *medium-energy*, *high-energy*, or special-purpose variations thereof. What sets them apart are the dimensions of the holes and septa. Generally, low-energy collimators (used for low photon energies) have narrow, shallow holes and thin septa. Conversely, high-energy collimators (used for high photon energies) have large holes and long, thick septa to efficiently absorb unwanted emissions.

Selecting the optimal collimator is not straightforward; trade-offs are essentially always required. In essence, a certain amount of absorbing material is necessary to block photons traveling in unwanted directions. However, increasing the amount of material reduces the space available for detecting photons of interest, leading to lower sensitivity and/or degraded spatial resolution.

Importantly, all photons emitted by the imaged nuclide must be considered—not only those used for imaging. High-energy photons can penetrate the septa (referred to as *septal penetration*), undergo scattering, and register within a lower photopeak window, thereby contributing to image degradation (more on this in Section 2.3.5).

In summary, collimator selection requires balancing resolution, sensitivity, and the need to minimize penetration—making it a crucial factor in optimizing image quality.

2.3.3 Sensitivity

Sensitivity is a key performance characteristic in γ-camera imaging. It is typically expressed as the number of recorded counts per unit activity (e.g., [cps/MBq]) and is influenced by several factors.

A key factor is the photon emission probability (i.e., *yield*) of the radionuclide. A higher yield leads to higher count rates and, therefore, greater sensitivity (i.e., as per unit activity). This can pose a challenge for theragnostic radionuclides like ^{177}Lu or ^{161}Tb, as their imageable emissions have relatively low yields (~10–15%) (*53*,*54*), compared to diagnostic nuclides like ^{99m}Tc, which emits photons in nearly every decay (*59*). This is a recurring theme in post-therapeutic imaging: **we must make the most of the emissions we have, even if they are not ideal**. In this context, that means recognizing that lower emission probabilities lead to decreased sensitivity, and a greater susceptibility to image noise.

Secondly, the detector material plays a major role. As previously mentioned, traditional γ-cameras rely on the principle of scintillation: incoming radiation interacts with the crystal, and the deposited energy is re-emitted as light in the visible to ultraviolet range. The most widely used scintillator material is thallium-doped sodium iodide, NaI(Tl), which is well known for its high light yield (*60*), contributing to relatively good sensitivity.

There is also a strong dependence on photon energy. For NaI(Tl), peak detection efficiency is typically achieved at approximately ~100 keV (*61*). At higher photon energies, sensitivity decreases due to the reduced photoabsorption cross-section. Conversely, at lower photon energies, sensitivity is also reduced, e.g., due to increased self-absorption.

Naturally, the thickness of the crystal also impacts sensitivity. Common crystal thicknesses are 3/8” (9.525 mm) and 5/8” (15.875 mm), where a thicker crystal increases the likelihood of full absorption and thus improves sensitivity. This is especially advantageous for higher photon energies, where the photoabsorption cross-section is lower. Other hardware-related components also contribute to sensitivity, e.g., the performance of the PMTs in terms of amplification gain.

As previously touched on, collimator design is a critical factor when it comes to sensitivity: wider and shorter holes will allow more photons to reach the crystal, resulting in higher sensitivity. Conversely, collimators with narrower and longer holes (which provide better spatial resolution) will produce a lower sensitivity.

2.3.4 Resolution

Another crucial γ-camera characteristic is resolution, which broadly describes the system's ability to discriminate between signals of different origins. This may refer to:

1) *Energy resolution*: The ability to accurately differentiate between photons of different energies, usually characterized by the width of the recorded photopeak.
2) *Spatial resolution*: The level of detail or "sharpness" in the image; that is, the ability to distinguish areas of uptake that are close in space.
3) *Temporal resolution*: The system's ability to separate pulses recorded close in time, typically characterized by the dead-time constant.

Each of these aspects plays an important role in both visual image quality and quantitative accuracy. Temporal resolution and dead time are addressed in detail in Section 2.3.6.

Energy resolution is, as previously discussed, influenced by stochastic variations in the detection process, resulting in a Gaussian-shaped peak in the acquired spectra. The width of the peak depends on the incoming photon energy; higher photon energies lead to broader peaks, making it more difficult to distinguish true events. In recent years, alternative detector materials, e.g., cadmium zinc telluride (CZT), have become increasingly popular (62). CZT offers superior energy resolution compared to NaI(Tl), making the discrimination of scattered events easier.

Limitations in spatial resolution constitute a major source of degradation in γ-camera imaging. While also influenced by intrinsic properties (e.g., crystal thickness), spatial resolution is largely governed by the collimator. This is determined by the so-called angle of acceptance—that is, the slight angle at which photons are permitted to pass through the collimator holes—defined by the geometry of the holes and septa. Importantly, this introduces a geometric dependency of the resolution, referred to as the *collimator-detector response* (CDR). At greater source-to-collimator distances, the acceptance angle allows photons to deviate more from their true origin, leading to increased blurring.

The effects of limited spatial resolution—referred to as partial volume effects (PVEs)—are discussed in further detail in Section 2.4.3.3.

2.3.5 Septal Penetration and Scatter

In γ-camera-based image quantification, we generally want to assume that detected events correspond only to primary photon emissions—i.e., photons that have traveled directly from the emission site and fully deposited their energy in the crystal in a single interaction. If this assumption held true, image-based quantification would be straightforward, as the measured signal would be directly proportional to the activity in the corresponding region of the patient (assuming no attenuation or other degradation).

Unfortunately, reality is more complex. The signal detected within the photopeak will always contain a fraction of invalid events due to photon scattering and, for some nuclides more than others, septal penetration. This disrupts the desired proportionality between measured counts and true activity, which has both qualitative and quantitative implications.

To understand this, we need to revisit some fundamental particle physics. When talking about scatter, we most often refer to photons that have undergone *Compton scattering*. This is a process in which a photon transfers part of its energy to an electron, causing the photon to change direction and lose energy. The energy loss is given by:

$$h\nu' = h\nu \cdot \frac{1}{1 + \frac{h\nu}{m_0 c^2}(1 - \cos(\theta))} \qquad \text{Eq. (2.1)}$$

where $h\nu$ and $h\nu'$ denotes the photon energy pre- and post-scattering, m_0 is the electron rest mass, c the speed of light, and θ the angle of deflection. The likelihood of a photons scattering at θ (i.e., the differential cross section) is given by the Klein–Nishina formula, as follows:

$$\frac{d\sigma(\theta)}{d\Omega} = \frac{r_e^2}{2} \cdot \left(\frac{h\nu'}{h\nu}\right)^2 \cdot \left(\frac{h\nu}{h\nu'} + \frac{h\nu'}{h\nu} - \sin^2(\theta)\right) \qquad \text{Eq. (2.2)}$$

where r_e is the classical electron radius, and other notations are the same as above.

Essentially, what these two equations tell us is that 1) the angle of deflection increases with the amount of energy transferred, and 2) low-energy photons tend to scatter more isotropically, whereas high-energy photons scatter more in the forward direction (i.e., with a smaller energy loss).

Scatter events can broadly be categorized into two subgroups: 1) scatter that occurs within the patient and 2) scatter that occurs within the camera (i.e., the collimator, crystal, or other components), see Figure 2.7.

In the context of imaging, the issue with scattering arises when scattered photons are close in energy to relevant primary events, i.e., when they fall within the defined photopeak window. This can occur either when a photon scatters at a small angle, resulting in only a slight energy loss, or when a higher-energy photon scatters at a larger angle and/or multiple times (either in the patient or within the camera).

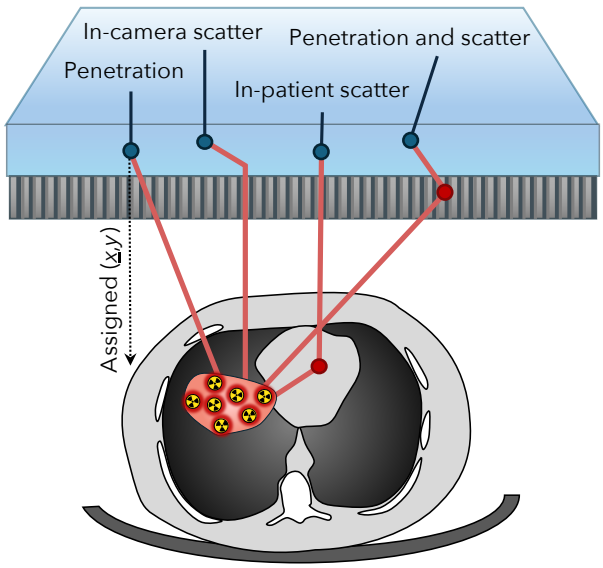

FIGURE 2.7. Different types of invalid scintillation events, resulting from scatter and penetration.

In this aspect, the energy resolution of the γ-camera constitutes a major limitation; with perfect energy resolution, true primary events would be easily distinguishable from scattered events. However, since all events produce a bell-shaped response, the signal in the energy spectrum will overlap, making this distinction impossible.

As implied, scatter is a major source of degradation in γ-camera imaging. Visually, scattered photons reduce image contrast, as their assigned (x, y) coordinates do not correspond to the true origin of the decay (see Figure 2.7). More critically, scattered photons will introduce a variability in sensitivity, complicating quantification. This variability depends on both source geometry and patient anatomy—e.g., larger patients will generate more in-patient scatter.

Additionally, the likelihood of penetration (and subsequent scatter) increases exponentially as the source-to-collimator distance decreases, introducing a distance dependence to an otherwise spatially independent sensitivity.

There are several ways to mitigate the effects of scatter, either during or post-acquisition. First, using a narrower and/or skewed photopeak window will reduce the fraction of scattered counts recorded. However, this inevitably leads to the rejection of some true primary events, also reducing sensitivity. For scatter resulting from septal penetration, the most effective approach is to minimize its occurrence at the acquisition stage by selecting an appropriate collimator. However, as discussed earlier, the collimator selection involves a trade-off between resolution and sensitivity.

Post-acquisition options include various scatter correction methods and/or applying a calibration factor that accounts for the contribution of scatter. While these approaches can be effective, there are associated challenges that must be addressed (discussed further in Section 2.4.3.2). In summary, scatter remains a major obstacle to accurate quantification, particularly for high-energy nuclides where septal penetration is more pronounced.

2.3.6 Dead Time

Another important aspect of γ-camera quantification is *dead time*. The term is quite self-explanatory; dead time occurs whenever the incoming signal is too large to be processed in real time, rendering the system inactive (i.e., "dead") for a period of time. Dead time can occur either due to limitations in the response time of the detector (e.g., related to the scintillation or transport of charge carriers) or the time required to process the signal and handle the acquired data (e.g., the pulse-shaping) (63). Dead time is commonly quantified using the dead-time constant, τ, defined as the minimal time required to separate two incoming pulses.

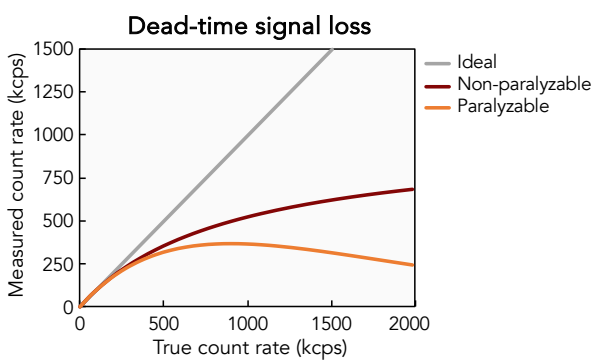

FIGURE 2.8. Example of the count rate response for paralyzable and non-paralyzable systems with identical dead-time constants (τ = 1 μs).

Systems can be categorized as either *paralyzable* or *non-paralyzable* (63), see Figure 2.8. In the non-paralyzable case, the system becomes unresponsive for a fixed period. During this time, any new incoming pulses are omitted. Ultimately, the system becomes saturated, and the measured count rate flattens out. Mathematically, this behavior can be described as:

$$R = \frac{R_T}{1 + \tau R_T} \qquad \text{Eq. (2.3)}$$

Where R is the recorded count rate, and R_T is the true count rate.

For paralyzable detectors, the system also becomes unresponsive; however, any additional pulses that occur during this period further prolong the dead time. Eventually, the observed count rate starts to **decrease** as activity increases, see Figure 2.8. In that case, the following relationship holds:

$$R = R_T \, e^{-\tau R_T} \qquad \text{Eq. (2.4)}$$

Using the same notation as above.

The appearance of dead-time-related signal loss (e.g., paralyzable or non-paralyzable) depends on the specific components that impose performance limits. Modern γ-cameras are complex systems and differ substantially from vendor to vendor, making it difficult to provide a universal explanation for the exact causes and manifestations of dead time.

That said, most γ-cameras function as paralyzable detectors (64, 65). However, many systems exhibit more unpredictable high count rate responses, including *saturation* characterized by a sudden sharp decline in observed count rate (66–68). Some systems include built-in corrections that mitigate dead-time effects to some extent; however, signal degradation remains inevitable at high count rates. Therefore, understanding your system's limitations is crucial for accurate quantification.

In post-therapeutic SPECT imaging, dead time is generally not a major concern. Although injected activities are much higher than in diagnostic procedures, the recorded count rate remains relatively low, e.g., due to lower sensitivity (as discussed in Section 2.3.3). Additionally, post-therapeutic imaging is mostly performed at extended times after administration when much of the activity has been eliminated. Nevertheless, dead time can still be an issue in early time-point imaging.

It should be noted that dead time is primarily dictated by the *wide-spectrum* (or *full-spectrum*) count rate; a potential issue for some theragnostic nuclides. For example, ^{99m}Tc emits almost exclusively 140 keV photons, meaning that a majority of the recorded signal will fall within the photopeak window.

In contrast, ^{161}Tb emits a range of high-intensity X-rays and low-yield, high-energy γ-photons that are *not* used to generate projection data but also contribute to dead time, as they too must be processed. This difference in wide-spectrum sensitivity makes dead time highly nuclide-specific, ultimately influencing the amount of activity that can be imaged.

Efficient correction for dead time requires proper system characterization, i.e., that the relationship between the observed and the "*true*" count rate is established. Count rate performance can be assessed either intrinsically or extrinsically, i.e., with or without the collimators attached.

One commonly used approach for characterizing dead time is the decaying source method, which involves repeatedly measuring a high-activity phantom as it decays over time. Another method, the dual-source technique, measures the difference in count rate between two sources at varying activity levels (69). Once characterized, dead time can be accounted for. In SPECT imaging, these corrections can be implemented either pre- or post-reconstruction (66), generally yielding an effective compensation.

2.3.7 Uniformity

Uniformity is an image quality measure that refers to the spatial consistency of the γ-camera response across the field-of-view (FOV). When irradiated homogeneously, the camera should—ideally—produce a perfectly uniform image. In reality, the signal will be amplified in some regions, and reduced in others. These inconsistencies are referred to as non-uniformities. During reconstruction, non-uniformities will propagate along the corresponding lines of response, resulting in ring artifacts (see Figure 2.9), compromising both visual image quality and quantitative accuracy.

Non-uniformities are commonly categorized as either intrinsic or extrinsic. Intrinsic non-uniformities are associated with "*built-in*" components of the camera, whereas extrinsic non-uniformities arise from the collimator. Common sources of non-uniformities include crystal deterioration, poor PMT tuning, faulty optical couplings, and/or defects in the collimator (70).

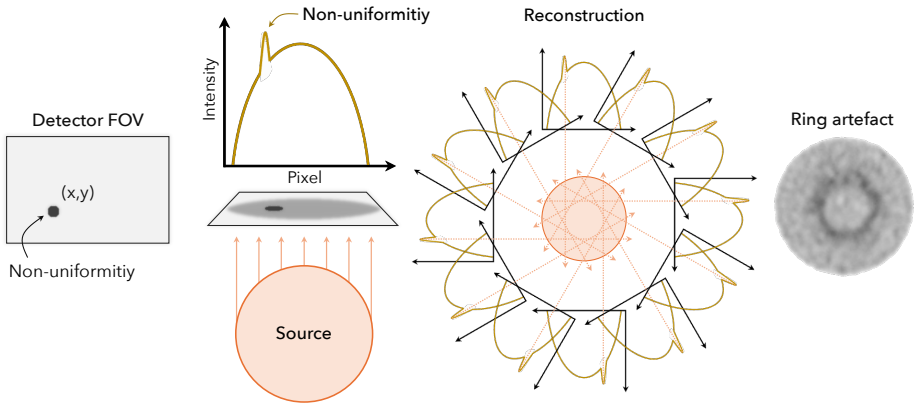

FIGURE 2.9. The formation of uniformity artefacts in SPECT. A detector non-uniformity—here shown as an increased signal in a specific (x,y) region—alters the system's sensitivity profile. During reconstruction, the non-uniformity is back projected along the corresponding line of projection, causing a ring in the reconstructed image.

Another potential source of non-uniformity is faulty linearity—i.e., when the system fails to correctly determine the (x, y) position of incident photons. In planar imaging, non-linearity can cause straight lines to appear warped. This effect is typically more pronounced for high-energy nuclides, as scintillation generally occur deeper within the crystal, illuminating fewer PMTs and thus making Anger logic positioning more challenging (*61*). However, non-linearity can also arise due to dead time.

Non-uniformities are corrected for using so-called uniformity maps, which are acquired through homogeneous irradiation of the detector FOV. This can be done either intrinsically (with the collimators detached) using a distant point source, or extrinsically (with the collimators attached) using a flood-source phantom.

2.4 SINGLE PHOTON EMISSION COMPUTED TOMOGRAPHY

Although groundbreaking, Anger's original γ-camera design had one major limitation: it only allowed for 2D image representations (*projections*) of 3D source distributions. This limitation was addressed by Kuhl and Edwards in 1963 with the invention of Single Photon Emission Computed Tomography (SPECT) (9).

In SPECT imaging, the γ-camera is used to acquire projections from several angles (or *views*) around the source, and a 3D image can be generated via *reconstruction*. Key aspects of SPECT acquisition and reconstruction are discussed below.

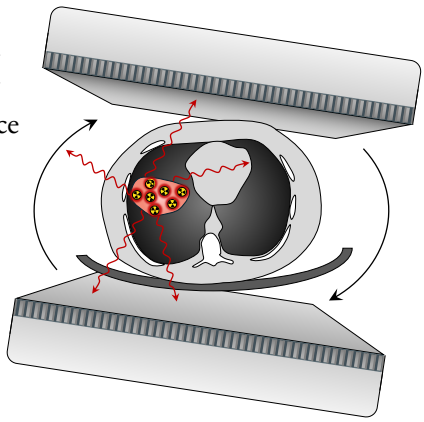

FIGURE 2.10. Illustration of a SPECT acquisition with gantries rotating around a patient.

2.4.1 Acquisition Protocols

Modern SPECT systems come in various shapes and sizes; however, dual-headed γ-camera systems are the most common*. In these systems, two opposing detector heads (or gantries) rotate synchronously around the patient, enabling a 360° acquisition of projection data (180°/detector) through a fixed number of views (an acquisition technique called *step-and-shoot*).

As spatial resolution decreases with distance, minimizing the space between the detector and the patient is crucial. Hence, modern systems offer *body-contouring*, where the detectors follow the patient's contour while rotating. The *radial distances* (i.e., the distances between the detectors and the center of rotation) are stored and used to correct for the distance-dependent resolution loss.

Today, most systems are SPECT/CT hybrids (as illustrated in Figure 2.11), allowing a CT scan to be performed in conjunction with the SPECT acquisition. The CT image provides anatomical information that serves multiple purposes: it is co-registered with the SPECT image for clinical evaluations (e.g., to localize radioligand uptake), used in dosimetry for organ segmentation, and incorporated into the reconstruction process for attenuation correction (see Section 2.4.3.1).

**Some newer systems, sometimes referred to as 360° SPECT/CT cameras (e.g., the VERITON Multi-CZT and GE StarGuide CZT cameras), use a completely different configuration. These systems feature twelve separate detector arms, evenly distributed around the patient, enabling a simultaneous 360° acquisition (unlike the traditional step-and-shoot) and allowing for significantly reduced acquisition times (71).*

The number of projections, along with the time per projection, are key acquisition parameters. Clinical SPECT acquisition protocols commonly use 60–120 projections, corresponding to an angular sampling of 3°–6°. A common acquisition time is ~30 seconds per projection, giving a total scan time of around 15–30 minutes per bed position (i.e., 60–120 projections × 30 seconds ÷ 2 detectors)*.

A matrix size of 128×128 with a pixel size of ~4×4 mm is commonly employed. While larger matrices (e.g., 256×256, ~2×2 mm) can be visually appealing (as the image grid becomes less apparent), they typically do not improve spatial resolution, as this parameter is fundamentally limited by the system and remains notably larger than the pixel size (72). Moreover, larger matrices increase noise and require longer reconstruction times (73).

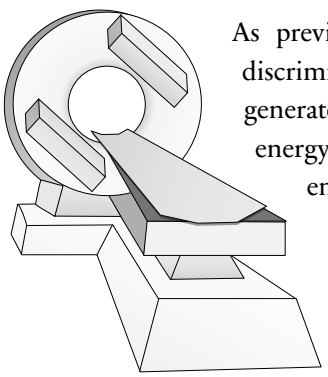

As previously touched on, energy windows are defined to discriminate between photons of different energies and generate the final projection. A window of ±10% (i.e., photon energy ± photon energy × 0.10) is commonly used for the emission, or emissions, of interest. In addition, one or two adjacent windows are commonly defined alongside the photopeak window and are used for window-based scatter correction, as discussed in Section 2.4.3.2.

FIGURE 2.11. Illustration of a dual-headed SPECT/CT hybrid system.

**Keeping the acquisition time to a minimum is desirable in practice (especially when multiple bed positions are required), as it is less resource-intensive and promotes patient comfort. One way to achieve this is by reducing the number of acquired projections. Generally, it is recommended that the number of projections be kept roughly equal to the matrix size to avoid artifacts (72, 73). That said, it has been shown that reducing the number of projections has limited importance in quantification (74). Regardless, reducing the number of views does degrade image quality by increasing noise—unless compensated by longer acquisition times. It has demonstrated that deep learning-based approaches can enable reduced angular sampling while maintaining image quality by generating synthetic intermediate projections (75–77). Deep learning-based denoising has also been shown as a viable approach for mitigating noise in γ-camera imaging (78,79).*

2.4.2 Iterative Reconstruction

Once the projection data has been acquired, the SPECT image can be *reconstructed*. Although introduced several decades ago, the Maximum Likelihood Expectation Maximization (MLEM) (80) and its accelerated variant, Ordered Subsets Expectation Maximization (OSEM) (81), remain the most widely used algorithms.

In essence, these iterative algorithms follow the same general pattern:

1) Initialize by providing an arbitrary source distribution (e.g., a uniform matrix of ones).
2) Forward-project the estimate of the source distribution to generate projections (3D → 2D).
3) Compare to measured projection data on a pixel-by-pixel basis.
4) Back-project the differences to update the source distribution (2D → 3D).
5) Repeat!

With OSEM, the image estimate is updated based on only a *subset* of the projection data (rather than the full dataset, as in MLEM) allowing for quicker convergence.

The quality of a SPECT image is largely influenced by the number of updates employed in the reconstruction. As the number of updates increases, the image converges toward a more "likely" solution (i.e., one that maximizes the likelihood function). However, a more likely solution is not necessarily more *accurate*.

In general, increasing the number of updates improves spatial resolution. Convergence is spatially dependent; small objects, or those adjacent to regions of high activity, tend to converge more slowly than large, isolated uptakes (*82*). However, while a high number of updates improves resolution, it also amplifies image noise. Qualitative applications (e.g., clinical visual assessments) require a balance between noise suppression and sufficient resolution (often in terms of maximizing the signal-to-noise-ratio, SNR).

In quantitative applications, noise is often less critical—if the volume of interest (VOI) is sufficiently large, the mean value within it typically remains accurate. That said, noise can become a limiting factor for small VOIs or in low-count regions (*82*) Furthermore, since both OSEM and MLEM are strictly non-negative algorithms, positive biases can occur in such regions, leading to an overestimation of activity (*73*).

Regardless of the application (i.e., qualitative or quantitative), evaluating image quality in relation to the number of updates is a crucial step in reconstruction optimizations.

2.4.3 Methods of Compensation

Due to the pronounced image degradation associated with γ-camera imaging, SPECT was once considered a non-quantitative imaging modality (83). However, with improved hardware and better methods of compensation, highly accurate SPECT-based quantification has since been proven feasible.

2.4.3.1 Correction for Attenuation

Although less problematic today, attenuation used to be a significant source of image degradation in SPECT (84). Essentially, a large fraction of the photons emitted within a patient will be lost due to attenuation; the greater the emission depth and the lower the photon energy, the more pronounced the effect will be. In non-attenuation-corrected reconstructions, this leads to artifacts where signal is falsely allocated to the edges of objects (i.e., to pixels corresponding to photon paths inherently characterized by less attenuation).

As previously mentioned, modern SPECT systems are hybrids, enabling accurate CT-based mapping of the patient's attenuation properties. By acquiring a low-dose CT alongside the SPECT scan, Hounsfield Unit (HU) values are obtained and converted into linear attenuation coefficients. These coefficients allow calculation of the cumulative attenuation along all acquisition angles (on a pixel-by-pixel basis). By incorporating this information in the reconstruction, attenuation can be effectively compensated for.

2.4.3.2 Correction for Scatter and Penetration

While correcting for attenuation is relatively straightforward, accounting for scatter and penetration can be more challenging. As detailed in Section 2.3.5, scattered photons will degrade γ-camera image quality, and can introduce substantial errors in SPECT quantifications.

Several scatter correction methods exist, the most common being *window-based*. These methods use additional energy windows adjacent to the photopeak window to acquire projections that are subtracted from the primary photopeak data.

In the Dual Energy Window (DEW) method (85), a lower adjacent window is used, and the correction is applied pixel-wise to the projection data, $I(x,y)$, as:

$$I(x,y) = \mathrm{I}(x,y)_{EM} - \mathrm{k} \cdot \mathrm{I}(x,y)_{SC1} \qquad \text{Eq. (2.5)}$$

Where EM denotes the photopeak window, SC1 the lower scatter window, and k is a scaling factor that can be adjusted to better approximate the scatter component.

While easy and convenient to apply, DEW has limited efficacy, especially in the presence of septal penetration. As discussed in Section 2.3.5, penetration causes downscattered photons to leak into the photopeak window. In such cases, the Triple Energy Window (TEW) method (*86*) may be used, employing both lower (SC1) and upper (SC2) scatter windows:

$$I(x,y) = I(x,y)_{\mathrm{EM}} - \left(\frac{I(x,y)_{SC1}}{\Delta E_{SC1}} + \frac{I(x,y)_{SC2}}{\Delta E_{SC2}}\right) \cdot \frac{\Delta E_{EM}}{2} \qquad \text{Eq. (2.6)}$$

Where ΔE denotes the window width, and other notations are the same as above.

The TEW method allows for a better estimation of the spatial distribution of down-scattered counts. Still, both DEW and TEW are inherently limited in accuracy. The adjacent windows serve only as surrogates for the true scatter component, which varies spatially and is heavily dependent on geometry. As such, it's difficult to optimize these methods for all possible imaging conditions. In addition, the pixel-wise subtraction will cause increased image noise (*87*).

A more robust approach is to use MC-based simulation (see Section 2.5). In MC-based reconstructions, scatter and penetration—both within the patient and in the detector—can be accurately modeled and thus accounted for (*88*). Such simulations are, however, computationally intensive. While simulation times can be reduced, e.g., via GPU-based parallelization (*89*), specialized hardware is typically required, which limits widespread adoption. More recently, AI-based methods have emerged as a promising alternative, offering faster processing while maintaining good accuracy (*90*–*92*).

2.4.3.3 Partial Volume Effects

Partial volume effects (PVEs) arise as a consequence of the system's limited spatial resolution, and can also constitute a major source of error in SPECT-based quantification. Essentially, PVEs refer to when signal is shared among neighboring regions—either at the pixel level or on a larger scale. There are two main types of PVEs: *spill-in*, where signal from outside a region contributes to the measured activity within it (resulting in overestimation), and *spill-out*, where signal originating within a region is allocated elsewhere (resulting in underestimation).

In quantification, two general strategies can be applied to mitigate PVEs:

1) Minimize the impact by optimizing the reconstruction algorithm and/or segmentation approach.
2) Apply corrections to account for spill-in or spill-out within a segmented volume.

Pertaining to 1), an important factor influencing PVEs is the collimator-detector response (CDR). As previously discussed, spatial resolution degrades with increasing distance from the collimator. These effects can be modeled (e.g., via PSF convolution, guided by the recorded radial distances) and incorporated into the reconstruction—commonly referred to as resolution recovery (RR). While RR can effectively improve resolution, it may also introduce Gibbs artifacts (*93*). More recently, AI-based methods have been explored as an alternative for improving spatial resolution, thus mitigating PVEs (*79*,*94*).

In quantification, an effective PVE workaround is to use so-called small-VOI approaches, where the activity concentration is determined using a small VOI within the tissue of interest, thereby minimizing the impact of spill-out effects (*95*). This method has proven robust, e.g., for kidney dosimetry (*96*–*98*).

Concerning 2), a commonly used approach involves recovery coefficients (RCs). The RC is defined as the ratio between measured activity and true activity and is often used for image quality characterization purposes (i.e., as a measure of spatial resolution). However, as implied by the mathematical definition, dividing a measured value by the appropriate RC will (in theory) restore the true activity.

Unfortunately, PVE correction using RCs is not straightforward. Traditional approaches involve physical phantom measurements using simple geometries (e.g., spheres of various sizes), allowing the RC to be modeled as a function of volume. However, applying such sphere-based corrections directly to patient data is not ideal, as PVEs are highly geometry-dependent, with spheres being less affected than more complex geometries (*99*,*100*).

Advancements in 3D printing have made it possible to conduct physical phantom studies measurements with more realistic geometries (*101*–*103*), enabling new opportunities for accurate RC determination. In addition, MC-based simulation approaches can be employed to model geometry-dependence of RCs (*104*).

2.5 MONTE CARLO SIMULATION

Monte Carlo (MC) modeling is a computational technique used to solve complex mathematical problems that are inherently unpredictable, e.g., the interaction of radiation with matter. The fundamental principle is to perform repeated computations based on random number sampling. The more computations performed, the better the approximation of the unknown variable will be.

The γ-camera image formation is a stochastic process that can be effectively modeled using MC-based methods. By simulating the path of each photon—from emission to detection—highly realistic projection data can be generated, incorporating image-degrading effects such as attenuation, scatter, septal penetration, and loss of resolution.

2.5.1 Basic Principles for γ-Camera Simulation

A well-established example of an MC-based code for γ-camera simulation is the SIMIND framework: first published in 1989 (*105*), it has since become a widely adopted tool in nuclear medicine research.

Building on the SIMIND architecture, our research group developed the Sahlgrenska Academy Reconstruction code (SARec) (*89*)—an MC program for accelerated SPECT simulation and reconstruction. SARec is implemented in Compute Unified Device Architecture (CUDA) and supports parallelized simulations on up to four graphics processing units (GPUs), enabling both fast and accurate MC-based modeling.

In MC-based reconstructions, simulation is commonly incorporated into the forward projection, allowing for image-degrading effects to be realistically modeled (as opposed to the methods outlined in Section 2.4.3).

Below is a summary of the MC simulation process, along with key definitions of simulation parameters related to: (1) input data, (2) photon emission, (3) photon interaction, (4) photon detection, and (5) additional factors relevant to this work.

2.5.1.1 Input Data

The key inputs for MC-based simulations are:

a) An activity map: A 3D image representing the spatial distribution of the radioactive source.
b) An attenuation map: A 3D representation of the source's matter composition.

In summary, photons are emitted based on the activity map, and individually tracked as they interact with the surrounding medium (as guided by the attenuation map). Depending on the application, the attenuation map can be derived from digital phantoms, e.g., XCAT (*106*), or clinical image data—such as the low-dose CT acquired in conjunction with SPECT. The HU values are used to estimate density and effective atomic number via look-up tables. These parameters are then used to calculate interaction probabilities based on pre-tabulated cross sections.

Upon reaching the detector, the likelihood of detection is computed, considering the probabilities associated with the factors described below.

2.5.1.2 Photon Emission

First, the relevant emissions must be defined in terms of *energy* and *yield*. Initially, these photons are randomly emitted in a 4π geometry (or sometimes in a more restricted solid angle). The number of simulated emissions—commonly referred to as the number of *photon histories*—is predefined. The higher the number of photon histories, the greater the statistical accuracy of the simulation.

Some photons will travel directly toward the detector without interacting with the surrounding medium. To reduce computational load, their emission is often restricted to a predefined solid angle (i.e., the *maximum angle*). This is based on the fact that photons emitted at large angles have a low likelihood of detection due to collimator absorption. Simulating such photons would therefore contribute negligibly to the final projection, while increasing computation time. This *restricted emission* is an example of a *variance reduction technique*—a procedure designed to minimize computational cost by omitting non-relevant photon emissions.

2.5.1.3 Photon Interactions

After emission, each photon is tracked as it interacts with the surrounding medium. Photons that are attenuated through absorption will—by definition—not contribute to the final image. Therefore, photons are forced to scatter (either coherently or incoherently, i.e., with or without energy loss) and ultimately reach the detector, even though the likelihood of such a path is low. The probability is subsequently accounted for by applying a weighting factor, calculated based on the scattering cross-sections corresponding to the relevant angle(s) leading to detection. This *forced interaction* is, once again, a form of variance reduction.

Another form of variance reduction involves restricting the number of allowed scattering events, using a predefined parameter known as the *scattering order*. Since the probability of detection decreases significantly with each scattering event, allowing an infinite number of scatter events would only increase the computational burden without effectively improving accuracy. The appropriate scattering order depends on photon energy and, more importantly, the presence of other higher-energy emissions that may cause downscattering.

2.5.1.4 Photon Detection

In the final step, all photons are forced to interact with the detector. The photon is directed within a predefined solid angle toward the detector surface (again, *variance reduction* through *forced detection*). The likelihood of the photon being detected is then calculated and used to weight its contribution to the final image.

Several factors influence the probability of detection. First, the likelihood of the photon passing through the collimator is determined by the *angular response function* (ARF), which is typically precomputed through simulation and stored as a look-up table. The ARF provides the transmission probability as a function of photon energy and angle of incidence.

Once the collimator interaction is accounted for, the probability of interaction within the scintillation crystal is calculated. This depends on parameters such as *crystal thickness*, *energy*, and *incident angle*. Additionally, scattering within the crystal or other detector components may be simulated.

2.5.1.5 Additional Factors

Properly simulating all possible types of scattering events—including scatter within the collimator, crystal, or surrounding components—can be difficult and computationally expensive. To address this, these effects can be approximated using a *scattering kernel* (89). This is a measured function that is convolved with the projection data to simulate the associated image-degrading effects, e.g., reduced image contrast.

Another critical factor that is challenging to properly simulate is the system's *energy resolution* (i.e., the broadening of peaks in the energy spectra). This is typically accounted for by applying an energy-dependent Gaussian function, which can either be measured experimentally or modeled analytically. As a final step, just as in physical imaging, an *energy window* is applied to select photons of interest for projection formation.

2.6 DOSIMETRY IN RADIONUCLIDE THERAPY

The possibility for post-therapeutic imaging provides radionuclide therapy with a distinct advantage over other systemic cancer treatments: it enables the study and quantification of patient-specific pharmacokinetics, allowing for the calculation of absorbed doses to both tumors and healthy organs-at-risk—i.e., *dosimetry*. This enables a level of treatment individualization that is simply not achievable with conventional systemic therapies.

In this context, dosimetry may be viewed as an exciting tool for research and clinical optimizations. However, when radionuclide therapy is regarded as a form of radiation therapy, dosimetry becomes an expected part of safe and effective treatment planning. This expectation is reflected in the legal framework, e.g., in Article 56 of the 2013/59/Euratom Directive (*107*), which states:

> ”*For all medical exposure of patients for radiotherapeutic purposes, exposures of target volumes shall be individually planned and their delivery appropriately verified taking into account that doses to non-target volumes and tissues shall be as low as reasonably achievable […]*”

Despite this clear directive, radionuclide dosimetry often remains neglected in clinical practice. Many centers do not perform dosimetry at all, while others apply it inconsistently or only in limited contexts. The reasons for this are multifaceted, including a lack of trained personnel or limited access to quantitative imaging tools.

A common criticism of dosimetry is that it remains too uncertain and resource-intensive to be clinically feasible. To address these concerns, several efforts have been undertaken, including the development of quantitative imaging guidelines and directives (*56*,*72*,*73*), proposals of more viable workflows (*108*), and harmonization initiatives aimed at reducing inter-center variability in absorbed dose estimates, e.g., by identifying and assessing the various sources of uncertainty that impair accuracy (*109*–*113*).

With these efforts, reliable and clinically feasible dosimetry is becoming increasingly attainable. However, reaching this goal requires thorough optimization and validation across all stages of the dosimetry process. Some key aspects of this process are discussed in this chapter.

2.6.1 General Workflow and Calibration

Dosimetry workflows can vary depending on institutional routines, available resources, and the overall purpose (e.g., clinical vs. research). Generally, the process follows these steps:

1) Patients are administered a prescribed activity, often based on a fixed regimen. For example, Lutathera (i.e., [^{177}Lu]Lu-DOTATATE) is usually given in four cycles of 7,400 MBq, spaced eight weeks apart.
2) After administration, patients undergo SPECT/CT imaging at one or multiple time points post-injection. Acquisition protocols may differ between centers, but should adhere to guidelines (if any exist).
3) The acquired image data is reconstructed and processed for dosimetry. This includes segmentation of relevant tissues, activity quantification, time-activity curve fitting, and absorbed dose computation.

A key requirement for quantitative SPECT is *system calibration*. Basically, calibration ensures that what we measure in terms of image counts can be accurately converted into activity. Although some vendors offer so-called "fully quantitative" imaging pipelines, these must still be validated. In practice, we rely on independent *phantom measurements* to establish the relationship between signal and activity.

The accuracy of calibration depends on several factors, e.g., relating to measurement geometry and reconstruction parameters (*114*,*115*). Importantly, phantoms must be adequately prepared, i.e., properly measured and weighed. A particularly critical—yet sometimes overlooked—aspect is the dose calibrator. This ionization chamber-based system is a routine workhorse in nuclear medicine, used to measure activity both prior to patient administration and often in the phantom measurements that underpin the calibration. Hence, its accuracy directly impacts all downstream steps of quantification and dosimetry. Understanding the limitations of the dose calibrator is crucial, especially for low-energy photon emitters such as ^{161}Tb, as they are more susceptible to attenuation (*116*). This results in a higher geometry-dependence, meaning that the activity readings can vary significantly depending on container type, volume, and positioning within the chamber.

Another key aspect in activity measurements is *traceability*, i.e., that equipment used is calibrated against national or international standards. Despite its importance, the infrastructure for traceability varies between countries, and many centers are effectively left to independently verify the accuracy of own equipment (*117*).

2.6.2 The MIRD Formalism

Absorbed dose, traditionally defined as the energy imparted per unit mass ($d\varepsilon/dm$), is a physical quantity that describes the energy deposited in a medium when exposed to ionizing radiation. In nuclear medicine, calculations of absorbed dose are performed according to the Medical Internal Radiation Dose (MIRD) formalism (*118*). The MIRD schema offers a dosimetric framework for internal radionuclide exposure, enabling absorbed dose assessments for virtually any geometry or region of tissue—from the organ level down to the cellular level—as well as voxelized structures in general.

Although the nomenclature may be somewhat startling at first, the basic principles behind the MIRD schema are rather intuitive. We just need to follow the energy! Doing so mandates the introduction of two key concepts: *source region* (r_S) and *target region* (r_T). The source region is the region in which the activity is located, while the target region is the region in which the energy from the radioactive decay is deposited, i.e., the region for which we want to determine the absorbed dose.

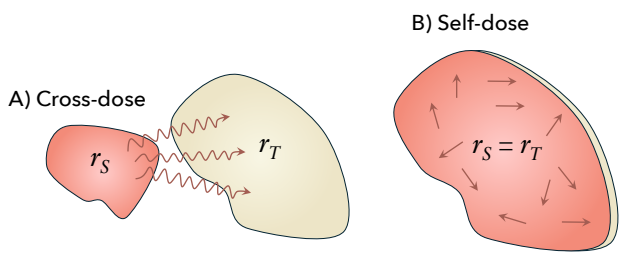

FIGURE 2.12. Illustration of the concepts of source and target regions. In the MIRD formalism, calculations of absorbed dose are performed by considering the energy deposited in the target region (r_T), emitted from the source region (r_S). The radiation may originate from a separate tissue or region ($r_T \leftarrow r_S$ = cross-dose), a scenario most relevant for photon emissions, or from within the tissue itself ($r_T \leftarrow r_T$ = self-dose), which is more pertinent to short-ranged charged particle emissions (as indicated by the arrows).

The mean absorbed dose to the target region [unit: Gy/kg or J] can be expressed as:

$$D(r_T) = TIA(r_S)S(r_T \leftarrow r_S) \qquad \text{Eq. (2.7)}$$

Where $TIA(r_S)$ is the *time-integrated activity*, representing the total number of decays within the source region during the relevant time period [unit: Bqs], and $S(r_T \leftarrow r_S)$ denotes the energy deposited in the target region per decay [unit: J/kg] (commonly referred to as the *S-value*).

The time-integrated activity, or TIA, can be calculated as:

$$TIA(r_S) = \int_{T_i}^{T_f} A(r_S, t)\, dt \qquad \text{Eq. (2.8)}$$

Where $A(r_S,t)$ is the activity within the source region as a function of time. The integration period $[T_i, T_f]$ is usually chosen as $[0, \infty)$. The S-value is defined as:

$$S(r_T \leftarrow r_S) = \frac{1}{M_{r_T}} \sum_i E_i Y_i \phi_i(r_T \leftarrow r_S) \qquad \text{Eq. (2.9)}$$

Where M_{r_T} is the mass of the target region, E_i is the mean emitted energy for emission i, Y_i is the corresponding yield, and ϕ_i is the so-called *absorbed fraction*, which describes the fraction of energy emitted from r_S that is deposited in r_T.

The absorbed dose can be divided into two categories: *self-dose* ($r_T \leftarrow r_T$) and *cross-dose* ($r_T \leftarrow r_S$). For *self-dose*, we consider the dose contribution from activity in the target region itself. Conversely, *cross-dose* involves dose contributions from neighboring regions, see Figure 2.12.

In therapeutic applications, we are often most concerned with particle self-dose. At the macroscopic level—e.g., for an entire organ—one can often assume that all charged particles will completely deposit their energy within that same region, i.e., $\phi_i = 1$. Exceptions occur when the particle range is comparable to the considered region, e.g., in instances of high particle energy or for very small tissue structures (e.g., red marrow within a vertebrae).

2.6.3 Time-Activity Curve Fitting

As previously discussed, the TIA is defined as the total number of decays within the source region over a given period of time. While post-therapeutic imaging allows for estimates of the activity distribution within the patient at selected time points after administration, computing the TIA requires—as evident in Eq. (2.8)—an expression for the activity as a function of time, i.e., a *time-activity curve* (TAC).

To illustrate the most fundamental concepts, let us consider the simplest form of a TAC, i.e., a monoexponential function:

$$A(t) = A_0 \cdot e^{\lambda_{eff} \cdot t} \qquad \text{Eq. (2.10)}$$

Here, A_0 is the assumed activity at time $t = 0$, t is the time elapsed, and λ_{eff} is the effective elimination coefficient (defined as $\lambda_{eff} = \lambda_{bio} + \lambda_{phys}$), which relates to the *effective half-life* as $T_{eff} = \ln(2)/\lambda_{eff}$. Effective half-life is an important quantity in internal dosimetry, describing the combined elimination of the radiopharmaceutical due to both biological excretion (λ_{bio}) and physical decay (λ_{phys}).

While monoexponential models are commonly used, they provide a simplified representation of the biokinetics, as they do not account for the uptake phase (i.e., $A_0 \neq 0$). For a more accurate description, multi-exponential functions—e.g., sums of exponentials—can be employed.

In applications where even greater physiological detail is sought after, compartmental models or physiologically based pharmacokinetic models may be used (*119*). These models describe the biokinetic profile using interconnected compartments representing different organs or tissues and can provide a more detailed description of the uptake, distribution, redistribution, and excretion of a radiopharmaceutical.

2.6.3.1 Pitfalls in TAC Fitting

At first glance, generating a TAC might seem straightforward; all you need is a bit of time-activity data and a curve-fitting software, and you're all set. Unfortunately, it's not that simple. The curve-fitting process involves several pitfalls that one needs to be mindful of, and the chosen fit may significantly impact the accuracy of the absorbed dose estimation.

One major limitation is the number of data points available. Generally, the more imaging time points, the better. A common rule of thumb is that at least three sampling points should be used per exponential, to avoid overfitting (*120*). This is, however, easier said than done—imaging can be both resource-intensive (in terms of available personnel and camera slots) and physically demanding for patients. Commonly, no more than four imaging sessions are performed, making multiexponential fitting (while more biologically accurate than monoexponential fitting) unsuitable.

One potential workaround is incorporating *a priori* information, such as population-based biological half-life estimates, which allows for reasonable fitting with fewer data points. Current research places significant focus on simplified dosimetry protocols that rely on fewer, or even a single, time point (*121*–*126*).

Another critical factor to consider is the temporal sampling (i.e., the time points at which imaging is performed), as this too can have a major impact on the resulting fit. There is no universal optimal schedule—it depends on the pharmacokinetics of the drug and the specific tissue examined. For biexponential fitting, an ideal scheme has been proposed as effective half-life × 0.1, 0.3, 1, 3, and 5 (*120*). Including a late time point (e.g., ≳ 1 week) has been proven especially important for obtaining good accuracy (*127*).

To this day, best practices of TAC fitting remain a subject of debate, and official guidelines are lacking. Recently, Ivanshenko et al. (2023) proposed a quality control workflow for TAC fitting, including seven recommended control measures (ranging from low- to high-level) for evaluating the goodness of a fit (*120*). Table 2.5 shows my interpretation of Ivanshenko's suggested workflow.

TABLE 2.5. Seven quality control measures proposed by Ivanshenko et al. to evaluate the adequacy of a TAC (*120*).

	Assess the…	The ♥ of the question	What to do
Low-level	Appearance	Does the fit look reasonable?	Inspect visually
	Plausibility	Do the fitted parameters assume realistic values?	Control parameters that correspond to physical quantities, e.g., half-life > 0
	Coefficient of determination	Does the model provide a good approximation for the given data points?	Check the R^2-value. The closer to 1, the better.
Mid-level	Correlation of fitted parameters	Do the fitting parameters uniquely contribute to output of the model?	Inspect the correlation matrix. Off-diagonal elements should fall within [-0.8, 0.8].
	Uncertainty of fitted parameters	Can we trust the fitted parameters, or might other values fit the data just as well?	Evaluate the coefficient of variation (CV). Should be < 50%.
	Distribution of weighted residuals	Are there any systematic over- or underestimations of activity?	Ensure that the weighted residuals are uniformly dispersed around zero
High-level	TIA uncertainty	What uncertainty could the model introduce in terms of dose?	Calculate the uncertainty of the TIA through error propagation

2.7 RADIOLIGAND OPTIMIZATION STRATEGIES

There are numerous ways in which radionuclide therapies can be optimized to achieve better therapeutic outcomes. Naturally, the choice of radionuclide plays a major role. Other optimization strategies include modifying the administration protocol, e.g., by adjusting the number of treatment cycles, the activity per cycle, or the time between cycles. The field of radiobiology focuses on the use of radiosensitizers to enhance tumor response, and radioprotectors to reduce toxicity in organs at risk.

Ultimately, all optimization strategies share a common goal: expanding the *therapeutic window*—that is, enhancing treatment efficacy while maintaining an acceptable safety profile. Another approach—explored herein—is to optimize the design of the radioligand to improve the drug's pharmacokinetic profile, the goal being to maximize the absorbed dose to the tumor while keeping the absorbed dose to organs at risk low (i.e., improved tumor-to-organ-at-risk absorbed dose ratios). In this thesis, two specific radioligand optimization strategies are explored, which are discussed in more detail below.

2.7.1 Somatostatin Antagonists for Therapy of NETs

Somatostatin receptors (SSTRs) have proven to be a highly successful target for the treatment of neuroendocrine tumors (NETs). Currently established ligands (e.g., DOTATATE and DOTATOC) are SSTR agonists that bind to the receptor and undergo internalization into the tumor cell. More recently, SSTR antagonists have emerged as a promising alternative. Unlike agonists, antagonists bind to and block the receptor without internalization, and exhibit significantly higher uptake due to the availability of more SSTR binding sites (*128*).

Clinical studies have demonstrated that SSTR antagonists, e.g., DOTA-LM3 and DOTA-JR11, can be used to achieve high tumor doses and possibly favorable treatment outcomes (*129*, *130*). The administration of ~6 GBq [^{177}Lu]Lu-DOTA-LM3 showed good therapeutic efficacy with no significant toxicity across 51 patients, and a favorable therapeutic index compared to [^{177}Lu]Lu-DOTATOC: a 5.1-fold higher tumor absorbed dose with only a 3.8-fold higher kidney absorbed dose (*129*).

However, the increased uptake induced by antagonists is also associated with a higher risk of toxicity—particularly for radiosensitive tissues, such as the bone marrow. There are some cautionary cases; in a phase I study with [^{177}Lu]Lu-DOTA-JR11, two treatment cycles of ~7 GBq resulted in grade 4 hematological toxicity in four out of seven patients. The study was suspended, and continued with decreased activity (*131*).

Nevertheless, recent data suggest that there is a synergistic effect to combining antagonists (specifically DOTA-LM3) with ^{161}Tb (*132*,*133*). *In vitro* studies demonstrated that [^{161}Tb]Tb-DOTA-LM3 was 820 and 102 times more potent in reducing cell viability compared to [^{177}Lu]Lu-DOTATOC and [^{177}Lu]Lu-DOTA-LM3, respectively. Additionally, [^{161}Tb]Tb-DOTA-LM3 resulted in superior tumor growth delay and prolonged survival in mice, with no observed toxicity (*132*). These effects were attributed to increased cell membrane damage, caused by the low-energy electron contributions (*132*,*133*).

Overall, these findings highlight [^{161}Tb]Tb-DOTA-LM3 as a promising candidate for NET treatment, potentially combining the benefits of both ^{161}Tb and SSTR antagonists. However, further investigations are needed to assess possible toxicity and confirm potential benefits.

2.7.2 Albumin-Binding Ligands for Therapy of mCRPC

Targeting prostate-specific membrane antigen (PSMA) has been demonstrated to be a viable strategy for radionuclide therapy of metastatic castration-resistant prostate cancer (mCRPC). However, first-generation PSMA ligands (e.g., PSMA-617 and PSMA-I&T) have shown limited efficacy, with approximately one-third of PSMA-positive mCRPC patients not responding to treatment (*134*). One possible limitation is the rapid clearance of these ligands from the bloodstream, which may restrict tumor uptake.

To address this, focus has been placed on developing albumin-binding PSMA ligands, designed to extend circulation time and enhance tumor accumulation (*135*). Serum albumin—the most abundant protein in blood—plays a crucial role in maintaining colloid osmotic pressure and transporting various substances, e.g., hormones and fatty acids. Incorporating albumin-binding properties is an established way to prolong the circulation of a drug (*136*).

Initial clinical studies with the albumin-binding ligand [^{177}Lu]Lu-PSMA-ALB-56 (a single cycle of 3 GBq in 10 patients) demonstrated increased tumor uptake and an improved tumor-to-salivary gland dose ratio compared to [^{177}Lu]Lu-PSMA-617. However, these benefits came at the cost of high absorbed doses to the bone marrow and kidneys (*137*), highlighting the challenge of optimizing albumin affinity to minimize toxicity.

More recently, ibuprofen has been explored as an albumin-binding entity for PSMA ligand optimization (*138*). Compared to other albumin-binding ligands (e.g., ALB-56), ibuprofen-based ligands exhibit slightly lower albumin affinity, potentially leading to more favorable pharmacokinetics (*139*). Specifically, the radioligand [^{177}Lu]Lu-SibuDAB has shown promising properties in preclinical studies, outperforming [^{177}Lu]Lu-PSMA-617 in terms of increased survival in mice (*140*). Recently, [^{177}Lu]Lu-SibuDAB was evaluated in a first-in-human study (17 patients, injected with ~5 GBq in a single cycle), where SPECT-based dosimetry revealed a two-fold higher tumor absorbed dose. This said, tumor-to-kidney and tumor-to-bone marrow dose ratios that were comparable to those of conventional ligands (*141*).

It has been suggested that combining ^{161}Tb with albumin-binding ligands could effectively expand the therapeutic window in mCRPC radionuclide therapy (*142*, *143*). The use of ^{161}Tb is described as particularly favorable for mCRPC, as the condition is characterized by widespread micrometastases (*142*). Preclinical comparisons of SibuDAB and PSMA-I&T labeled with ^{161}Tb and ^{177}Lu, respectively, have been conducted, showing that [^{161}Tb]Tb-SibuDAB was the most effective at inhibiting tumor growth (*143*). However, clinical studies are still needed to confirm whether these therapeutic benefits can be realized, or if the prolonged circulation and higher absorbed doses may induce toxicity.

3 SPECIFIC AIMS

In this section, I provide a condensed background to each project, along with the specific study aims.

Paper I: While ^{161}Tb-based SPECT imaging has been proven viable, quantitative assessments are lacking. The aim of this study was to assess the feasibility of accurate SPECT/CT-based ^{161}Tb activity quantification using clinical reconstruction software, with particular focus on collimator choice (e.g., low- or medium-energy) and energy window selection.

Paper II: The ^{161}Tb decay scheme is characterized by intense X-ray emissions, along with numerous low-yield, high-energy γ-photons, which may degrade image quality. This study aimed to characterize the performance of a SPECT/CT system employed in clinical ^{161}Tb imaging (Papers III and IV), focusing on sensitivity, septal penetration, and dead-time effects.

Paper III: Studies have shown that somatostatin receptor antagonists, e.g., DOTA-LM3, exhibit higher tumor uptake compared to analogues like DOTATOC, leading to favorable tumor-to-risk organ dose ratios. The aim of this study was to compare the absorbed doses for [^{161}Tb]Tb-DOTA-LM3 and [^{177}Lu]Lu-DOTATOC in patients with NETs.

Paper IV: Incorporating albumin-binding properties into PSMA ligands has been suggested as a strategy to improve treatment outcomes. The aim of this study was to compare the absorbed doses of [^{161}Tb]Tb-SibuDAB (a weak albumin-binding ligand) and [^{177}Lu]Lu-PSMA-I&T (a standard PSMA ligand) in patients with mCRPC.

4 PATIENTS AND METHODS

The following text is structured thematically to reflect the common methodology across Papers I–IV. All patient-related procedures were conducted in accordance with the principles of the Declaration of Helsinki. Ethical approval was granted by the Ethics Committee of Northwest and Central Switzerland (Paper III: 01.03.2022; No. 2022-00162; Paper IV: 06.11.2023; No. 2023-01868). Informed consent was obtained from patients prior to inclusion in each study. Patients provided written consent for the anonymous use of clinical data and image data for publication.

4.1 IMAGE ACQUISITION PROTOCOLS

4.1.1 Sahlgrenska University Hospital

For the technical evaluations in Paper I, all imaging was performed at Sahlgrenska University Hospital using a GE Discovery NM/CT 670 Pro system. A 360° step-and-shoot acquisition with body contouring was employed, using 120 projections, a 256 × 256 matrix, and a clinical low-dose CT protocol. The SPECT energy protocol included two photopeak windows around the 49 and 75 keV peaks, respectively, along with three adjacent scatter windows (Figure 4.2A), as previously established by Marin et al. (29).

Three different collimators were evaluated: extended low-energy general purpose (ELEGP), low-energy high-resolution (LEHR), and medium-energy general purpose (MEGP), see Figure 4.1.

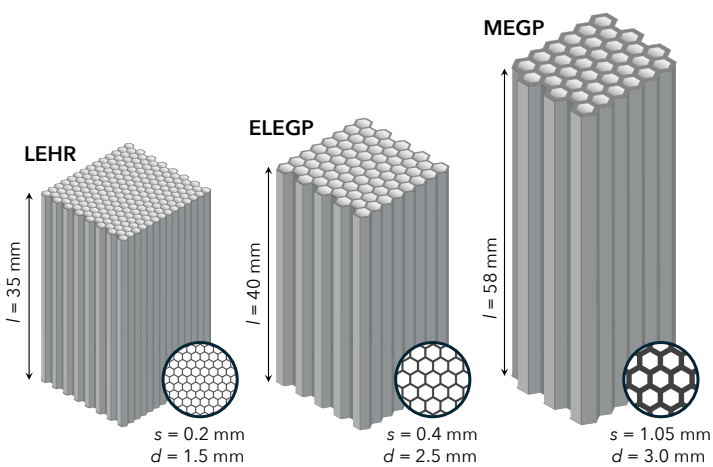

FIGURE 4.1. The collimators evaluated in Paper I. Hole lengths (*l*), hole diameters (*d*), and septal thicknesses (*s*) are sketched to reflect the true proportions of each design, as specified by the vendor (144).

4.1.2 Basel University Hospital

Leading up to the clinical trials at Basel University Hospital, a dedicated ^{161}Tb SPECT/CT protocol was established on the hospital's Siemens Symbia Intevo 16 system, which was used in Papers II–IV. The protocol included a step-and-shoot acquisition with body contouring, 60 projections, and a 256 × 256 matrix (2.40 × 2.40 mm pixels). A clinical low-dose CT protocol was employed. Imaging time points, bed position configurations, and acquisition durations are detailed in the study protocol descriptions in Section 4.2.

For clinical imaging, a low-energy high-resolution (LEHR) collimator was used; however, additional calibration and evaluations were performed using a medium-energy low-penetration (MELP) collimator, see collimator dimensions in Table 4.1.

TABLE 4.1. Collimator dimension specification for the Siemens Symbia Intevo system.

Collimator	Hole length (mm)	Hole diameter (mm)	Septal thickness (mm)
MELP	40.64	2.94	1.14
LEHR	24.05	1.11	0.16

The SPECT energy protocol was modified, as compared to in Paper I: two photopeak windows (48 keV ± 20% and 75 keV ± 10%), along with two adjacent scatter windows per photopeak; see Table 4.2 and Figure 4.2B.

TABLE 4.2. The Siemens ^{161}Tb energy protocol, listed using standard Siemens nomenclature. Each window is defined by its center energy (keV), width (%), and, where applicable, shift (%). Photopeak windows (A1, B2) serve as parent windows for the corresponding lower and upper scatter windows (C3–F6).

Window	Center (keV)	Width (%)	Shift (%)	Type	Parent
A1	48	40	0	Photopeak	
B2	75	20	0	Photopeak	
C3		10		Lower Scatter	A1
D4		10		Upper Scatter	A1
E5		6		Lower Scatter	B2
F6		6		Upper Scatter	B2

TABLE 4.3. The Siemens ^{177}Lu energy protocol, with the same notations as in Table 4.1.

Window	Center (keV)	Width (%)	Shift (%)	Type	Parent
A1	208	20	0	Photopeak	
B2		10	0	Lower Scatter	A1
C3		10	0	Upper Scatter	A1

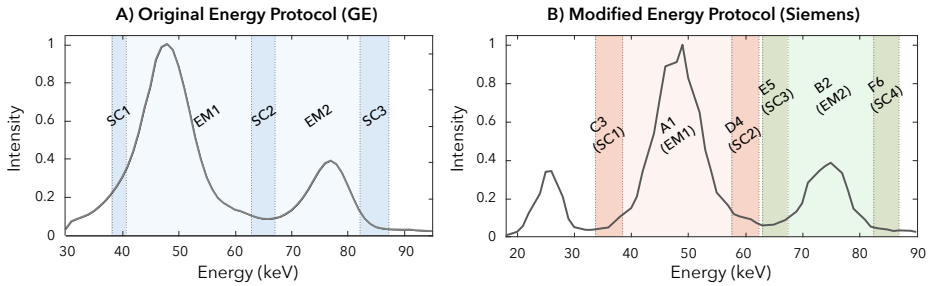

FIGURE 4.2. Employed ^{161}Tb energy window settings overlaid on energy spectra acquired in air for the GE (A) and Siemens (B). In (A), GE nomenclature is used (scatter windows: SC1–SC3; photopeak windows: EM1–EM2), while (B) shows Siemens settings (as in Table 4.1), with GE equivalents in parentheses.

As the clinical trials involved intrapatient comparisons with ^{177}Lu-labelled ligands, protocols were also established for this nuclide, employing identical acquisition parameters except for a 208 keV ± 10% photopeak window and two adjacent scatter windows (see Table 4.3) and a MELP collimator.

4.2 CLINICAL STUDY PROTOCOLS

4.2.1 BETA PLUS for NETs

The BETA PLUS study is a randomized, cross-over, prospective, single-center, open-label phase 0 trial designed to compare absorbed doses for [^{161}Tb]Tb-DOTA-LM3 and [^{177}Lu]Lu-DOTATOC in patients with gastroenteropancreatic neuroendocrine tumors (GEP-NETs). The study was initiated in March 2023, and is expected to be completed by December 2025, with an estimated inclusion of 16 patients (8 in phase 0a and 4–8 in phase 0b).

The now-completed phase 0a study (pertaining to Paper III) included two test injections per patient: 1 GBq [^{161}Tb]Tb-DOTA-LM3 (≤ 100 µg peptide) and 1 GBq [^{177}Lu]Lu-DOTATOC (~200 µg peptide), administered 4–6 weeks apart. Patients were randomized into two groups: one group received [^{161}Tb]Tb-DOTA-LM3 first, followed by [^{177}Lu]Lu-DOTATOC, and the other group received the injections in reverse order. Kidney protection was administered with both injections.

Post-therapeutic SPECT/CT imaging was performed at 3, 24, 72, and 168 hours post-injection. Two bed positions and an acquisition time of 30 s per projection were used. The first bed position comprised the region from the shoulders to the mid-abdomen, while the second covered mid-abdomen to the bottom of the pelvis.

4.2.1.1 Subsequent Study Phase

Phase 0b, currently ongoing, will include comparative dosimetry for two ~1 GBq test injections of [^{161}Tb]Tb-DOTA-LM3 administered with different peptide amounts (≤ 100 µg and ~300 µg) to the same patients. If well tolerated, patients will proceed to two therapeutic cycles of [^{161}Tb]Tb-DOTA-LM3 with increased activity, administered approximately eight weeks apart. The preferred peptide amount is decided based on the dosimetry of the two test injections.

4.2.2 PROGNOSTICS for mCRPC

The PROGNOSTICS study is a prospective, single-center, phase 1 trial evaluating the safety and efficacy of [^{161}Tb]Tb-SibuDAB in relation the established [^{177}Lu]Lu-PSMA-I&T. The trial was initiated in January 2024 and is expected to be completed by December 2027. The study consists of two phases: phase 1a, a randomized, open-label, cross-over study including 10 patients, and phase 1b, a dose-escalation study with an estimated inclusion of 15 patients.

Phase 1a (relating to Paper IV), which is now completed, included two test injections per patient: 1 GBq [^{161}Tb]Tb-SibuDAB (~200 µg of peptide) and 1 GBq [^{177}Lu]Lu-PSMA-I&T (~100 µg peptide), administered 2 weeks apart. Similarly to in the BETA PLUS study, patients were randomized into two groups: one receiving [^{161}Tb]Tb-SibuDAB as the first injection and [^{177}Lu]Lu-PSMA-I&T as the second injection, and the other in reversed order.

Post-therapeutic SPECT/CT imaging was performed at 3, 24, 48, and 168 hours post-injection. For this study, the acquisition time was reduced to 25 s per projection to accommodate three adjacent bed positions: the first including the head, neck, and shoulders (to enable salivary gland dosimetry); the second over the abdomen; and the third over the pelvis and upper thighbone.

4.2.2.1 Subsequent Study Phase

Phase 1b is a dose-escalation study including up to 15 patients receiving 4 injections of [^{161}Tb]Tb-SibuDAB, administered every 6 weeks. A 3+3 dose-escalation design will be applied. Administered activities will be adjusted if the maximum absorbed dose constraints—30 Gy to the kidneys and 2 Gy to the bone marrow—are at risk of being exceeded, or if clinical signs of toxicity emerge.

4.3 ACTIVITY MEASUREMENTS

For all studies, ^{161}Tb was produced at the Paul Scherrer Institute (PSI) in Switzerland, and the activity was determined using equipment calibrated with standards traceable to the Système International de Référence (*145*). For Paper I, the dose calibrator at Sahlgrenska University Hospital was calibrated against a ^{161}Tb reference vial provided by PSI. Similarly, the dose calibrators used at Basel University Hospital (Papers II–IV) were cross-calibrated against PSI standards. For the SPECT calibration in Papers III and IV, additional cross-calibration was performed by sending aliquots from the phantoms to PSI for activity determination using a HPGe detector.

4.4 PHANTOM MEASUREMENTS

4.4.1 Uniformity

In Paper I, SPECT image uniformity was assessed prior to all phantom experiments. Uniformity maps were acquired intrinsically using ^{161}Tb point sources of varying activity (one map per detector and photopeak window), and extrinsically using a ^{161}Tb flood source phantom (one map per detector and collimator–photopeak window combination), as shown in Figure 4.3. The resulting maps were compared with clinically available intrinsic ^{99m}Tc-based maps, using measurements of a uniform cylinder phantom. Based on these comparisons, extrinsic maps were found most suitable and were applied in all subsequent measurements.

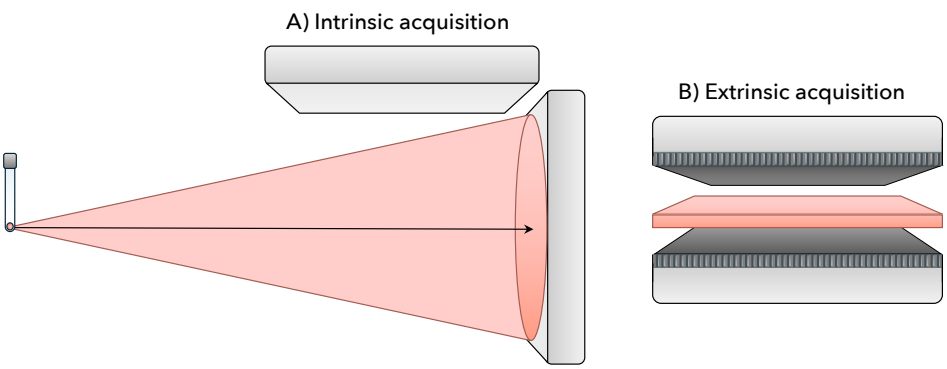

FIGURE 4.3. Setups for acquiring uniformity maps: (A) intrinsically, using a distant point source and the detectors in L-mode, and (B) extrinsically, using a flood phantom and the detectors in H-mode.

For the Siemens system employed in Papers II–IV, clinically available intrinsic uniformity maps were deemed suitable (once again supported by measurements of a cylindrical phantom) and were therefore applied without additional calibration.

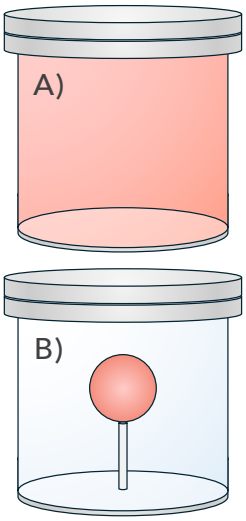

FIGURE 4.4. CF phantom geometries: (A) a uniform cylinder phantom, (B) a large sphere in water.

4.4.2 Calibration Factors

In Paper I, SPECT calibration factors (CFs) were established using two separate phantom configurations (Figure 4.4): a cylinder with uniform activity (uniCF) and a cylinder containing a single hot sphere (V = 113 mL) in water (sphCF). CFs were calculated as:

$$CF = \frac{\dot{C}}{A_{Ref}} \qquad \text{Eq. (4.1)}$$

Where $\dot{C}$ represents the recorded count rate within a specified volume-of-interest (VOI), and A_{Ref} denotes the corresponding VOI activity derived from dose calibrator measurements. Various VOI sizes were analyzed to evaluate robustness.

For the clinical dosimetry (Papers III and IV), the CFs for ^{161}Tb and ^{177}Lu were established using the uniCF geometry with a cylinder VOI comprising roughly 50% of the total phantom volume.

4.4.3 Recovery

In Paper I, recovery coefficients (RCs) were determined using a cylindrical Jaszczak phantom containing six spherical inserts (V = 0.5, 1, 2, 4, 8, and 16 mL) in a cold background (Figure 4.5). RCs were calculated as:

$$RC = \frac{\dot{C} \times \frac{1}{CF}}{A_{Ref}} \qquad \text{Eq. (4.2)}$$

To evaluate the SPECT reconstructions in Papers III and IV, a similar methodology was applied. RCs were determined as a function of the number of OSEM updates using a NEMA Body Phantom with spherical inserts (V = 0.5, 1.2, 2.6, 5.6, 11.5, and 26.5 mL). Measurements were performed both with a cold background and at a sphere-to-background ratio (SBR) of 10.

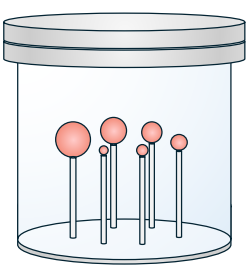

FIGURE 4.5. Phantom with spherical inserts, as used to determine RCs.

4.4.4 Anthropomorphic Evaluations

In Paper I, an Elliptical Lung-Spine Phantom was used to assess quantitative errors in a patient-like geometry (Figure 4.6A). Eight spheres filled with ^{161}Tb (2, 4, 8, and 16 mL; each × 2) were placed in various locations within the phantom. Measurements were performed using SBRs of ∞, 20:1, and 10:1. Duplicate ELEGP measurements were acquired to assess noise sensitivity. Quantitative accuracy was evaluated using the relative quantification error (RQE), defined as follows:

$$RQE = \frac{A - A_{Ref}}{A_{Ref}} = \frac{\dot{C} \times \frac{1}{CF} \times \frac{1}{RC}}{A_{Ref}} - 1 \qquad \text{Eq. (4.3)}$$

Additionally, Paper I included measurements using two 3D-printed kidney inserts placed in a NEMA Body Phantom (Figure 4.6B). RCs were determined as described in Eq. (4.2), and line profiles were extracted across the kidneys to evaluate spatial resolution and contrast.

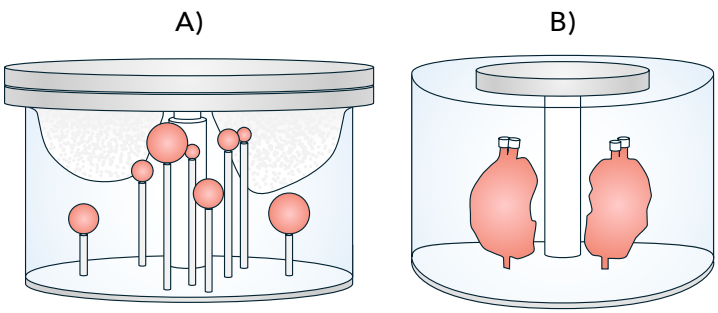

FIGURE 4.6. Anthropomorphic phantom setups: (A) the Elliptical Lung-Spine phantom with spherical inserts, lung inserts filled with Styrofoam beads and water, and a spinal insert; (B) the NEMA Body Phantom with 3D-printed kidney inserts and a spinal insert.

For the clinical implementations in Papers III and IV, the Lung-Spine Phantom (Figure 4.6A) was used to estimate quantification errors relevant to tumor dosimetry. The same SBRs as in Paper I (∞, 20:1, and 10:1) were applied, but with sphere volumes of 0.5, 1, 2, 4, 8, and 16 mL. The proposed patient quantification method (Section 4.6.1) was employed, and resulting errors were assessed.

4.4.5 Sensitivity, Penetration, and Dead Time

In Paper II, a characterization of the Siemens system at Basel University Hospital was performed using the phantom geometries shown in Figure 4.7. Planar acquisitions were performed at various source-to-collimator distances using a Petri dish filled with ^{161}Tb. Planar sensitivity and septal penetration were evaluated according to NEMA standards (*146*).

Dead time was assessed intrinsically using a set of ^{161}Tb point sources. The observed wide-spectrum count rate (R_O) was recorded, and the true count rate (R_T) was estimated by linear extrapolation of R_O in the low-count-rate region. Sorensen's paralyzable model was fitted to the data to extract the dead-time constant (τ), and fractional dead-time losses (ω) were determined.

To investigate potential dead-time losses in clinical SPECT imaging, a cylindrical phantom was imaged with the MELP and LEHR collimators, employing both open energy window settings and the ^{161}Tb energy protocol (see Section 4.1.2). Angular sensitivity, $S(\theta)$, was defined as the count rate per unit activity for each projection. Critical activity levels (A_{Crit}), corresponding to predefined dead-time loss thresholds, were estimated based on $S(\theta)$ and the intrinsic dead-time data.

Finally, patient count rates recorded in the BETA PLUS trial (Paper III) were analyzed to assess the potential impact of dead time under clinical conditions.

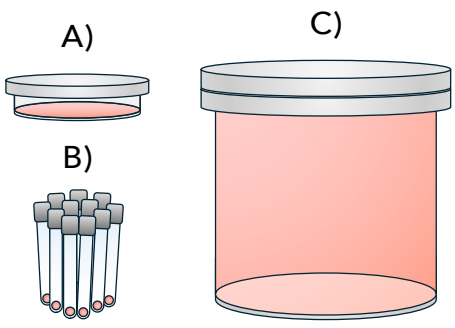

FIGURE 4.7. Measurement geometries for characterization: (A) a Petri dish for sensitivity and penetration determination, (B) point sources for dead-time estimation, and (C) a homogeneous cylinder phantom for SPECT dead-time evaluation.

4.5 SPECT RECONSTRUCTIONS

4.5.1 Conventional OSEM Reconstruction

In Paper I, all images were reconstructed using the vendor-provided OSEM algorithm (Volumetrix MI, Xeleris 4.0, GE) using 2–20 iterations and 10 subsets, along with a CT-based attenuation correction, a TEW scatter correction, and resolution recovery.

4.5.2 MC-Based OSEM Reconstruction

For Papers III and IV, reconstructions were performed using our in-house MC-based OSEM reconstruction (*89*). To reduce computation time, projection data were down-sampled from 256 × 256 to 128 × 128. Different iteration and subset configurations were evaluated. Ultimately, 6 iterations and 10 subsets were chosen. For the ^{161}Tb dosimetry in Papers III and IV, only the 75 keV ± 10% photopeak window was used.

ARFs were simulated for both LEHR and MELP collimators based on vendor-provided specifications, see Table 4.1. For both ^{161}Tb and ^{177}Lu, energy resolution was determined using a recently published model (*147*) and validated against measured energy spectra. The appropriate number of scatter orders was evaluated.

The MC simulation was incorporated in the forward-projection step, providing compensation for attenuation, in-patient scatter, and CDR degradation. The back-projection included a convolution-based CDR compensation using a MC-simulated PSF. The simulation parameters used are summarized in Table 4.4 for ^{161}Tb and ^{177}Lu, respectively.

TABLE 4.4. Summary of simulation parameters applied in the MC-based reconstructions for ^{177}Lu and ^{161}Tb.

Parameter	^{177}Lu	^{161}Tb
Photon energy	208 keV	74.6 keV
Yield	10.4%	10.2%
Energy window	187.2–228.8 keV	67.14–82.06 keV
Maximum angle	0.06 rad	0.06 rad
Crystal thickness	9.525 mm	9.525 mm
Photon histories	400 per voxel	400 per voxel
Scattering order	3	3
Energy resolution	9.0%	12.5%
ARF	Siemens MELP	Siemens LEHR

As multiple bed positions were employed (two in Paper III and three in Paper IV), each FOV was reconstructed separately and subsequently merged. To ensure smooth transitions, the values of overlapping voxels v were determined as:

$$v(x,y) = v_1(x,y)_i \cdot \frac{n-i}{n+1} + v_2(x,y)_i \cdot \frac{i}{n+1}, \qquad \text{for } i = 1, 2, \ldots, n \qquad \text{Eq. (4.4)}$$

Where v_1 and v_2 are the voxel values in overlapping slices (indexed by i) in the first and second FOV, respectively, and n is the number of overlapping slices. The voxel overlap was set to $n = 4$.

4.6 CLINICAL DOSIMETRY

4.6.1 Segmentation and Activity Quantification

For the clinical dosimetry in Papers III and IV, VOIs were delineated using a combination of manual, semi-automatic, and automatic methods, depending on the tissue of interest.

Kidney activity concentrations were determined using a small-VOI approach, with a single 30 mL VOI placed centrally in the kidney parenchyma, to mitigate PVEs. The 30 mL VOIs were generated using an isosurface-based segmentation tool, which was applied to 3D Gaussian-filtered SPECT images (σ = 16 mm). A seed region was manually defined in the filtered images, and an isovalue corresponding to the predetermined volume was selected to delineate the boundary. VOIs were then applied to the unfiltered images to extract the activity concentration. The method was validated via MC simulation for both ^{161}Tb and ^{177}Lu.

A similar methodology was used to determine spleen activity concentrations (Paper IV only), with isosurface VOIs placed centrally in the spleen with a ~1 cm margin from the outer edge to minimize spill-out.

Tumor volumes were determined based on pre-therapeutic diagnostic imaging (either ^{68}Ga PET/CT, contrast-enhanced CT, or MRI), with an inclusion criterion of $V > 1$ mL. Tumor volume was assumed to be constant for both the ^{161}Tb and ^{177}Lu test injections.

Tumor activity was quantified using extended VOIs encompassing all visible uptake. For tumors clearly separated from background or adjacent organs, the isosurface tool was used. In cases of overlapping uptake or high background, manual segmentation was applied. Background correction was performed by placing a VOI in an adjacent tissue region deemed representative of non-tumor activity. For each lesion, the VOI

size was kept constant across all time points. Tumor activity was calculated by subtracting the background contribution from the total VOI count.

Bone marrow dosimetry (Paper III only) was based on activity concentrations measured in the L1–L5 vertebral bodies, initially segmented manually using low-dose CT. An AI-based segmentation model was subsequently developed and applied. Vertebrae with metastases, or located near metastatic lesions, were omitted. The mean activity concentration across eligible vertebrae was used for absorbed dose calculations. For Paper IV, blood-based bone marrow dosimetry was performed.

Various segmentation methods were evaluated for salivary gland dosimetry (Paper IV only), including a small-VOI approach for determining activity concentration with minimal spill-out. Two VOI sizes were tested: 2 mL and 4 mL. While no significant difference in the resulting mean activity concentration was observed, the 2 mL estimates were deemed unacceptably noisy. Consequently, the 4 mL small-VOI approach was selected, with one centrally placed VOI in each parotid gland.

4.6.2 TAC Fitting and Absorbed Dose Calculations

All TACs were fitted using a nonlinear least-squares method in MATLAB, applying the following three-parameter biexponential function:

$$A(t) = a(e^{-bt} - e^{-ct}) \qquad \text{Eq. (4.5)}$$

Here, b corresponds to the effective decay constant, with effective half-life defined as $T_{eff} = \ln(2)/b$. As an exception, the [^{177}Lu]Lu-DOTATOC bone marrow dosimetry was based on a monoexponential fit, excluding the 3 h time point.

Absorbed doses were calculated according to the MIRD formalism (see Section 2.6.2). Photon contributions were neglected. S-values were derived based on the total mean emitted electron energy, $\Delta(^{161}\text{Tb}) = 202$ keV and $\Delta(^{177}\text{Lu}) = 148$ keV (*18*). An absorbed fraction of $\phi = 1$ was applied to all organs except bone marrow, for which $\phi(^{161}\text{Tb}) = 0.69$ and $\phi(^{177}\text{Lu}) = 0.65$ were used (*148*). A red marrow fraction of 0.63 was assumed (*149*,*150*). For all tissues, a soft-tissue density of $\rho = 1.05$ g/cm^3 was used. All absorbed dose estimates were normalized to the injected activity, and tumor-to-risk organ ratios were evaluated.

5 RESULTS

5.1 TECHNICAL FOUNDATIONS (PAPER I & II)

In Paper I, CFs were roughly 3-fold higher for the 49 keV window (Figure 5.1B) compared to the 75 keV window (Figure 5.1A). Moreover, the two CF geometries examined exhibited distinctly different behaviors. Generally, uniCFs (derived from the uniform cylinder phantom) remained stable across VOI volumes, with little dependency on the number of OSEM updates, whereas sphCFs (derived from the single 113 mL sphere in water) varied significantly (see Figure 5.1).

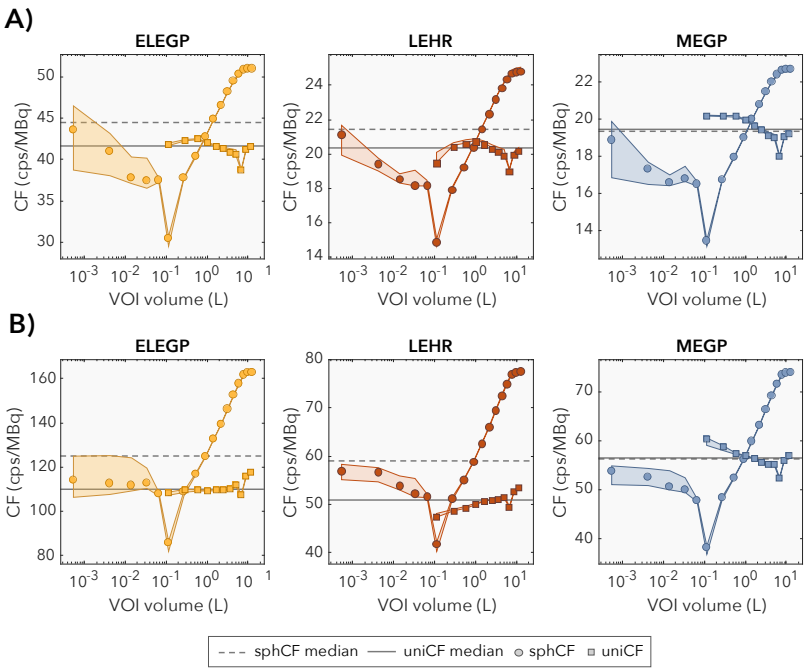

FIGURE 5.1. SPECT calibration factors (CFs) for the 75 keV (A) and 49 keV (B) windows, derived from phantom measurements using a uniform cylinder (uniCF, square markers) and a single large sphere (V = 113 mL) in water (sphCF, circle markers), for each respective collimator, displayed as a function of VOI volume. Shaded areas indicate variation due to the number of OSEM updates (minimum to maximum). Markers represent the mean across all iterations, and lines represent the median across all volumes.

For each collimator–window combination, the minimum sphCF was obtained for a VOI size corresponding to the physical volume of the insert (i.e., 113 mL). For VOIs exceeding this size, CFs increased steeply with volume—more so at 49 keV than at 75 keV—and reached maximum values when the VOI encompassed the entire phantom.

For VOIs smaller than the insert (V = 0.54–65.4 mL), CFs were closer to the uniCFs but showed a distinct dependency on the number of OSEM updates. Notably, the overall difference between uniCFs and sphCFs was reduced for the MEGP collimator (see lines in Figure 5.2).

As for visual image quality in Paper I, differences in resolution and contrast were apparent across the different settings. Figure 5.2 shows representative SPECT images of one of the 3D-printed kidneys for each collimator–energy window combination examined (top row). In general, the 49 keV window produced lower resolution and reduced contrast, compared to the 75 keV window. Among the collimators, LEHR provided the highest level of detail, followed by MEGP and then ELEGP, consistent with the spatial system resolution specifications provided by the manufacturer (*144*). The line profiles (Figure 5.2, bottom row) reflect these differences, showing broader activity distributions for lower-resolution combinations (e.g., ELEGP–49 keV) and narrower peaks for higher-resolution configurations (e.g., LEHR–75 keV).

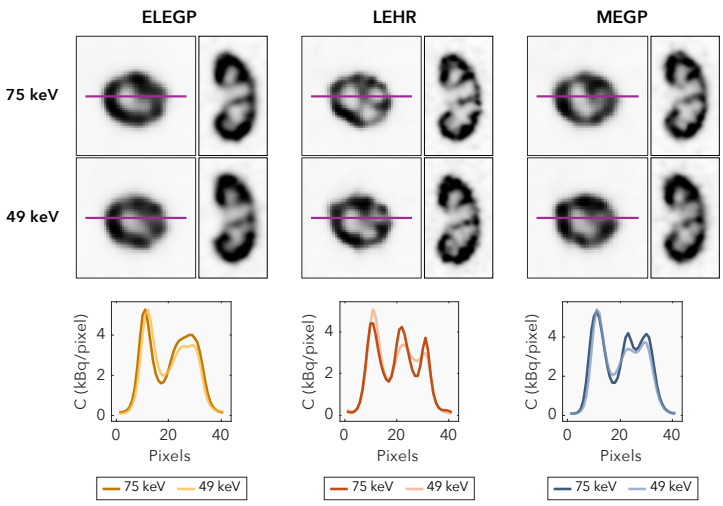

FIGURE 5.2. SPECT images (6i10s) of one of the 3D-printed kidneys (top row) along with extracted line profiles (bottom row), for each collimator–energy window combination as examined in Paper I.

For the Lung-Spine evaluation in Paper I, RQEs were similar across all collimator–energy window combinations when no background activity was used. When background activity was added, underestimations were observed for both low-energy collimators, becoming increasingly pronounced with higher background activity (i.e., at SBR = 10:1). At 75 keV, the maximum errors were –16% and –14% for ELEGP and LEHR, respectively. At 49 keV, the underestimation was more severe, reaching –37% for ELEGP and –43% for LEHR (see Figure 5.3).

In contrast, MEGP did not show this trend and exhibited low RQEs that were generally evenly distributed around zero. However, a consistent overestimation was observed for the 2 mL spheres, with a maximum of 23% at SBR = 20:1.

		75 keV			49 keV		
		Collimator			Collimator		
	Volume	ELEGP	LEHR	MEGP	ELEGP	LEHR	MEGP
No background	2 mL	8.8%	14%	16%	4.6%	3.8%	11%
		0.46%	4.0%	4.7%	4.1%	-2.5%	11%
	4 mL	2.9%	-1.8%	-2.3%	-3.2%	-5.9%	-7.7%
		-0.48%	3.5%	3.5%	2.1%	9.3%	5.4%
	8 mL	-2.9%	-5.5%	3.4%	-1.7%	-4.9%	-0.050%
		-4.0%	0.54%	0.00%	0.18%	0.80%	-0.54%
	16 mL	-3.4%	1.0%	-0.85%	-6.2%	-2.7%	-3.1%
		-2.7%	0.10%	1.9%	-1.7%	1.9%	3.1%
SBR = 20:1	2 mL	-4.3%	-0.38%	23%	-20%	-26%	6.7%
		-6.2%	-1.6%	10%	-20%	-14%	5.9%
	4 mL	-8.4%	-12%	-3.6%	-23%	-17%	-9.0%
		-0.18%	-3.1%	-1.8%	-12%	-7.5%	-4.5%
	8 mL	-8.2%	-10%	1.9%	-19%	-20%	-6.8%
		-10%	-5.0%	-1.1%	-16%	-15%	-4.8%
	16 mL	-10%	-7.8%	0.030%	-22%	-22%	-6.7%
		-7.1%	-3.2%	2.4%	-17%	-12%	-3.8%
SBR = 10:1	2 mL	-5.2%	-8.9%	16%	-37%	-43%	-1.2%
		-13%	-6.8%	20%	-22%	-25%	13%
	4 mL	-11%	-14%	-0.60%	-34%	-28%	-21%
		-1.7%	-4.7%	5.2%	-21%	-18%	-3.4%
	8 mL	-13%	-12%	-1.9%	-32%	-35%	-7.6%
		-15%	-13%	-0.15%	-27%	-26%	-9.2%
	16 mL	-16%	-14%	-2.1%	-32%	-33%	-13%
		-12%	-11%	3.7%	-25%	-26%	-8.0%
	Median	-5.7%	-4.9%	1.9%	-19%	-16%	-3.6%

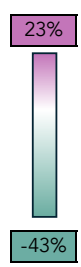

FIGURE 5.3. Relative quantification errors (RQEs) obtained using the Lung-Spine phantom for three activity conditions (no background, SBR = 20, SBR = 10) and sphere sizes (V = 2, 4, 8, 16 mL), as evaluated in Paper I at 20i10s (where RQEs were generally minimized). Results are shown for all examined collimator–window combinations, including the median error across all estimates.

Analysis of the acquired energy spectra in Paper I (see Figure 5.4C) revealed significantly elevated wide-spectrum count rates for LEHR and ELEGP, 123 and 106 cps/MBq respectively, compared to 48 cps/MBq for MEGP (Figure 5.4B). For LEHR, a majority of the recorded counts (60%) were situated above the highest scattering window, with a lower fraction for ELEGP (38%) and an even lower fraction for MEGP (26%).

For the Siemens system in Paper II, the fraction of penetration (PF) reached a maximum of 22% for LEHR–75 keV, whereas the other combinations (75 keV–MELP, 48 keV–LEHR, and 48 keV–MELP) produced PFs generally below 5% (Figure 5.5). Penetration was also observed as an increased wide-spectrum count rate—69 cps/MBq for LEHR (51% above the highest energy window), compared to 48 cps/MBq for MELP (12% above)—see Figures 5.4B and 5.4D.

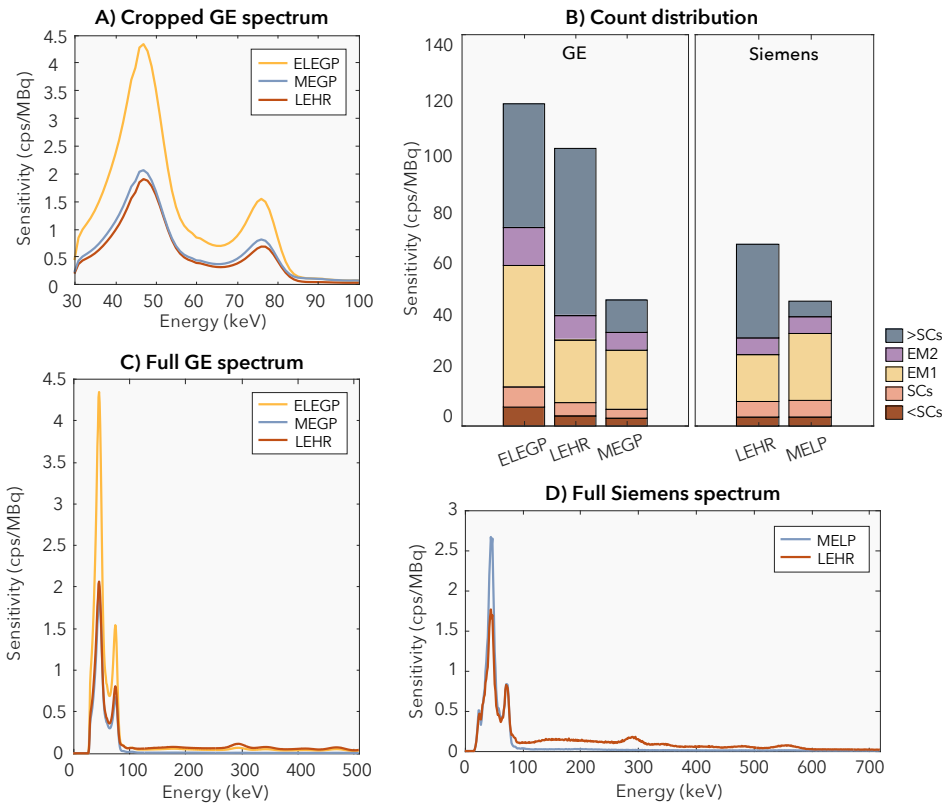

FIGURE 5.4. Energy spectra from cylinder phantom measurements for the GE system (Paper I, panels A and C) and the Siemens system (Paper II, panel D). Corresponding bar plots show the total counts recorded in different spectral regions for all examined collimators (GE: LEHR, ELEGP, MEGP; Siemens: LEHR, MELP). EM1 refers to the 48/49 keV photopeak window (depending on protocol, see Methods), EM2 to the 75 ± 10% keV window, and SC to the scatter windows.

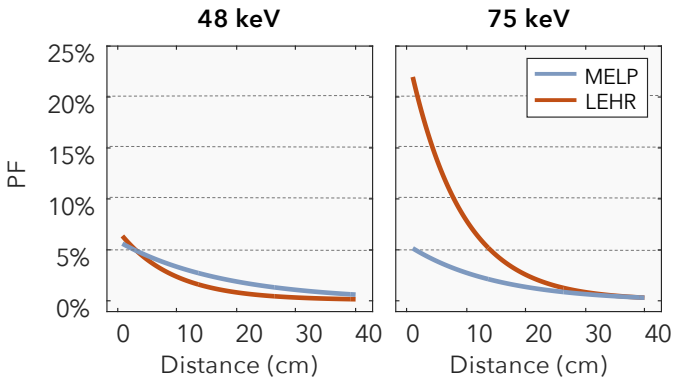

FIGURE 5.5. The penetration fraction (PF), determined according to the NEMA standard (146), as a function of source-to-collimator distance for the Siemens system (Paper II), measured for the LEHR and MELP collimators at 75 keV and 48 keV, respectively.

As for dead time, both detectors for the system in Paper II had an intrinsic dead-time constant of 0.42 µs. Non-linear responses were observed at count rates exceeding 93 kcps. With reference to the cylinder phantom, this corresponded to in-field activities as low as 1.4 GBq for LEHR and 1.7 GBq for MELP (assuming the minimal source-to-collimator distance). At very high count rates, saturation occurred, manifesting as a sudden sharp decline in recorded counts. This was observed at different thresholds for the two detector heads—384 kcps and 546 kcps, respectively.

Table 5.1 presents the predicted fractional dead-time losses at various in-field activity levels, with consistently higher values for LEHR, compared to MELP. For example, an in-field activity of 3 GBq was estimated to result in losses of 6.3%–8.9% for LEHR and 5.2%–6.5% for MELP (again, based on the cylinder phantom geometry).

TABLE 5.1. Predicted dead-time losses at various in-field activity levels for the Siemens system (Paper II), extrapolated from intrinsic count rate data, for MELP and LEHR, respectively.

	Dead-time loss	
Activity (GBq)	MELP	LEHR
1	1.8%–2.2%	2.2%–3.1%
2	3.5%–4.4%	4.3%–6.0%
3	5.2%–6.5%	6.3%–8.9%
4	6.9%–8.5%	8.4%–12%
5	8.5%–11%	10%–14%
6	10%–13%	12%–17%

5.2 CLINICAL APPLICATION (PAPER III & IV)

For the clinical imaging in Papers III and IV, distinct differences were observed between the examined agents in terms of both visual image quality and biokinetic properties (Figures 5.6 and 5.7).

In general, the ^{177}Lu images exhibited lower resolution, as expected with MELP collimation, while the ^{161}Tb images demonstrated higher resolution, consistent with the use of LEHR collimation. Both ^{161}Tb-labeled compounds showed high uptake and prolonged retention, which also contributed to reduced image noise.

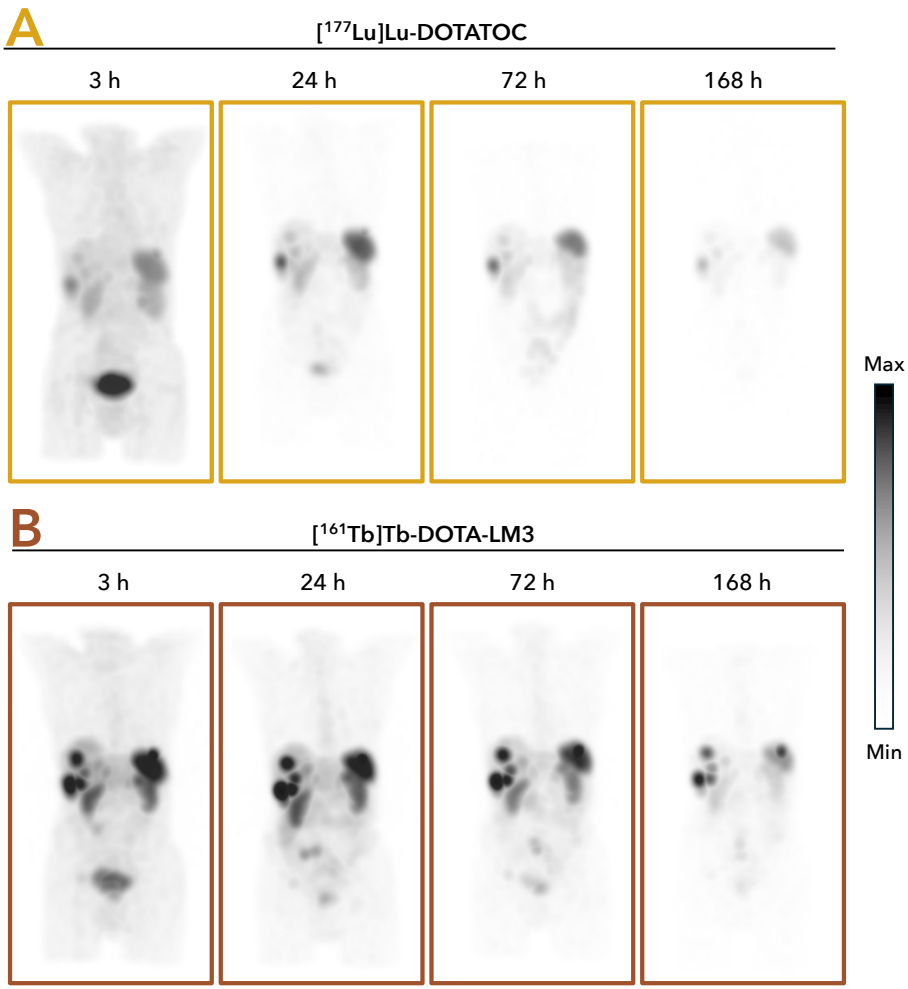

FIGURE 5.6. Maximum intensity projections from the MC-based SPECT reconstructions (6i10s) at 3 h, 24 h, 48 h, and 168 h post-injection for [^{177}Lu]Lu-DOTATOC (A) and [^{161}Tb]Tb-DOTA-LM3 (B). Equal gray scaling is applied to all images, with voxels values in unit of activity.

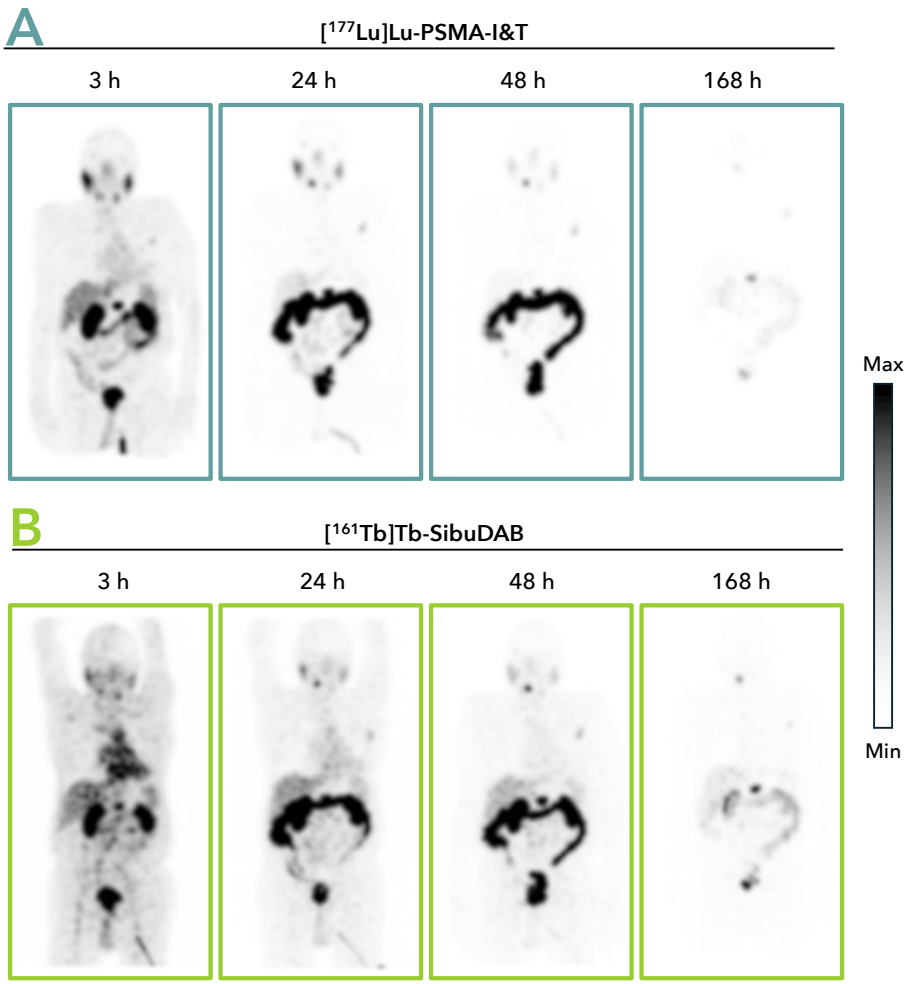

FIGURE 5.7. Maximum intensity projections from the MC-based SPECT reconstructions (6i10s) at 3 h, 24 h, 72 h, and 168 h post-injection for [^{177}Lu]Lu-PSMA-I&T (A) and [^{161}Tb]Tb-SibuDAB (B). Equal gray scaling is applied to all images, with voxels values in unit of activity.

For [^{161}Tb]Tb-DOTA-LM3, significantly elevated activity concentrations were observed across all examined tissues, along with higher total measured activity, as compared to [^{177}Lu]Lu-DOTATOC (Figure 5.8). At Day 7, 16% of the injected activity remained within the FOVs for [^{161}Tb]Tb-DOTA-LM3, compared to 3.9% for [^{177}Lu]Lu-DOTATOC. High tumor concentrations were also observed, with a peak measured activity concentration of 1.6 MBq/mL at 24 h p.i. (Tumor 3) for [^{161}Tb]Tb-DOTA-LM3, compared to 0.26 MBq/mL for [^{177}Lu]Lu-DOTATOC (Figure 5.8).

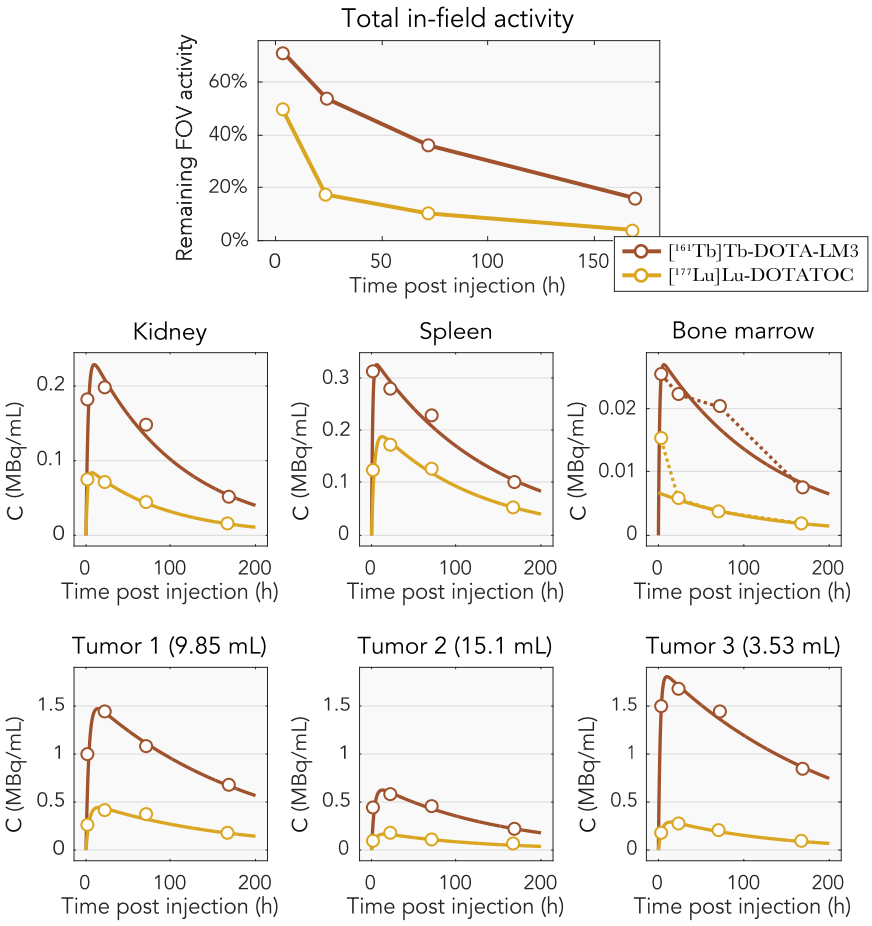

FIGURE 5.8. Time-activity curves (TACs) for [^{161}Tb]Tb-DOTA-LM3 and [^{177}Lu]Lu-DOTATOC used for dosimetry in the BETA PLUS trial (Paper IV), for kidneys, spleen, bone marrow, and three selected tumors. Also shown is the total in-field activity at each imaging time point (3 h, 24 h, 72 h, and 168 h post-injection).

For [^{161}Tb]Tb-SibuDAB and [^{177}Lu]Lu-PSMA-I&T, activity concentrations were comparable within the first day post administration, except for the parotid glands, which exhibited higher uptake for [^{177}Lu]Lu-PSMA-I&T (47 vs. 73 kBq/mL at 3 h). However, longer retention was generally observed for [^{161}Tb]Tb-SibuDAB (see Figure 5.9). At Day 7, 9.2% of the administered activity remained for [^{161}Tb]Tb-SibuDAB, compared to 1.3% for [^{177}Lu]Lu-PSMA-I&T.

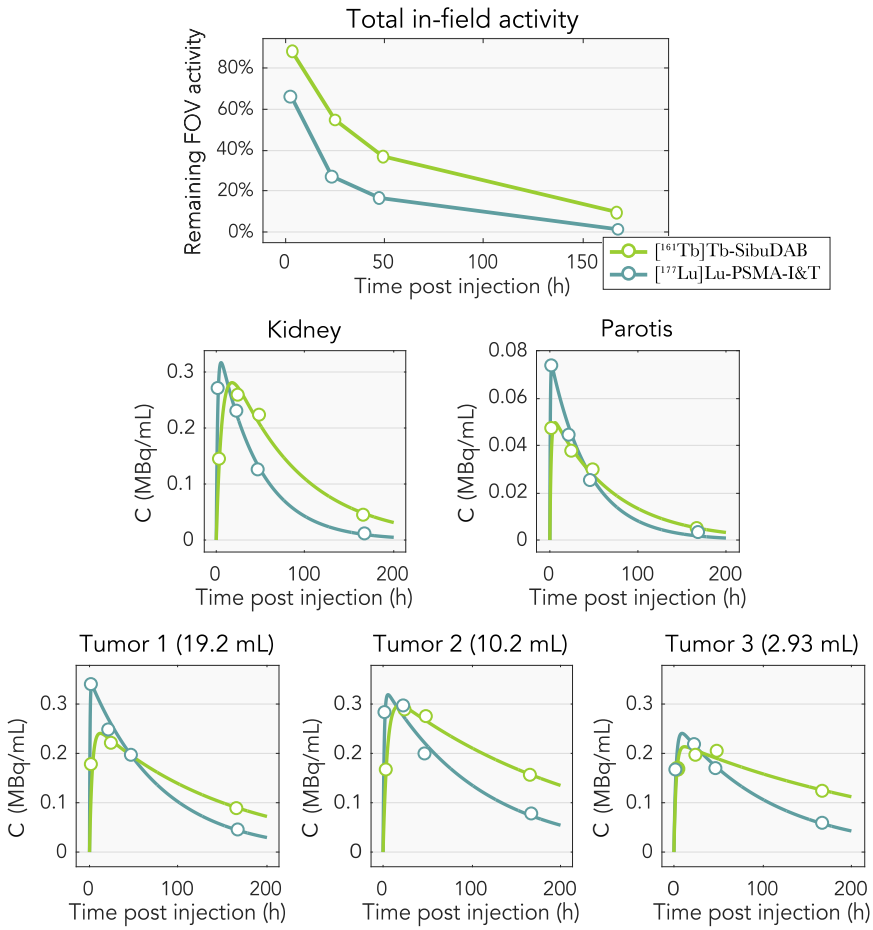

FIGURE 5.9. Time-activity curves (TACs) for [^{161}Tb]Tb-SibuDAB and [^{177}Lu]Lu-PSMA-I&T used for dosimetry in the PROGNOSTICs trial (Paper IV), for kidneys, parotis, and three selected tumors. Also shown is the total in-field activity at each imaging time point (3 h, 24 h, 48 h, and 168 h post-injection).

The resulting absorbed dose estimates and effective half-lives, presented in Tables 5.2 and 5.3, align with these observations. For [^{161}Tb]Tb-DOTA-LM3, the mean tumor absorbed dose was 8.1 times higher compared to [^{177}Lu]Lu-DOTATOC. The corresponding increases for the kidneys, spleen, and bone marrow were factors of 4.8, 2.8, and 6.3, respectively. For [^{161}Tb]Tb-SibuDAB, the mean tumor absorbed dose was 2.3 times higher compared to [^{177}Lu]Lu-PSMA-I&T, with corresponding increases of 2.1 for the kidneys and 1.5 for the parotid glands.

TABLE 5.2. Absorbed doses, D, and effective half-lives, T_{eff}, after 1 GBq of [^{161}Tb]Tb-DOTA-LM3 and [^{177}Lu]Lu-DOTATOC, respectively.

	[^{161}Tb]Tb-DOTA-LM3		[^{177}Lu]Lu-DOTATOC	
Organ	*D* (Gy/GBq)	T_{eff} (h)	*D* (Gy/GBq)	T_{eff} (h)
Left kidney	2.8	74	0.56	65
Right kidney	2.8	78	0.61	70
Spleen	5.0	98	1.8	83
Bone marrow	0.40	93	0.064	85
Tumor 1 (9.85 mL)	32	132	5.7	111
Tumor 2 (15.1 mL)	10	101	1.7	84
Tumor 3 (3.53 mL)	42	146	3.0	87

TABLE 5.3. Absorbed doses, D, and effective half-lives, T_{eff}, after 1 GBq [^{161}Tb]Tb-SibuDAB and [^{177}Lu]Lu-PSMA-I&T, respectively.

	[^{161}Tb]Tb-SibuDAB		[^{177}Lu]Lu-PSMA-I&T	
Organ	*D* (Gy/GBq)	T_{eff} (h)	*D* (Gy/GBq)	T_{eff} (h)
Left kidney	1.8	60	0.89	32
Right kidney	2.8	62	1.28	33
Left parotis	0.38	49	0.27	30
Right parotis	0.46	45	0.28	18
Tumor 1 (19.2 mL)	4.0	106	2.3	56
Tumor 2 (10.2 mL)	7.3	155	3.0	76
Tumor 3 (2.93 mL)	6.2	136	2.4	70

6 DISCUSSION

The results from Paper I suggest that accurate SPECT/CT-based ^{161}Tb activity quantification is feasible using clinical reconstruction software, and that a MEGP collimator with a 75 keV ± 10% energy window appears to be the preferable option (based on RQEs closer to zero, and less dependency on VOI volume and measurement geometry in the CF evaluation).

Nevertheless, indications of scatter degradation were observed, manifesting as a strong dependence on measurement and VOI geometry in CF determination. Regardless of collimator choice, sphCFs were deemed unsuitable due to their high dependence on VOI volume, while uniCFs appeared more stable. This emphasizes the need for an optimized acquisition and/or reconstruction protocol, even for MEGP.

Furthermore, the anthropomorphic phantom studies demonstrated that while MEGP provided RQEs closer to zero, LEHR was superior in terms of spatial resolution and contrast (i.e., higher RCs and more distinct line profiles), as previously reported (29). Moreover, the 49 keV window performed worse than the 75 keV window both visually and quantitatively, regardless of collimator. Nonetheless, it was concluded that the 49 keV window could be useful for late imaging time points due to its significantly higher CF (roughly a factor of 3), provided that the window settings are optimized, and that the scatter correction is improved.

Furthermore, dead-time effects emerged as a concern, as RQEs decreased with increasing activity—an effect more pronounced for LEHR and ELEGP. This trend was attributed to septal penetration from high-energy photon emissions, causing an elevated wide-spectrum count rate (more than doubled for LEHR and ELEGP, compared to MEGP).

In Paper II, these effects were further investigated, confirming that ^{161}Tb is particularly susceptible to dead-time effects, especially in the presence of septal penetration.

The derived dead-time constant (τ = 0.42 µs) was similar to, but slightly lower than, that reported for ^{177}Lu on similar systems (τ = 0.55 µs) (67), suggesting slightly improved measurement capability in terms of the wide-spectrum count rate, potentially due to the lower photon energy of ^{161}Tb placing less strain on the PHA. That said, ^{161}Tb still produces a high wide-spectrum count rate *per unit activity*, effectively limiting the maximum measurable activity, particularly in the presence of septal penetration.

Concerning septal penetration, a maximum PF of 22% was observed with the LEHR collimator at 75 keV, compared to 5% with MELP at the corresponding source-to-collimator distance. When comparing LEHR to MELP, the total wide-spectrum count rate was increased by roughly 40%, indicating that the use of a medium-energy collimator would increase the maximum measurable activity by the corresponding margin. Notably, this difference is smaller than for the GE system in Paper I, likely due to differences in collimator design and crystal thickness.

Based on the derived dead-time constant, it was concluded that no dead-time effects should occur below in-field activities of 1.2 GBq for LEHR and 1.7 GBq for MELP. This contrasts with the findings in Paper I, where dead-time effects appeared to arise at 460 MBq (i.e., an SBR of 1:20) for ELEGP and LEHR.

The discrepancy can be attributed to two main factors: (1) the larger wide-spectrum count rate observed for ELEGP and LEHR with the GE system, and (2) an inferior temporal resolution of the GE system. While dead time was not explicitly measured for the GE camera in Paper I, others have performed direct comparisons between similar GE and Siemens systems, reporting substantially higher dead-time constants for GE—e.g., $\tau = 1.74$ µs vs. $\tau = 0.49$ µs for ^{99m}Tc (68)—supporting this conclusion.

As for the calibration measurements performed in preparation for Papers III and IV, no dead-time effects were observed in the Lung-Spine and NEMA acquisitions (conducted with activities similar to those in Paper I), and satisfactory quantitative accuracy was obtained when applying the proposed quantification methods (*data not shown*). Based on these findings, it was concluded that dead time would not pose a major issue for clinical imaging in Papers III and IV, which informed the decision to employ the LEHR collimator.

Concerning the dosimetry results in Papers III and IV, higher tumor absorbed doses and favorable tumor-to-organ-at-risk ratios were generally observed for both ^{161}Tb-labeled compounds compared to their ^{177}Lu-labeled counterparts, in line with preclinical predictions (132,143). Minor discrepancies compared to previously published absorbed doses may be noted, as CFs have since been updated and segmentation re-performed. The values presented here represent the current best estimates.

First, the obtained TACs clearly highlight the pharmacokinetic differences between the examined compounds. [^{161}Tb]Tb-SibuDAB was mostly characterized by prolonged retention (in line with its albumin-binding properties), thus resulting in higher absorbed doses.

In contrast, [^{161}Tb]Tb-DOTA-LM3 demonstrated both significantly higher uptake and a longer effective half-life than [^{177}Lu]Lu-DOTATOC, as expected for SSTR agonists due to their ability to bind strongly to a larger number of sites (*128*).

These pharmacokinetic differences naturally affected the resulting absorbed doses to organs at risk. For [^{161}Tb]Tb-DOTA-LM3, normal organ absorbed doses were notably high, particularly for the bone marrow (0.40 Gy/GBq). This highlights the increased risk of hematological toxicity, previously reported for SSTR antagonists (*131*). Nonetheless, the mean tumor-to-bone marrow absorbed dose remained favorable (70 vs. 54 for [^{177}Lu]Lu-DOTATOC), underscoring its therapeutic potential.

For [^{161}Tb]Tb-SibuDAB, while tumor doses were higher (roughly 2.3-fold), the increase in therapeutic index was not as pronounced. The tumor-to-parotid absorbed dose ratio was clearly favorable for [^{161}Tb]Tb-SibuDAB compared to [^{177}Lu]Lu-PSMA-I&T (a 1.5-fold increase for [^{161}Tb]Tb-SibuDAB), whereas the increase in average kidney absorbed dose was comparable but slightly lower than that of the average tumor absorbed dose (a 2.1-fold increase).

Based on these initial findings, both [^{161}Tb]Tb-DOTA-LM3 and [^{161}Tb]Tb-SibuDAB appear to be promising candidates for radionuclide therapy of NETs and mCRPC, respectively. Moreover, the use of [^{161}Tb]Tb-SibuDAB and [^{161}Tb]Tb-DOTA-LM3 could offer some important logistical advantages. The increased uptake and/or higher absorbed doses observed for both ligands suggest that a lower administered activity could be used to achieve the same therapeutic effect, compared to current clinical options—an important consideration given the anticipated future shortage of ^{177}Lu (*152*). Notably, on March 28, 2025, the FDA expanded the indication for [^{177}Lu]Lu-PSMA-617 (*153*), increasing the number of mCRPC patients eligible for treatment. In this context, ligands such as [^{161}Tb]Tb-SibuDAB—if proven safe and effective—could help meet a growing clinical demand.

It should be emphasized that the observations above pertain only to the initial patients presented in Papers III and IV, and not to the full study cohorts, as those data have yet to be published.

7 FUTURE PERSPECTIVES

Much remains to be explored regarding the technical aspects of ^{161}Tb SPECT/CT imaging. Further characterization is needed, including a more detailed assessment of dead-time effects under more patient-like acquisition conditions. An optimization of the window-based scatter correction is also required to achieve more accurate and clinically attainable reconstructions. Furthermore, continued optimization of SARec (*89*) is essential, particularly with respect to accurately modeling septal penetration from high-energy γ-emissions.

In addition, the impact of ^{160}Tb contamination warrants further investigation. This impurity emits high-yield, high-energy γ-rays, which could degrade image quality if present in larger amounts. In these studies, high-purity ^{161}Tb was used, and no image degradation attributable to ^{160}Tb was observed. However, allowing a higher ^{160}Tb content would facilitate the production of larger quantities of ^{161}Tb (*19*), meaning that future production upscaling could require a trade-off between radionuclidic purity and production yield—one that would need to be carefully evaluated with respect to its effect on image quality.

The potential use of the 49 keV window also merits exploration, as its high sensitivity could offer distinct advantages. Although currently less accurate, the application of optimized MC-based methods—e.g., improved modeling of collimator X-rays and scatter—may enable late time-point quantification with reduced noise degradation, which is particularly desirable in low-activity regions such as the bone marrow.

A more thorough validation of the dosimetry methodologies for [^{161}Tb]Tb-DOTA-LM3 and [^{161}Tb]Tb-SibuDAB is required, particularly with respect to TAC fitting. The prolonged circulation of [^{161}Tb]Tb-SibuDAB may render conventional mono- or biexponential models unsuitable, necessitating further evaluation of alternative fitting approaches. In addition, salivary gland dosimetry for both [^{161}Tb]Tb-SibuDAB and [^{177}Lu]Lu-PSMA-I&T requires further validation, as PVEs are particularly pronounced for this organ.

From a clinical perspective, continued evaluation of the safety and efficacy of [^{161}Tb]Tb-DOTA-LM3 and [^{161}Tb]Tb-SibuDAB is essential. Both trials are currently in their second subphases. Given the prolonged retention of these compounds, potential adverse effects on normal organs—particularly hematological toxicity—must be closely monitored. Clinical dosimetry in larger patient cohorts will be crucial for optimizing administration schemes and, if warranted, supporting regulatory approval.

SUMMARIZING THOUGHTS

To understand the challenges associated with ^{161}Tb SPECT quantification, we must begin at the core: the ^{161}Tb decay. The very features that make ^{161}Tb attractive for therapy (i.e., its significant low-energy electron emission) also complicate its use in imaging. As discussed in Section 2.2.3, the emission of Auger and conversion electrons competes with the emission of γ- and X-rays, resulting in a complex photon spectrum spanning a wide energy range.

Although the high-energy γ-emissions have low yield, their impact can be substantial. Without adequate collimation, these emissions can significantly increase the total recorded count rate via septal penetration. This, combined with the high-intensity X-rays, makes ^{161}Tb measurements particularly susceptible to dead time—something to be considered in both quantification and calibration.

A personal experience illustrates this quite well: during the Paper I data collection, I struggled to obtain good-quality intrinsic uniformity maps. Initially, I followed the NEMA guidelines, which state that "*the count rate shall not exceed 20,000 cps through a photopeak window […] for the appropriate clinical mode*" (*146*). In adhering to this limit for the 75 keV window, I failed to recognize the much higher wide-spectrum count rate, resulting in dead-time artifacts (manifesting as non-linearity) and, consequently, uniformity artifacts in the reconstructed images. This experience highlights the importance of accounting for the elevated wide-spectrum count rate in all aspects of ^{161}Tb γ-camera imaging.

In the context of dosimetry, dead time may be a less critical concern. Significant losses appear to occur at activity levels on the order of several hundred MBq, and are likely negligible beyond the first day post-injection. That said, modern systems clearly differ significantly in how they handle of dead time, and the activity threshold at which dead-time losses become relevant may vary between vendors.

Perhaps more pressing is the trade-off in collimator selection imposed by ^{161}Tb's emission profile. While low-energy collimators can provide satisfactory visual image quality—as demonstrated in Paper I, and consistent with the findings of Marin et al. (*29*) and MacIntosh et al. (*151*)—they also promote penetration and scatter, which undermines quantitative accuracy. In this regard, using a medium-energy collimator appears to be a safer option, as it minimizes both penetration and dead-time effects.

That said, context matters. In the clinical trials in Papers III and IV, a low-energy collimator was employed—partly because calibration was already underway when the associated issues became apparent, and partly because resolution was prioritized.

Given the low administered activities in these early-phase studies, dead time was not a major concern. Thus, we could accept the known limitations of low-energy collimation in favor of achieving good visual image quality.

So, where does that leave us? Although I would have loved to propose an optimal collimator design within this thesis, that lies beyond its current scope. Nonetheless, it is clear that medium-energy collimation offers greater robustness for SPECT/CT-based ^{161}Tb quantification. While this comes at the expense of spatial resolution, it should provide more favorable conditions for accurate dosimetry. Although some centers might have the tools and expertise to compensate for the degrading effects associated with low-energy collimation (e.g., a robust MC-based reconstruction), such resources are not universally available. Therefore, prioritizing hardware choices that support accurate quantification may be the safer and more broadly applicable approach—at least for now, given current technology. In a broader perspective, this may also help establish more reliable dose–response relationships, which are essential for the advancement of radionuclide therapy.

To circle back to the core point: the very properties that make ^{161}Tb an exciting therapeutic radionuclide are also the ones that complicate imaging. With growing access to improved correction algorithms, AI-based tools, and shared expertise in general, accurate image-based ^{161}Tb dosimetry is certainly within reach. That said, awareness of the underlying physics—and its impact on the resulting image quality—remains essential. This thesis, I hope, contributes to that understanding and helps pave the way for more informed ^{161}Tb SPECT imaging in the future.

REFERENCES

1. The National Board of Health and Welfare; The Swedish Cancer Society. Cancer i siffror 2023: Populärvetenskapliga fakta om cancer [Cancer in Numbers 2023: Popular Science Facts About Cancer]. Stockholm, Sweden: The National Board of Health and Welfare and Swedish Cancer Society; 2023.
2. Strebhardt K, Ullrich A. Paul Ehrlich's magic bullet concept: 100 years of progress. Nat Rev Cancer. 2008;8(6):473-480. doi:10.1038/nrc2394
3. Hevesy G. The Absorption and Translocation of Lead by Plants: A Contribution to the Application of the Method of Radioactive Indicators in the Investigation of the Change of Substance in Plants. Biochem J. 1923;17(4-5):439-45. doi: 10.1042/bj0170439.
4. Blumgart, H. L., & Weiss, S. (1927). Studies on the Velocity of Blood Flow: V. The Physiological and the Pathological Significance of the Velocity of Blood Flow. The Journal of Clinical Investigation, 4(2), 199-209.
5. Tuttle LW, Scott KG, Lawrence JH. Phosphorus Metabolism in Leukemic Blood. Proceedings of the Society for Experimental Biology and Medicine. 1939;41(1):20-25. doi:10.3181/00379727-41-10556
6. Ehrhardt JD Jr, Güleç S. A Review of the History of Radioactive Iodine Theranostics: The Origin of Nuclear Ontology. Mol Imaging Radionucl Ther. 2020;29(3):88-97. doi:10.4274/mirt.galenos.2020.83703
7. Krenning EP, Kooij PP, Bakker WH, et al. Radiotherapy with a radiolabeled somatostatin analogue, [^{111}In-DTPA-D-Phe1]-octreotide. A case history. Ann N Y Acad Sci. 1994;733:496-506. doi:10.1111/j.1749-6632.1994.tb17300.x
8. Myers WG. Nuclear Medicine Pioneer Citation-1974. Hal Oscar Anger, D.Sc. (Hon.). J Nucl Med. 1974;15(6):471-473.
9. Hutton BF. The origins of SPECT and SPECT/CT. Eur J Nucl Med Mol Imaging. 2014;41 Suppl 1:S3-S16. doi:10.1007/s00259-013-2606-5
10. Wagner HN Jr. A brief history of positron emission tomography (PET). Semin Nucl Med. 1998;28(3):213-220. doi:10.1016/s0001-2998(98)80027-5
11. Strosberg JR, Caplin ME, Kunz PL, et al. ^{177}Lu-DOTATATE plus long-acting octreotide versus high-dose long-acting octreotide in patients with midgut neuroendocrine tumours (NETTER-1): final overall survival and long-term safety results from an open-label, randomised, controlled, phase 3 trial [published correction appears in Lancet Oncol. 2022 Feb;23(2):e59. doi: 10.1016/S1470-2045(22)00028-6.]. Lancet Oncol. 2021;22(12):1752-1763. doi:10.1016/S1470-2045(21)00572-6

12. Sartor, O., De Bono, J., Chi, K. N., Fizazi, K., Herrmann, K., Rahbar, K., ... & Krause, B. J. (2021). Lutetium-177–PSMA-617 for metastatic castration-resistant prostate cancer. New England Journal of Medicine, 385(12), 1091-1103.
13. Zhang S, Wang X, Gao X, et al. Radiopharmaceuticals and their applications in medicine. Signal Transduct Target Ther. 2025;10(1):1. Published 2025 Jan 3. doi:10.1038/s41392-024-02041-6
14. Silberstein EB. Radioiodine: the classic theranostic agent. Semin Nucl Med. 2012;42(3):164-170. doi:10.1053/j.semnuclmed.2011.12.002
15. Tansjö L. Carl Gustaf Mosander and his research on rare earths. In: Evans CH, ed. Episodes from the History of the Rare Earth Elements. Kluwer Academic Publishers; 1996:37-49. doi:10.1007/978-94-009-0287-9
16. Live Chart of Nuclides – Nuclear Structure and Decay Data. International Atomic Energy Agency (IAEA). Updated June 1, 2011. Accessed April 1, 2025. https://www-nds.iaea.org/relnsd/vcharthtml/VChartHTML.html
17. Müller C, Zhernosekov K, Köster U, et al. A unique matched quadruplet of terbium radioisotopes for PET and SPECT and for α- and β- radionuclide therapy: an in vivo proof-of-concept study with a new receptor-targeted folate derivative. J Nucl Med. 2012;53(12):1951-1959. doi:10.2967/jnumed.112.107540
18. Eckerman K, Endo A. ICRP Publication 107. Nuclear decay data for dosimetric calculations. Ann ICRP. 2008;38(3):7-96. doi:10.1016/j.icrp.2008.10.004
19. Moiseeva AN, Favaretto C, Talip Z, Grundler PV, van der Meulen NP. Terbium sisters: current development status and upscaling opportunities. Front Nucl Med. 2024;4:1472500. Published 2024 Oct 11. doi:10.3389/fnume.2024.1472500
20. de Jong M, Breeman WA, Bernard BF, et al. Evaluation in vitro and in rats of ^{161}Tb-DTPA-octreotide, a somatostatin analogue with potential for intraoperative scanning and radiotherapy. Eur J Nucl Med. 1995;22(7):608-616. doi:10.1007/BF01254561
21. Bernhardt P, Benjegård SA, Kölby L, et al. Dosimetric comparison of radionuclides for therapy of somatostatin receptor-expressing tumors. Int J Radiat Oncol Biol Phys. 2001;51(2):514-524. doi:10.1016/s0360-3016(01)01663-7
22. Uusijärvi H, Bernhardt P, Rösch F, Maecke HR, Forssell-Aronsson E. Electron- and positron-emitting radiolanthanides for therapy: aspects of dosimetry and production. J Nucl Med. 2006;47(5):807-814.
23. Müller C, Reber J, Haller S, et al. Direct in vitro and in vivo comparison of (161)Tb and (177)Lu using a tumour-targeting folate conjugate. Eur J Nucl Med Mol Imaging. 2014;41(3):476-485. doi:10.1007/s00259-013-2563-z
24. Haller S, Pellegrini G, Vermeulen C, et al. Contribution of Auger/conversion electrons to renal side effects after radionuclide therapy: preclinical comparison

of (161)Tb-folate and (177)Lu-folate. EJNMMI Res. 2016;6(1):13. doi:10.1186/s13550-016-0171-1

25. Lehenberger S, Barkhausen C, Cohrs S, et al. The low-energy β(-) and electron emitter (161)Tb as an alternative to (177)Lu for targeted radionuclide therapy. Nucl Med Biol. 2011;38(6):917-924. doi:10.1016/j.nucmedbio.2011.02.007
26. Hindié E, Zanotti-Fregonara P, Quinto MA, Morgat C, Champion C. Dose Deposits from ^{90}Y, ^{177}Lu, ^{111}In, and ^{161}Tb in Micrometastases of Various Sizes: Implications for Radiopharmaceutical Therapy. J Nucl Med. 2016;57(5):759-764. doi:10.2967/jnumed.115.170423
27. Champion C, Quinto MA, Morgat C, Zanotti-Fregonara P, Hindié E. Comparison between Three Promising ß-emitting Radionuclides, (67)Cu, (47)Sc and (161)Tb, with Emphasis on Doses Delivered to Minimal Residual Disease. Theranostics. 2016;6(10):1611-1618. Published 2016 Jun 18. doi:10.7150/thno.15132
28. Alcocer-Ávila ME, Ferreira A, Quinto MA, Morgat C, Hindié E, Champion C. Radiation doses from ^{161}Tb and ^{177}Lu in single tumour cells and micrometastases. EJNMMI Phys. 2020;7(1):33. Published 2020 May 19. doi:10.1186/s40658-020-00301-2
29. Marin I, Rydèn T, Van Essen M, et al. Establishment of a clinical SPECT/CT protocol for imaging of ^{161}Tb. EJNMMI Phys. 2020;7(1):45. Published 2020 Jul 1. doi:10.1186/s40658-020-00314-x
30. Baum RP, Singh A, Kulkarni HR, et al. First-in-Humans Application of ^{161}Tb: A Feasibility Study Using ^{161}Tb-DOTATOC. J Nucl Med. 2021;62(10):1391-1397. doi:10.2967/jnumed.120.258376
31. Borgna F, Barritt P, Grundler PV, et al. Simultaneous Visualization of ^{161}Tb- and ^{177}Lu-Labeled Somatostatin Analogues Using Dual-Isotope SPECT Imaging. Pharmaceutics. 2021;13(4):536. Published 2021 Apr 12. doi:10.3390/pharmaceutics13040536
32. Borgna F, Haller S, Rodriguez JMM, et al. Combination of terbium-161 with somatostatin receptor antagonists-a potential paradigm shift for the treatment of neuroendocrine neoplasms. Eur J Nucl Med Mol Imaging. 2022;49(4):1113-1126. doi:10.1007/s00259-021-05564-0
33. Müller C, Umbricht CA, Gracheva N, et al. Terbium-161 for PSMA-targeted radionuclide therapy of prostate cancer. Eur J Nucl Med Mol Imaging. 2019;46(9):1919-1930. doi:10.1007/s00259-019-04345-0
34. Borbinha J, Ferreira P, Costa D, Vaz P, Di Maria S. Targeted radionuclide therapy directed to the tumor phenotypes: A dosimetric approach using MC

simulations. Appl Radiat Isot. 2023;192:110569. doi:10.1016/j.apradiso.2022.110569

35. De Nardo L, Santi S, Dalla Pietà A, et al. Comparison of the dosimetry and cell survival effect of ^{177}Lu and ^{161}Tb somatostatin analog radiopharmaceuticals in cancer cell clusters and micrometastases. EJNMMI Phys. 2024;11(1):94. Published 2024 Nov 13. doi:10.1186/s40658-024-00696-2
36. Bernhardt P, Svensson J, Hemmingsson J, et al. Dosimetric Analysis of the Short-Ranged Particle Emitter ^{161}Tb for Radionuclide Therapy of Metastatic Prostate Cancer. Cancers (Basel). 2021;13(9):2011. Published 2021 Apr 22. doi:10.3390/cancers13092011
37. Verburg FA, de Blois E, Koolen S, Konijnenberg MW. Replacing Lu-177 with Tb-161 in DOTA-TATE and PSMA-617 therapy: potential dosimetric implications for activity selection. EJNMMI Phys. 2023;10(1):69. Published 2023 Nov 10. doi:10.1186/s40658-023-00589-w
38. Gracheva N, Müller C, Talip Z, et al. Production and characterization of no-carrier-added ^{161}Tb as an alternative to the clinically-applied ^{177}Lu for radionuclide therapy. EJNMMI Radiopharm Chem. 2019;4(1):12. Published 2019 Jul 10. doi:10.1186/s41181-019-0063-6
39. Arman MÖ, Mullaliu A, Geboes B, et al. Separation of terbium as a first step towards high purity terbium-161 for medical applications. RSC Adv. 2024;14(28):19926-19934. Published 2024 Jun 20. doi:10.1039/d4ra02694b
40. Holiski CK, Bender AA, Monte PF, et al. The production and separation of ^{161}Tb with high specific activity at the University of Utah. Appl Radiat Isot. 2024;214:111530. doi:10.1016/j.apradiso.2024.111530
41. Gizawy MA, El-Din AMS, Borai EH, Mohamed NMA. Production and radiochemical separation of Tb-161 as a feasible beta therapeutic radioisotope from reactor irradiated Gd target. J Chromatogr A. 2024;1737:465439. doi:10.1016/j.chroma.2024.465439
42. Favaretto C, Grundler PV, Talip Z, et al. ^{161}Tb-DOTATOC Production Using a Fully Automated Disposable Cassette System: A First Step Toward the Introduction of ^{161}Tb into the Clinic. J Nucl Med. 2023;64(7):1138-1144. doi:10.2967/jnumed.122.265268
43. Abdlkadir AS, Abufara A, Al-Ibraheem A. Dual Radionuclide Therapy: The Synergistic Effects of [^{161}Tb]Tb-PSMA and [^{177}Lu]Lu-PSMA in Advanced Prostate Cancer Post [^{177}Lu]Lu-PSMA Failure [published correction appears in Nucl Med Mol Imaging. 2025 Feb;59(1):94. doi: 10.1007/s13139-024-00887-w.]. Nucl Med Mol Imaging. 2024;58(6):381-382. doi:10.1007/s13139-024-00871-4

44. Al-Ibraheem A, Abdlkadir AS, Sweedat DA, et al. From Despair to Hope: First Arabic Experience of ^{177}Lu-PSMA and ^{161}Tb-PSMA Therapy for Metastatic Castration-Resistant Prostate Cancer. Cancers (Basel). 2024;16(11):1974. Published 2024 May 23. doi:10.3390/cancers16111974
45. Buteau JP, Kostos L, Alipour R, et al. Clinical Trial Protocol for VIOLET: A Single-Center, Phase I/II Trial Evaluation of Radioligand Treatment in Patients with Metastatic Castration-Resistant Prostate Cancer with [^{161}Tb]Tb-PSMA-I&T. J Nucl Med. 2024;65(8):1231-1238. Published 2024 Aug 1. doi:10.2967/jnumed.124.267650
46. Rosar F, Maus S, Schaefer-Schuler A, Burgard C, Khreish F, Ezziddin S. New Horizons in Radioligand Therapy: ^{161}Tb-PSMA-617 in Advanced mCRPC. Clin Nucl Med. 2023;48(5):433-434. doi:10.1097/RLU.0000000000004589
47. Schaefer-Schuler A, Burgard C, Blickle A, et al. [^{161}Tb]Tb-PSMA-617 radioligand therapy in patients with mCRPC: preliminary dosimetry results and intra-individual head-to-head comparison to [^{177}Lu]Lu-PSMA-617. Theranostics. 2024;14(5):1829-1840. Published 2024 Feb 24. doi:10.7150/thno.92273
48. Chirindel A, Nicolas GP, Westerbergh F, et al. First-in-human administration of [^{161}Tb]Tb-SibuDAB and comparative dosimetry with standard [^{177}Lu]Lu-PSMA-I&T as part of the PROGNOSTICS phase Ia study. Eur J Nucl Med Mol Imaging. 2025;52(5):1628-1630. doi:10.1007/s00259-024-07009-w
49. Fricke J, Westerbergh F, McDougall L, et al. First-in-human administration of terbium-161-labelled somatostatin receptor subtype 2 antagonist ([^{161}Tb]Tb-DOTA-LM3) in a patient with a metastatic neuroendocrine tumour of the ileum. Eur J Nucl Med Mol Imaging. 2024;51(8):2517-2519. doi:10.1007/s00259-024-06641-w
50. Laboratoire National Henri Becquerel (LNHB). NUCLÉIDE-LARA on the Web: Decay Data for ^{160}Tb (original source: Nuclear Data Sheets [NDS] 78 & 105, 2008). Accessed April 4, 2025. http://www.lnhb.fr/Laraweb/
51. Durán MT, Juget F, Nedjadi Y, et al. Determination of ^{161}Tb half-life by three measurement methods. Appl Radiat Isot. 2020;159:109085. doi:10.1016/j.apradiso.2020.109085
52. Dong J, Bai T, Hu Y, et al. Determination of the half-life of ^{161}Tb. Appl Radiat Isot. 2023;193:110647. doi:10.1016/j.apradiso.2022.110647
53. Laboratoire National Henri Becquerel (LNHB). NUCLÉIDE-LARA on the Web: Decay Data for ^{177}Lu (original source: Argonne National Laboratory [ANL], 2003). Accessed April 4, 2025. http://www.lnhb.fr/Laraweb/

54. Laboratoire National Henri Becquerel (LNHB). NUCLÉIDE-LARA on the Web: Decay Data for ^{161}Tb (original source: Nuclear Data Sheets [NDS] 112, 2011–2014). Accessed April 4, 2025. http://www.lnhb.fr/Laraweb/
55. Juget F, Talip Z, Buchillier T, et al. Determination of the gamma and X-ray emission intensities of terbium-161 [published correction appears in Appl Radiat Isot. 2023 Oct;200:110955. doi: 10.1016/j.apradiso.2023.110955.]. Appl Radiat Isot. 2021;174:109770. doi:10.1016/j.apradiso.2021.109770
56. Ljungberg M, Celler A, Konijnenberg MW, et al. MIRD Pamphlet No. 26: Joint EANM/MIRD Guidelines for Quantitative ^{177}Lu SPECT Applied for Dosimetry of Radiopharmaceutical Therapy. J Nucl Med. 2016;57(1):151-162. doi:10.2967/jnumed.115.159012
57. Goddu SM, Howell RW, Bouchet LG, Bolch WE, Rao DV, eds. MIRD Cellular S Values: Self-Absorbed Dose per Unit Cumulated Activity for Selected Radionuclides and Monoenergetic Electron and Alpha Particle Emitters Incorporated into Different Cell Compartments. Society of Nuclear Medicine; 1997.
58. Peterson TE, Furenlid LR. SPECT detectors: the Anger Camera and beyond. Phys Med Biol. 2011;56(17):R145-R182. doi:10.1088/0031-9155/56/17/R01
59. Laboratoire National Henri Becquerel (LNHB). NUCLÉIDE-LARA on the Web: Decay Data for ^{99m}Tc (original source: CEA/LNE-LNHB, KRI, 2004). Published 2022. Accessed April 4, 2025. http://www.lnhb.fr/Laraweb/
60. Knoll GF. Radiation Detection and Measurement. 4th ed. USA: Wiley; 2010. Ch. 8, Scintillation Detection Principles; p. 219-247.
61. Cherry SR, JA Sorenson, ME Phelps. Physics in Nuclear Medicine. 4th ed. Philadelphia (US): Saunders, Elsevier Health Sciences; 2012. Ch. 13: The Gamma Camera: Basic Principles; p. 195-206.
62. Ritt P. Recent Developments in SPECT/CT. Semin Nucl Med. 2022;52(3):276-285. doi:10.1053/j.semnuclmed.2022.01.004
63. Van Eijk CWE. Ch. 6: Basic Radiation Detectors. In: Bailey DL, Humm JL, Todd-Pokropek A, van Aswegen A, editors. Nuclear Medicine Physics: A Handbook for Teachers and Students. Vienna: International Atomic Energy Agency; 2014. p. 199-200.
64. Zanzonico PB. Ch 10: Non-Imaging Detectors and Counters. In: Bailey DL, Humm JL, Todd-Pokropek A, van Aswegen A, editors. Nuclear Medicine Physics: A Handbook for Teachers and Students. Vienna: International Atomic Energy Agency; 2014. p. 298.

65. Cherry SR, JA Sorenson, ME Phelps. Physics in Nuclear Medicine. 4th ed. Philadelphia (US): Saunders, Elsevier Health Sciences; 2012. Ch. 14: The Gamma Camera: Performance Characteristics; p. 209-231.
66. Desy A, Bouvet GF, Lafrenière N, Zamanian A, Després P, Beauregard JM. Impact of the dead-time correction method on quantitative ^{177}Lu-SPECT (QSPECT) and dosimetry during radiopharmaceutical therapy. EJNMMI Phys. 2022;9(1):54. Published 2022 Aug 17. doi:10.1186/s40658-022-00484-w
67. Frezza A, Desport C, Uribe C, et al. Comprehensive SPECT/CT system characterization and calibration for ^{177}Lu quantitative SPECT (QSPECT) with dead-time correction. EJNMMI Phys. 2020;7(1):10. Published 2020 Feb 14. doi:10.1186/s40658-020-0275-6
68. Desy A, Bouvet GF, Croteau É, et al. Quantitative SPECT (QSPECT) at high count rates with contemporary SPECT/CT systems. EJNMMI Phys. 2021;8(1):73. Published 2021 Oct 30. doi:10.1186/s40658-021-00421-3
69. Heemskerk JWT, Defrise M. Gamma detector dead time correction using Lambert W function. EJNMMI Phys. 2020;7(1):27. Published 2020 May 11. doi:10.1186/s40658-020-00296-w
70. Daube-Witherspoon ME. Ch. 8: Generic Performance Measures. In: Bailey DL, Humm JL, Todd-Pokropek A, van Aswegen A, editors. Nuclear Medicine Physics: A Handbook for Teachers and Students. Vienna: International Atomic Energy Agency; 2014. p. 234-250.
71. Hoog C, Koulibaly PM, Sas N, et al. 360° CZT-SPECT/CT cameras: ^{99m}Tc- and ^{177}Lu-phantom-based evaluation under clinical conditions. EJNMMI Phys. 2024;11(1):89. Published 2024 Oct 24. doi:10.1186/s40658-024-00684-6
72. Dewaraja YK, Frey EC, Sgouros G, Brill AB, Roberson P, Zanzonico PB, Ljungberg M. MIRD pamphlet No. 23: quantitative SPECT for patient-specific 3-dimensional dosimetry in internal radionuclide therapy. J Nucl Med. 2012 Aug;53(8):1310-25. doi: 10.2967/jnumed.111.100123. Epub 2012 Jun 28. PMID: 22743252; PMCID: PMC3465844.
73. Dickson JC, Armstrong IS, Gabiña PM, et al. EANM practice guideline for quantitative SPECT-CT. Eur J Nucl Med Mol Imaging. 2023;50(4):980-995. doi:10.1007/s00259-022-06028-9
74. Gustafsson J, Larsson E, Ljungberg M, Sjögreen Gleisner K. Pareto optimization of SPECT acquisition and reconstruction settings for ^{177}Lu activity quantification. EJNMMI Phys. 2024;11(1):62. Published 2024 Jul 15. doi:10.1186/s40658-024-00667-7
75. Wikberg E, Essen MV, Rydén T, Svensson J, Gjertsson P, Bernhardt P. Improvements of ^{177}Lu SPECT images from sparsely acquired projections by

reconstruction with deep-learning-generated synthetic projections. EJNMMI Phys. 2024;11(1):53. Published 2024 Jun 28. doi:10.1186/s40658-024-00655-x

76. Rydén T, Van Essen M, Marin I, Svensson J, Bernhardt P. Deep-Learning Generation of Synthetic Intermediate Projections Improves ^{177}Lu SPECT Images Reconstructed with Sparsely Acquired Projections. J Nucl Med. 2021;62(4):528-535. doi:10.2967/jnumed.120.245548
77. Leube J, Gustafsson J, Lassmann M, Salas-Ramirez M, Tran-Gia J. Analysis of a deep learning-based method for generation of SPECT projections based on a large Monte Carlo simulated dataset. EJNMMI Phys. 2022;9(1):47. Published 2022 Jul 19. doi:10.1186/s40658-022-00476-w
78. Minarik D, Enqvist O, Trägårdh E. Denoising of Scintillation Camera Images Using a Deep Convolutional Neural Network: A Monte Carlo Simulation Approach. J Nucl Med. 2020;61(2):298-303. doi:10.2967/jnumed.119.226613
79. Li Z, Fessler JA, Mikell JK, Wilderman SJ, Dewaraja YK. DblurDoseNet: A deep residual learning network for voxel radionuclide dosimetry compensating for single-photon emission computerized tomography imaging resolution. Med Phys. 2022;49(2):1216-1230. doi:10.1002/mp.15397
80. Shepp LA, Vardi Y. Maximum likelihood reconstruction for emission tomography. IEEE Trans Med Imaging. 1982;1(2):113-122. doi:10.1109/TMI.1982.4307558
81. Hudson HM, Larkin RS. Accelerated image reconstruction using ordered subsets of projection data. IEEE Trans Med Imaging. 1994;13(4):601-609. doi:10.1109/42.363108
82. Leube J, Claeys W, Gustafsson J, et al. Position dependence of recovery coefficients in ^{177}Lu-SPECT/CT reconstructions - phantom simulations and measurements. EJNMMI Phys. 2024;11(1):52. Published 2024 Jun 28. doi:10.1186/s40658-024-00662-y
83. Bailey DL, Willowson KP. Quantitative SPECT/CT: SPECT joins PET as a quantitative imaging modality. Eur J Nucl Med Mol Imaging. 2014;41 Suppl 1:S17-S25. doi:10.1007/s00259-013-2542-4
84. Patton JA, Turkington TG. SPECT/CT Physical Principles and Attenuation Correction. J Nucl Med Technol. 2008;36(1):1-10. doi:10.2967/jnmt.107.046839
85. Jaszczak RJ, Greer KL, Floyd CE Jr, Harris CC, Coleman RE. Improved SPECT quantification using compensation for scattered photons. J Nucl Med. 1984;25(8):893-900.
86. Ogawa K, Harata Y, Ichihara T, Kubo A, Hashimoto S. A practical method for position-dependent Compton-scatter correction in single photon emission CT. IEEE Trans Med Imaging. 1991;10(3):408-412. doi:10.1109/42.97591

87. Hutton BF, Buvat I, Beekman FJ. Review and current status of SPECT scatter correction. Phys Med Biol. 2011;56(14):R85-R112. doi:10.1088/0031-9155/56/14/R01
88. Ljungberg M, Strand SE. Scatter and attenuation correction in SPECT using density maps and Monte Carlo simulated scatter functions. J Nucl Med. 1990;31(9):1560-1567.
89. Rydén T, Heydorn Lagerlöf J, Hemmingsson J, et al. Fast GPU-based Monte Carlo code for SPECT/CT reconstructions generates improved ^{177}Lu images. EJNMMI Phys. 2018;5(1):1. Published 2018 Jan 4. doi:10.1186/s40658-017-0201-8
90. Xiang H, Lim H, Fessler JA, Dewaraja YK. A deep neural network for fast and accurate scatter estimation in quantitative SPECT/CT under challenging scatter conditions. Eur J Nucl Med Mol Imaging. 2020;47(13):2956-2967. doi:10.1007/s00259-020-04840-9
91. Kim H, Li Z, Son J, Fessler JA, Dewaraja YK, Chun SY. Physics-Guided Deep Scatter Estimation by Weak Supervision for Quantitative SPECT. IEEE Trans Med Imaging. 2023;42(10):2961-2973. doi:10.1109/TMI.2023.3270868
92. McMillan AB, Bradshaw TJ. Artificial Intelligence-Based Data Corrections for Attenuation and Scatter in Position Emission Tomography and Single-Photon Emission Computed Tomography. PET Clin. 2021;16(4):543-552. doi:10.1016/j.cpet.2021.06.010
93. Nuyts J. Unconstrained image reconstruction with resolution modelling does not have a unique solution. EJNMMI Phys. 2014;1(1):98. doi:10.1186/s40658-014-0098-4
94. Leube J, Gustafsson J, Lassmann M, Salas-Ramirez M, Tran-Gia J. A Deep-Learning-Based Partial-Volume Correction Method for Quantitative ^{177}Lu SPECT/CT Imaging. J Nucl Med. 2024;65(6):980-987. Published 2024 Jun 3. doi:10.2967/jnumed.123.266889
95. Vicente EM, Lodge MA, Rowe SP, Wahl RL, Frey EC. Simplifying volumes-of-interest (VOIs) definition in quantitative SPECT: Beyond manual definition of 3D whole-organ VOIs. Med Phys. 2017;44(5):1707-1717. doi:10.1002/mp.12164
96. Sandström M, Garske-Román U, Johansson S, Granberg D, Sundin A, Freedman N. Kidney dosimetry during ^{177}Lu-DOTATATE therapy in patients with neuroendocrine tumors: aspects on calculation and tolerance. Acta Oncol. 2018;57(4):516-521. doi:10.1080/0284186X.2017.1378431
97. Hou X, Zhao W, Beauregard JM, Celler A. Personalized kidney dosimetry in ^{177}Lu-octreotate treatment of neuroendocrine tumours: A comparison of kidney dosimetry estimates based on a whole organ and small volume segmentations.

Phys Med Biol. 2019;64(17):175004. Published 2019 Aug 28. doi:10.1088/1361-6560/ab32a1

98. Curkic Kapidzic S, Gustafsson J, Larsson E, Jessen L, Sjögreen Gleisner K. Kidney dosimetry in [^{177}Lu]Lu-DOTA-TATE therapy based on multiple small VOIs. Phys Med. 2024;120:103335. doi:10.1016/j.ejmp.2024.103335
99. Marquis H, Schmidtlein CR, de Nijs R, et al. MIRD Pamphlet No. 32: A MIRD Recovery Coefficient Model for Resolution Characterization and Shape-Specific Partial-Volume Correction. J Nucl Med. 2025;66(3):457-465. Published 2025 Mar 3. doi:10.2967/jnumed.124.268520
100. Mínguez Gabiña P, Monserrat Fuertes T, Jauregui I, Del Amo C, Rodeño Ortiz de Zarate E, Gustafsson J. Activity recovery for differently shaped objects in quantitative SPECT. Phys Med Biol. 2023;68(12):10.1088/1361-6560/acd982. Published 2023 Jun 16. doi:10.1088/1361-6560/acd982
101. Grings A, Jobic C, Kuwert T, Ritt P. The magnitude of the partial volume effect in SPECT imaging of the kidneys: a phantom study. EJNMMI Phys. 2022;9(1):18. Published 2022 Mar 14. doi:10.1186/s40658-022-00446-2
102. Jessen L, Gustafsson J, Ljungberg M, Curkic-Kapidzic S, Imsirovic M, Sjögreen-Gleisner K. 3D printed non-uniform anthropomorphic phantoms for quantitative SPECT. EJNMMI Phys. 2024;11(1):8. Published 2024 Jan 22. doi:10.1186/s40658-024-00613-7
103. Tran-Gia J, Lassmann M. Optimizing Image Quantification for ^{177}Lu SPECT/CT Based on a 3D Printed 2-Compartment Kidney Phantom. J Nucl Med. 2018;59(4):616-624. doi:10.2967/jnumed.117.200170
104. Dewaraja YK, Ljungberg M, Koral KF. Monte Carlo evaluation of object shape effects in iodine-131 SPET tumor activity quantification. Eur J Nucl Med. 2001;28(7):900-906. doi:10.1007/s002590100551
105. Ljungberg M, Strand SE, King M. Monte Carlo Calculation in Nuclear Medicine: Applications in Diagnostic Imaging. IOP Publishing, 1998.
106. Segars WP, Sturgeon G, Mendonca S, Grimes J, Tsui BM. 4D XCAT phantom for multimodality imaging research. Med Phys. 2010;37(9):4902-4915. doi:10.1118/1.3480985
107. Council Directive 2013/59/Euratom of 5 December 2013 laying down basic safety standards for protection against the dangers arising from exposure to ionising radiation. Off J Eur Union. 2014;L13:1-73. Accessed April 20, 2025. https://eur-lex.europa.eu/eli/dir/2013/59/oj
108. Vergnaud L, Dewaraja YK, Giraudet AL, Badel JN, Sarrut D. A review of ^{177}Lu dosimetry workflows: how to reduce the imaging workloads?. EJNMMI Phys. 2024;11(1):65. Published 2024 Jul 18. doi:10.1186/s40658-024-00658-8

109. Uribe C, Peterson A, Van B, et al. An International Study of Factors Affecting Variability of Dosimetry Calculations, Part 1: Design and Early Results of the SNMMI Dosimetry Challenge. J Nucl Med. 2021;62(Suppl 3):36S-47S. doi:10.2967/jnumed.121.262748
110. Brosch-Lenz J, Ke S, Wang H, et al. An International Study of Factors Affecting Variability of Dosimetry Calculations, Part 2: Overall Variabilities in Absorbed Dose. J Nucl Med. 2023;64(7):1109-1116. doi:10.2967/jnumed.122.265094
111. Brosch-Lenz J, Kurkowska S, Frey E, Dewaraja YK, Sunderland J, Uribe C. An International Study of Factors Affecting Variability of Dosimetry Calculations, Part 3: Contribution from Calculating Absorbed Dose from Time-Integrated Activity. J Nucl Med. 2024;65(8):1166-1172. Published 2024 Aug 1. doi:10.2967/jnumed.123.267293
112. Kurkowska S, Brosch-Lenz J, Dewaraja YK, Frey E, Sunderland J, Uribe C. An International Study of Factors Affecting Variability of Dosimetry Calculations, Part 4: Impact of Fitting Functions in Estimated Absorbed Doses. J Nucl Med. 2025;66(3):441-448. Published 2025 Mar 3. doi:10.2967/jnumed.124.268612
113. Fuchs T, Kaiser L, Müller D, Papp L, Fischer R, Tran-Gia J. Enhancing Interoperability and Harmonisation of Nuclear Medicine Image Data and Associated Clinical Data. Verbesserung der Interoperabilität und Harmonisierung von nuklearmedizinischen Bilddaten und zugehörigen klinischen Daten. Nuklearmedizin. 2023;62(6):389-398. doi:10.1055/a-2187-5701
114. Ramonaheng K, van Staden JA, du Raan H. The effect of calibration factors and recovery coefficients on ^{177}Lu SPECT activity quantification accuracy: a Monte Carlo study. EJNMMI Phys. 2021;8(1):27. Published 2021 Mar 18. doi:10.1186/s40658-021-00365-8
115. Zhao W, Esquinas PL, Hou X, et al. Determination of gamma camera calibration factors for quantitation of therapeutic radioisotopes. EJNMMI Phys. 2018;5(1):8. Published 2018 May 2. doi:10.1186/s40658-018-0208-9
116. Juget F, Talip Z, Nedjadi Y, et al. Precise activity measurements of medical radionuclides using an ionization chamber: a case study with Terbium-161. EJNMMI Phys. 2022;9(1):19. Published 2022 Mar 14. doi:10.1186/s40658-022-00448-0
117. Hindorf C, Jessen L, Kapidzic SC, et al. Traceable calibration with ^{177}Lu and comparison of activity meters at hospitals in Norway and Sweden. Phys Med. 2023;116:103170. doi:10.1016/j.ejmp.2023.103170

118. Zanzonico P. The MIRD Schema for Radiopharmaceutical Dosimetry: A Review. J Nucl Med Technol. 2024;52(2):74-85. Published 2024 Jun 5. doi:10.2967/jnmt.123.265668
119. Siebinga H, de Wit-van der Veen BJ, Stokkel MDM, Huitema ADR, Hendrikx JJMA. Current use and future potential of (physiologically based) pharmacokinetic modelling of radiopharmaceuticals: a review. Theranostics. 2022;12(18):7804-7820. Published 2022 Nov 14. doi:10.7150/thno.77279
120. Ivashchenko OV, O'Doherty J, Hardiansyah D, et al. Time-Activity data fitting in molecular Radiotherapy: Methodology and pitfalls. Phys Med. 2024;117:103192. doi:10.1016/j.ejmp.2023.103192
121. Brosch-Lenz J, Delker A, Völter F, et al. Toward Single-Time-Point Image-Based Dosimetry of ^{177}Lu-PSMA-617 Therapy. J Nucl Med. 2023;64(5):767-774. doi:10.2967/jnumed.122.264594
122. Resch S, Ziegler SI, Sheikh G, et al. Impact of the Reference Multiple-Time-Point Dosimetry Protocol on the Validity of Single-Time-Point Dosimetry for [^{177}Lu]Lu-PSMA-I&T Therapy. J Nucl Med. 2024;65(8):1272-1278. Published 2024 Aug 1. doi:10.2967/jnumed.123.266871
123. Hardiansyah D, Yousefzadeh-Nowshahr E, Kind F, et al. Single-Time-Point Renal Dosimetry Using Nonlinear Mixed-Effects Modeling and Population-Based Model Selection in [^{177}Lu]Lu-PSMA-617 Therapy. J Nucl Med. 2024;65(4):566-572. Published 2024 Apr 1. doi:10.2967/jnumed.123.266268
124. Sundlöv A, Gustafsson J, Brolin G, et al. Feasibility of simplifying renal dosimetry in ^{177}Lu peptide receptor radionuclide therapy. EJNMMI Phys. 2018;5(1):12. Published 2018 Jul 5. doi:10.1186/s40658-018-0210-2
125. Gustafsson J, Taprogge J. Theoretical aspects on the use of single-time-point dosimetry for radionuclide therapy. Phys Med Biol. 2022;67(2):10.1088/1361-6560/ac46e0. Published 2022 Jan 19. doi:10.1088/1361-6560/ac46e0
126. Wang C, Peterson AB, Wong KK, Roseland ME, Schipper MJ, Dewaraja YK. Single-Time-Point Imaging for Dosimetry After [^{177}Lu]Lu-DOTATATE: Accuracy of Existing Methods and Novel Data-Driven Models for Reducing Sensitivity to Time-Point Selection. J Nucl Med. 2023;64(9):1463-1470. doi:10.2967/jnumed.122.265338
127. Rinscheid A, Kletting P, Eiber M, Beer AJ, Glatting G. Influence of sampling schedules on [177Lu]Lu-PSMA dosimetry. EJNMMI Phys. 2020;7(1):41. Published 2020 Jun 17. doi:10.1186/s40658-020-00311-0
128. Ginj M, Zhang H, Waser B, et al. Radiolabeled somatostatin receptor antagonists are preferable to agonists for in vivo peptide receptor targeting of

tumors. Proc Natl Acad Sci U S A. 2006;103(44):16436-16441. doi:10.1073/pnas.0607761103

129. Baum RP, Zhang J, Schuchardt C, Müller D, Mäcke H. First-in-Humans Study of the SSTR Antagonist ^{177}Lu-DOTA-LM3 for Peptide Receptor Radionuclide Therapy in Patients with Metastatic Neuroendocrine Neoplasms: Dosimetry, Safety, and Efficacy. J Nucl Med. 2021;62(11):1571-1581. doi:10.2967/jnumed.120.258889
130. Wild D, Grønbæk H, Navalkissoor S, et al. A phase I/II study of the safety and efficacy of [^{177}Lu]Lu-satoreotide tetraxetan in advanced somatostatin receptor-positive neuroendocrine tumours. Eur J Nucl Med Mol Imaging. 2023;51(1):183-195. doi:10.1007/s00259-023-06383-1
131. Reidy-Lagunes D, Pandit-Taskar N, O'Donoghue JA, et al. Phase I Trial of Well-Differentiated Neuroendocrine Tumors (NETs) with Radiolabeled Somatostatin Antagonist ^{177}Lu-Satoreotide Tetraxetan. Clin Cancer Res. 2019;25(23):6939-6947. doi:10.1158/1078-0432.CCR-19-1026
132. Borgna F, Haller S, Rodriguez JMM, et al. Combination of terbium-161 with somatostatin receptor antagonists-a potential paradigm shift for the treatment of neuroendocrine neoplasms. Eur J Nucl Med Mol Imaging. 2022;49(4):1113-1126. doi:10.1007/s00259-021-05564-0
133. Spoormans K, Struelens L, Vermeulen K, De Saint-Hubert M, Koole M, Crabbé M. The Emission of Internal Conversion Electrons Rather Than Auger Electrons Increased the Nucleus-Absorbed Dose for ^{161}Tb Compared with ^{177}Lu with a Higher Dose Response for [^{161}Tb]Tb-DOTA-LM3 Than for [^{161}Tb]Tb-DOTATATE. J Nucl Med. 2024;65(10):1619-1625. Published 2024 Oct 1. doi:10.2967/jnumed.124.267873
134. Cao J, Chen Y, Hu M, Zhang W. ^{177}Lu-PSMA-RLT of metastatic castration-resistant prostate cancer: limitations and improvements. Ann Nucl Med. 2021;35(8):861-870. doi:10.1007/s12149-021-01649-w
135. Kelly JM, Amor-Coarasa A, Ponnala S, et al. Albumin-Binding PSMA Ligands: Implications for Expanding the Therapeutic Window. J Nucl Med. 2019;60(5):656-663. doi:10.2967/jnumed.118.221150
136. Dennis MS, Zhang M, Meng YG, et al. Albumin binding as a general strategy for improving the pharmacokinetics of proteins. J Biol Chem. 2002;277(38):35035-35043. doi:10.1074/jbc.M205854200
137. Kramer V, Fernández R, Lehnert W, et al. Biodistribution and dosimetry of a single dose of albumin-binding ligand [^{177}Lu]Lu-PSMA-ALB-56 in patients with mCRPC. Eur J Nucl Med Mol Imaging. 2021;48(3):893-903. doi:10.1007/s00259-020-05022-3

138. Deberle LM, Benešová M, Umbricht CA, et al. Development of a new class of PSMA radioligands comprising ibuprofen as an albumin-binding entity. Theranostics. 2020;10(4):1678-1693. Published 2020 Jan 1. doi:10.7150/thno.40482
139. Tschan VJ, Borgna F, Busslinger SD, et al. Preclinical investigations using [^{177}Lu]Lu-Ibu-DAB-PSMA toward its clinical translation for radioligand therapy of prostate cancer. Eur J Nucl Med Mol Imaging. 2022;49(11):3639-3650. doi:10.1007/s00259-022-05837-2
140. Borgna F, Deberle LM, Busslinger SD, et al. Preclinical Investigations to Explore the Difference between the Diastereomers [^{177}Lu]Lu-SibuDAB and [^{177}Lu]Lu-RibuDAB toward Prostate Cancer Therapy. Mol Pharm. 2022;19(7):2105-2114. doi:10.1021/acs.molpharmaceut.1c00994
141. Ritt P, Fernández R, Soza-Ried C, et al. Biodistribution and dosimetry of [^{177}Lu]Lu-SibuDAB in patients with metastatic castration-resistant prostate cancer. Eur J Nucl Med Mol Imaging. Published online February 3, 2025. doi:10.1007/s00259-025-07102-8
142. Bernhardt P, Svensson J, Hemmingsson J, et al. Dosimetric Analysis of the Short-Ranged Particle Emitter ^{161}Tb for Radionuclide Therapy of Metastatic Prostate Cancer. Cancers (Basel). 2021;13(9):2011. Published 2021 Apr 22. doi:10.3390/cancers13092011
143. Tschan VJ, Busslinger SD, Bernhardt P, et al. Albumin-Binding and Conventional PSMA Ligands in Combination with ^{161}Tb: Biodistribution, Dosimetry, and Preclinical Therapy. J Nucl Med. 2023;64(10):1625-1631. doi:10.2967/jnumed.123.265524
144. GE Healthcare. Discovery NM/CT 670 Pro: Data Sheet. General Electric Company; 2014. Accessed April 21, 2025. https://www.probomedical.com/wp-content/uploads/2024/09/GE-Discovery-670.pdf
145. Nedjadi Y, Juget F, Desorgher L, et al. Activity standardisation of ^{161}Tb. Appl Radiat Isot. 2020;166:109411. doi:10.1016/j.apradiso.2020.109411
146. National Electrical Manufacturers Association (NEMA). NEMA Standards Publication NU 1-2023: Performance Measurements of Gamma Cameras. Rosslyn, VA: National Electrical Manufacturers Association; 2023.
147. Morphis M, van Staden JA, du Raan H, Ljungberg M. Modelling of energy-dependent spectral resolution for SPECT Monte Carlo simulations using SIMIND. Heliyon. 2021;7(2):e06097. Published 2021 Feb 10. doi:10.1016/j.heliyon.2021.e06097
148. Hemmingsson J, Svensson J, van der Meulen NP, Müller C, Bernhardt P. Active bone marrow S-values for the low-energy electron emitter terbium-161

compared to S-values for lutetium-177 and yttrium-90. EJNMMI Phys. 2022;9(1):65. Published 2022 Sep 24. doi:10.1186/s40658-022-00495-7

149. Hough M, Johnson P, Rajon D, Jokisch D, Lee C, Bolch W. An image-based skeletal dosimetry model for the ICRP reference adult male-internal electron sources. Phys Med Biol. 2011;56(8):2309-2346. doi:10.1088/0031-9155/56/8/001
150. O'Reilly SE, DeWeese LS, Maynard MR, et al. An image-based skeletal dosimetry model for the ICRP reference adult female-internal electron sources. Phys Med Biol. 2016;61(24):8794-8824. doi:10.1088/1361-6560/61/24/8794
151. McIntosh L, Jackson P, Emmerson B, et al. Quantitative calibration of Tb-161 SPECT/CT in view of personalised dosimetry assessment studies. EJNMMI Phys. 2024;11(1):18. Published 2024 Feb 19. doi:10.1186/s40658-024-00611-9
152. Vogel WV, van der Marck SC, Versleijen MWJ. Challenges and future options for the production of lutetium-177. Eur J Nucl Med Mol Imaging. 2021;48(8):2329-2335. doi:10.1007/s00259-021-05392-2
153. U.S. Food and Drug Administration. FDA expands Pluvicto's metastatic castration-resistant prostate cancer indication. Published March 28, 2025. Accessed April 23, 2025. https://www.fda.gov/drugs/resources-information-approved-drugs/fda-expands-pluvictos-metastatic-castration-resistant-prostate-cancer-indication

ACKNOWLEDGEMENTS

First of all, this work would not have been possible without the financial support of the Swedish Cancer Society, the King Gustav V Jubilee Clinic Cancer Foundation, the Swedish Research Council, the Swedish state under the ALF agreement (a collaboration between the Swedish government and the county councils), the Assar Gabrielsson Foundation, the Sahlgrenska University Hospital Fund, and the Royal Society of Arts and Sciences in Gothenburg. I would also like to acknowledge the University of Basel for funding the clinical trials, as well as the Swiss National Science Foundation and Personalized Medicine and Related Technology, whose contributions made the trials possible. Thank you all—your support is invaluable!

Beyond these parties, there are many individuals I would like to thank, without whom this journey would have looked very different. My heartfelt thanks to…

My supervisor, Peter. I am continuously amazed by your ability to think outside the box. If I can emulate even a fraction of your curiosity and creativity, I will be more than content. Above all, I am grateful to have shared this journey with you, and I am happy to call you my friend.

My co-supervisors, Jon and Martijn, for your solid support, and to all the other remarkable researchers I have had the great pleasure of collaborating with—Philipp, Julia, Alin, Lisa, Nick, Christina, and Damian, as well as the kind and hard-working staff at Basel University Hospital and PSI.

My undergraduate teachers at Lund University, for sparking my curiosity in nuclear medicine and for first giving me the tools to navigate this project. A special thanks to my former supervisors—Cecilia, Anna, and Erik. I would not have embarked on this journey had it not been for the confidence you instilled in me during my master's project.

My fellow PhONSA colleagues, past and present: Jens, Emma, Tobias, Linn, Jehangir, Rebecca, Jakob, Johanna S, Johanna D, Albin, and Harald. We've shared some wonderful times, both inside and outside (but mostly outside) of work. I truly could not have asked for a better group. Thanks Alexandra, for taking some of the load off me these last months with the dosimetry—this wouldn't be the thesis it is without you. And Katja… You have meant more to me than I think you realize. Thanks for all the adventures, and for being my honorary office mom on those especially chaotic days.

My colleagues at the department—Magnus, for all our fruitful conversations about undergraduate teaching; Jennie and Mia, for always being there to help with whatever came my way; the PhD student group, for all the fun times (including the very official ones in the basement). And Nishte—thanks for letting me vent and/or crash on your office couch whenever I needed to. In the wise words of some cartoon bear: *You are braver than you believe, stronger than you seem, and smarter than you think.*

Dahls Bageri, for the incredibly generous coffee subscription that came into my life exactly when I needed it. Four large coffees a day for 299 SEK a month?! A bargain!

To my friends, for keeping me at least **reasonably** sane along the way—and especially to the boys in the band, for helping me move apartments just days before handing this in. I feel unbelievably lucky to have you all.

My siblings, Simon and Inez. Although you have little to no idea what I've been up to these past few years (I'll let you debate who knows more…), I think you're proud, and that's all that matters.

Dad. I most definitely inherited my attention to detail and urge to probe from you (and, to be fair, probably Grandpa). Thank you for always encouraging me to seek answers while putting my own happiness first.

Mom, Claes, and the cats. There is no safe space like Villa Sjöblick. And Mamma (or Maria Kraft, rather)—they say we become even more alike as the years go by. I cannot think of a better incentive to grow old.